Surface Acoustic Wave Devices with Non-Contact Interdigital Transducers

Ashish Kumar Namdeo

Surface Acoustic Wave Devices with Non-Contact Interdigital Transducers

A thesis submitted

for the award of the degree of

DOCTOR OF PHILOSOPHY

by

ASHISH KUMAR NAMDEO

DEPARTMENT OF ELECTRONICS AND ELECTRICAL ENGINEERING

INDIAN INSTITUTE OF TECHNOLOGY GUWAHATI

GUWAHATI -781039, ASSAM, INDIA

May 2014

Certificate

This is to certify that the thesis entitled "**Surface Acoustic Wave Devices with Non-Contact Interdigital Transducers**", submitted by me to the Indian Institute of Technology Guwahati for the award of the degree of Doctor of Philosophy, is a bonafide record of research work carried out by me under the supervision of Dr. Harshal B. Nemade. The contents of this thesis, in full or in parts, have not been submitted to any other Institute or University for the award of any degree or diploma.

Dated: Ashish Kumar Namdeo

Guwahati

Certificate

This is to certify that the thesis entitled "**Surface Acoustic Wave Devices with Non-Contact Interdigital Transducers**", submitted by Ashish Kumar Namdeo (08610206), a research scholar in the Department of Electronics and Electrical Engineering, Indian Institute of Technology Guwahati, for the award of the degree of Doctor of Philosophy, is a record of an original research work carried out by him under my supervision and guidance. The thesis has fulfilled all requirements as per the regulations of the institute and in my opinion has reached the standard needed for submission. The results embodied in this thesis have not been submitted to any other University or Institute for the award of any degree or diploma.

Dated:

Guwahati

Dr. Harshal B. Nemade
Professor
Department of Electronics and Electrical Engineering
Indian Institute of Technology Guwahati
Guwahati - 781 039, Assam, India.

"Imagination is more important than knowledge."

- Albert Einstein

To my

Grand Parents, *Ram Deen and Shyam Bai*
Parents, *Rakesh and Ranjana*
Brother, *Aditya*
Sister, *Anupama*

Abstract

Surface acoustic wave (SAW) is a mechanical wave that travels along the surface of an elastic medium. Conventional SAW devices consist of metallic comb-shaped electrodes called interdigital transducer (IDT) patterned over the surface of a piezoelectric substrate. The IDTs convert electrical energy to mechanical energy and vice versa. The IDTs patterned over the piezo-substrate affect the propagation of SAW mainly due to conductivity (electrical load), mass load, dispersion, and other secondary effects. The device characteristics deviate if these effects are not accounted for while designing.

In this thesis, a non-contact arrangement of IDT (NCIDT) is proposed where IDTs are fabricated on a non-piezoelectric holding substrate kept above facing the piezo-substrate with a small air gap, and the electric field between NCIDT and the piezo-substrate is coupled through the air gap. As the piezo-substrate is void of IDTs, the effects mentioned above are either eliminated or greatly reduced. For sensor applications, the proposed configuration provides entire piezo-substrate for sensing, in addition to the convenience of easy cleaning or coating of sensing film due to the absence of bonding wires.

The SAW devices with NCIDTs are simulated by finite element method (FEM) using COMSOL Multiphysics and the most significant result encountered is that the velocity of SAW in the device is appreciably close to the free surface velocity. However, the coupling decreases as the electric field couples through the air gap between the transducer and the piezo-substrate. Thus the proposed technique has applications in the fields of instrumentation, signal processing and communication where frequency accuracy is crucial. The parameters like SAW phase velocity dispersion, reflection coefficient, and electromechanical coupling coefficient as a function of air gap between NCIDT and piezo-substrate are calculated from the simulation results. The comparison of the proposed devices with the conventional SAW devices is presented based on the device parameters, the transduction coefficient, quality factor, SAW phase velocity dispersion, reflection coefficient, and electromechanical coupling coefficient. The thesis includes a thorough analysis of the proposed SAW devices with NCIDT that investigates the effects of the permittivity of the holding substrate, separation between NCIDT and piezo-substrate, thickness of IDT fingers, metallization ratio, and aperture width. Another device configuration to get rid of the bonding wires in SAW devices is proposed in

which the bonding wires in a conventional SAW device are replaced by external metal plates aligned with the existing bond pads in the SAW device and the signal is capacitively coupled between the external plates and the bond pads. Simulations of the proposed device are carried out with finite aperture width and the results are compared with an identical conventional SAW device.

Conventional SAW devices such as SAW delay line and resonator are simulated to verify the mass loading effect of IDT, short circuiting of electric field by IDT, and bulk wave generation. Simulation of SAW sensors based on mass load for NCIDT gives remarkable improvement in sensitivity compared to conventional IDT where the static load of IDT is predominant. Similarly sensors based on conductivity show improved sensitivity in case of NCIDT as the entire piezo-substrate is available for sensing.

Experiments are carried out to verify the device operation, effect of separation between NCIDT and piezo-substrate, tilt of NCIDT, and to check suitability for applications in high sensitivity sensors, and oscillators. The NCIDT for SAW devices are fabricated on silicon substrates and on copper cladded FR4 printed circuit boards. Scattering parameters of the fabricated devices are measured and the results are verified with the simulation results. The experiments are carried out to demonstrate mass loading of liquids for sensing application.

Acknowledgment

I feel it as a great privilege in expressing my deepest and most sincere gratitude to my thesis supervisor Dr. Harshal B. Nemade for his excellent guidance throughout my study. His kindness, dedication, hard work, and attention to detail have been a great inspiration to me. I thank him for the unlimited support, invaluable guidance and infinite patience he has shown to me. He is more than a supervisor for me.

I am thankful to my doctoral committee members Professor R. Bhattacharjee, Professor R. P. Palathinkal and Dr. S. Kanagaraj for sparing their precious time to evaluate the progress of my work. My special thanks to technical staff of EEE Department and centre for Nanotechnology for their support in various task.

I am highly thankful to Indian Nanoelectronics User Program (INUP), and Centre for Excellence in Nanoelectronics (CEN), IISc., Bangalore for providing the fabrication facility to carry out my experimental work. I would like to thank all faculty coordinators of INUP, in particular I would like to thank Dr. Vijay Mishra, INUP coordinator for his tremendous help during my stay at IISc. Bangalore. I would also like to extend my thanks to Ms. Radha Manda and Mr. srinivasa murthy for their encouragement during fabrication and support in carrying out my work in IISc. Bangalore. Most importantly I would like give my gratitude to the INUP staff at CEN, IISc. Bangalore.

Thanks go out to all my friends in Department of EEE- IIT Guwahati, Centre for Nanotechnology - IIT Guwahati, INUP-IISc., Bangalore. They have always been around to provide useful suggestions, companionship and created a peaceful research environment. They all contributed directly or indirectly to this thesis. My special thank to my senior Dr. Ramakrishnan for his help and support always. I would like to thank Priya Madam, Govind, Harish, and Rajib Bhaiya for helping in sorting out some of the experimental data. I would like to thank Amaresh, Shilpa, Amit and Upashi for helping me in sensors experiments.

I am extremely thankful to Mrs. Leena Nemade for her care shown and support given to me during my stay at IIT Guwahati. I would like express my thanks to my friends, Nagesh CH, Kuntal Deka, Rajib Panigrahi, Om Prakash Singh, Sanjoy Mondal, Dr. Krishna, Amit Kumar Dubey, Vishal Deshpande, Mayank Agarwal, and Brijesh. My work in this remote place

definitely would not be possible without their love and care that helped me to enjoy my new life in this IIT Guwahati.

My special thanks to my SAW group member the guys who are always with me, Sai Krishna, Mandar Maitra, Vivek Lukose, Basudeba, Jitendra, Sushanta, and Shyam, for their unconditional care, support, and extreme cooperation during my stay in IIT Guwahati.

During these five years at IIT Guwahati I have had several friends that have helped me in several ways, I would like to say a big thank you to all of them for their friendship and support. I would like to extend thank to all Bachelor of Engineering friends for their continuous encouragement and moral support.

My deepest gratitude goes to my grandparents, parents, brother and sister for their continuous love and support throughout my studies. Especially, I want to thank my mother and father for the opportunities he has given me and his unlimited love and support are the reasons where I am and what I have accomplished so far. I want give my most special thanks for brother for everything.

Finally, I believe this research experience will greatly benefit my career in the future.

Ashish Kumar Namdeo

Contents

List of Figures

List of Tables

List of Acronyms

APM	Acoustic Plate Mode
BAW	Bulk Acoustic Wave
COM	Coupling of Mode
DBAW	Deep Bulk Acoustic Wave
DCE	cis-1,2 Dichloro ethene
DI	De-ionized
DOF	Degrees of Freedom
FEM	Finite Element Method
FPM	Flexural Plate Mode
GUI	Graphical User Interface
IDT	Interdigital Transducer
LPKF	Leiterplatten Kopier Fräsen
LSAW	Leaky Surface Acoustic Wave
MEMS	Microelectromechanical Systems
MR	Metallization Ratio
NCIDT	Non-contact Interdigital Transducer
OHP	Overhead Projector
PCB	Printed Circuit Board
PDE	Partial Differential Equation
PIB	Polyisobutylene
RF	Radio Frequency

RFID	Radio Frequency Identification
SAW	Surface Acoustic Wave
SH	Shear Horizontal
SSBW	Surface Skimming Bulk Wave
TCE	Trichloro ethylene
UV	Ultraviolet

List of Symbols

T	Time period
p	IDT finger pitch
t	Time
v	SAW phase velocity
v_0	Free surface SAW phase velocity in substrate
v_B	BAW velocity
λ	SAW wavelength
f_r	Synchronous or resonance frequency
f_b	3dB bandwidth of SAW device
h_a	Air gap
h_e	Electrode height
k	wave number
N	Number of IDT finger pairs
N_r	Number of reflector strips
r_s	Reflection coefficient of one strip
A_n	Amplitude of impluse
ω	Angular frequency
a_0	Amplitude of step response
K_R	Electromechanical coupling coefficient of Rayleigh wave
C_1	Capacitance per pair of IDT fingers and per unit length
P_R	Mean power density of transported by the wave
$\|U\|$	Amplitude of applied input signal

θ	Periodic section transit angle
R_0	Mechanical impedance
C_s	Electrode capacitance per electrode (static)
j	Imaginary unit
E_n	Electric potential equivalent to F_n (n stands for number of electrodes)
I_n	Equivalent electric current
ϕ	Turns ratio of an acoustic-to-electric circuit transformer
C_T	Total capacitance of IDT
G_a	Radiation conductance
B_a	Susceptance
α	Transduction coefficient
ε	Permittivity
R_f	Thin film resistance in one transduction unit
C_f	Interdigital capacitance in one transduction period
κ	Reflection parameter
F_n	Acoustic terminal force(n stands for number of electrodes)
P_{11} and P_{22}	Reflections coefficients of IDT in P-Matrix
P_{12} and P_{21}	Transmission coefficients of IDT in P-Matrix
P_{13} and P_{23}	Excitation coefficients of IDT in P-Matrix
P_{31} and P_{32}	Current generated by the wave arriving at acoustic ports of IDT
P_{33}	Admittance of IDT in P-matrix
S	Strain

T	Stress
V_{in}	Input electric potential to IDT
V	Scalar electric potential
$\mathbf{u}$	SAW particle displacement
u'_i	Particle velocity of SAW along i direction
$T_{ij(mech)}$	Stress due to mechanical strain
$T_{ij(elec)}$	Stress due to electric field
ε_{ij}	Permittivity tensor of dielectric medium
C^E_{ijkl}	Stiffness tensor for constant electric field
S_{jk}	Strain components
ε^s_{ij}	Permittivity tensor for constant stress
E_j	Electric field vector
ρ	Material density
δ	Edge length
$\mathbf{B}$	Magnetic field
$\mathbf{E}$	Electric field
X, Y, and Z	Crystal lattice direction
k and β	Wave number of the surface wave
U_{left}, *and* V_{left}	Displacements and potentials at left side of boundaries
U_{right} *and* V_{right}	Displacements and potentials at right side of boundaries
f_{sc-}	Lower edge frequency called as resonance frequency
f_{sc+}	Upper edge frequency called as antiresonance frequency
Γ_L	Denotes left side boundary of the SAW resonator geometry

Γ_R	Denotes right side boundary of the SAW resonator geometry
d	IDT electrode width
η	Normalized frequency
f_0	Free surface resonance frequency
Q_r	Quality factor at resonance frequency
Δf	Bandwidth at half of the peak-conductance
γ	Capacitance ratio
f_a	Antiresonance frequency
B_L, B_R and B_B	Critical damping at the edge of the transmitter, receiver, and bottom of the substrate
$\lvert\kappa_p\rvert$	Absolute value of the reflection coefficient per period
K_{eff}^2	Effective electromechanical coupling coefficient
θ_B	BAW propagation angle
λ_B	BAW wavelength
v_{Bmin}	Minimal speed of the BAW
P_B	Total power generated by IDT in the form of bulk wave
s	Slowness of BAW
h_s	Depth of the piezo-substrate
h_h	Thickness of holding substrate
h_a	Air gap between NCIDT and piezo-substrate
α_p	Transaction coefficient per period of fingers
γ_p	Attenuation per period of IDT fingers

G_r Conductance at resonance frequency

v_f Free surface SAW phase velocity of the device

v_m Metallized surface SAW phase velocity of the device

ρ_0 Density of PIB film

h_0 Thickness of PIB film

c_v Concentration of organic vapor in air

k_p Air/sensing film partition coefficient for measurand vapor

ρ_v Vapor density

c Vapor concentration

P Air pressure

R Gas constant

T Air temperature

S_{11} Scattering parameter (return loss)

K^2 Electromechanical coupling coefficient

I Cross-section moment of inertia

i_n Current equivalent to particle velocity for a single pair of electrode of IDT

x_i Co-ordinate axis (i = 1, 2, 3)

ξ Damping ratio

ς Piezoelectric constant used in mason equivalent circuit

Z_o Acoustic impedance

$\mathbf{Z}$ Rayleigh damping matrix

x_i Co-ordinate axis (i = 1, 2, 3)

φ_a	Phase offset of the gratings of IDT
φ_t	Phase offset in the potential
V_{in}	Input voltage to IDT
V_o	Output voltage from IDT
A_{dM}	Mass proportional damping parameter
B_{dk}	Stiffness proportional damping parameter

1

Introduction to Surface Acoustic Wave (SAW) Devices

The surface acoustic wave (SAW) devices have been popular in electronic industries for many years due to their compactness, versatility, efficiency in controlling and processing electrical signals [1]. SAW devices have unique advantages for applications in instrumentation, signal processing and communications that include satellite receivers, remote control units, keyless entry system, radio frequency identification (RFID), television sets, mobile phones, actuators, and sensors [1], [2]. SAW devices such as pulse compression filters, band pass filters, resonators, oscillators, and matched filters are used for spread spectrum communications due to low insertion loss, small size and high operating frequency [3]. Interdigital transducer (IDT) fabricated on a piezo-substrate is used to convert electrical signal into acoustic waves and vice versa [4]. In a SAW device, the most of the acoustic energy is confined to one wavelength depth of the piezoelectric substrate and SAW amplitude decays exponentially with the substrate depth [4]. Since the phase velocity of SAW is about 5 orders lower than the electromagnetic wave, signal processing in acoustic domain is possible in real time in a single compact device [3]. SAW devices are also used as micro actuators such as SAW nano-stepping motors and SAW micropumps [2], [5]. The sensors based on SAW offer high sensitivity for changes in mechanical and electrical properties of the medium usually coated on the surface of the piezo-substrate as a sensing film which is chosen to respond to a specific measurand [6].

Normally piezoelectric substrates made of lithium niobate, lithium tantalate, langasite, and quartz are used to develop SAW devices. Metallic IDT patterned on the piezo-substrate affects the propagation of SAW due to electrical loading, mass loading, dispersion, and other secondary effects [7]–[9], [4]. The characteristics of the fabricated device deviate if these effects are not accounted for while designing.

This thesis mainly focuses on the research work carried out on the analysis of the proposed non-contact arrangement of IDT (NCIDT) where IDTs are fabricated on a non-piezoelectric substrate kept above facing a piezo-substrate with a small air gap, and the electric field between NCIDT and the piezo-substrate is coupled through the air gap. As the piezo-substrate is void of IDTs, the effects mentioned above are either eliminated or greatly reduced. For sensor applications, the proposed configuration provides entire piezo-substrate for sensing, in addition to the convenience of easy cleaning or coating of sensing film due to the absence of bonding wires. The results of simulation and experiments on the proposed devices are presented in this thesis.

1.1 Surface acoustic waves – A brief introduction

The displacement of particles from their equilibrium positions by an external force together with the elastic restoring forces cause the generation of travelling or standing waves in the elastic medium [10]. For a particular particle there are three possible geometries of motion called as polarization such as linear, elliptical, and circular polarization [3], [10]. SAW propagates over the surface of the elastic medium with particles move in elliptical path around their mean position. Two basic patterns of the wave motion occur in elastic medium, namely longitudinal or compressional wave and shear or transverse wave [3]. In longitudinal or compressional waves, the particle displacement is parallel to the direction of wave propagation as shown in figure 1.1 (a). Figure 1.1 (b) shows the shear or transverse wave, where the particle displacement is normal to the direction of wave propagation. The types of

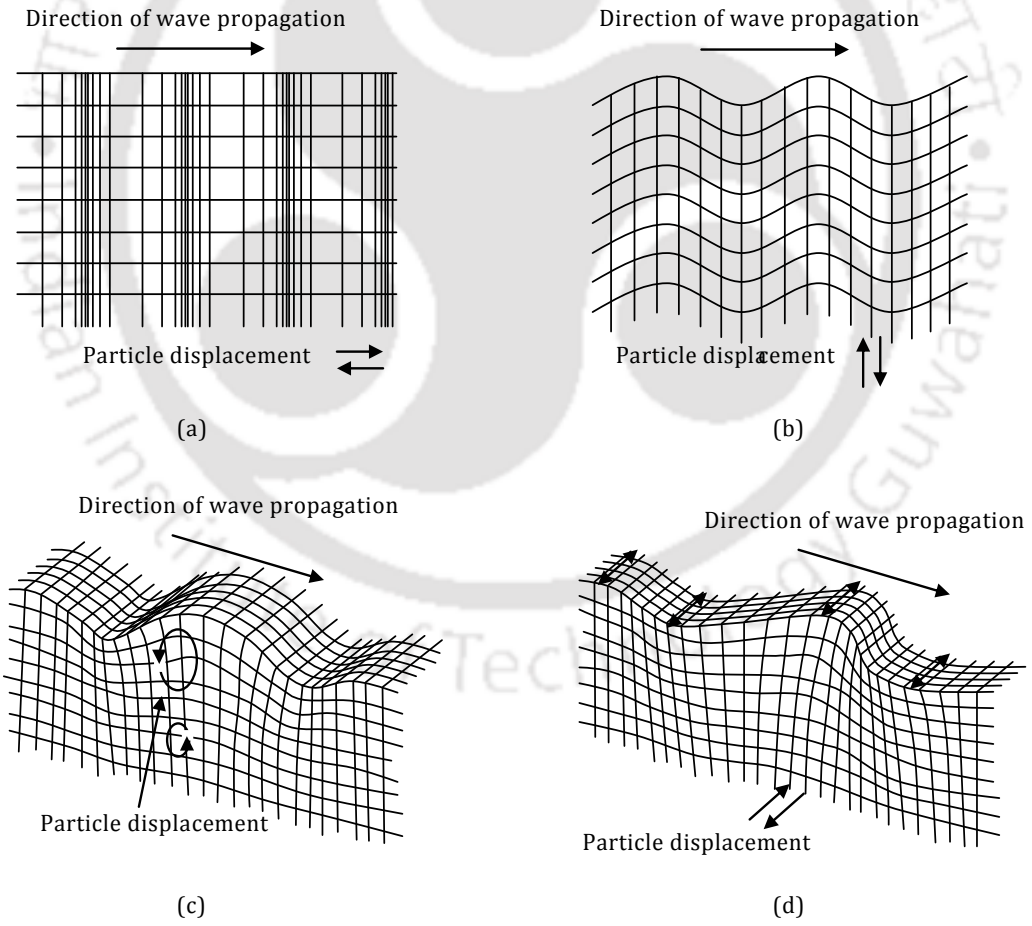

Figure 1.1 Schematic of acoustic wave propagation for (a) longitudinal or compressional wave, (b) shear or transverse wave, (c) Rayleigh wave, and (d) shear horizontal (SH) wave.

acoustic waves generated in a piezoelectric medium are determined by the properties of the piezoelectric material, crystal cut (and therefore orientation), thickness of the medium used, and the configuration of the electrodes used in the transducers [3], [6], [11]. Various possible types of acoustic waves used for SAW devices are Rayleigh wave, shear horizontal (SH) wave, acoustic plate mode (APM) wave, Love wave, and flexural plate mode (FPM) wave [11], [12].

The existence of vibrations in elastic medium was first identified by Lord Rayleigh in year 1885. The particle displacement in elastic Rayleigh wave has both surface normal and surface parallel components with respect to the direction of wave propagation. The particle's movement at the top surface of the elastic medium takes elliptical path in anti-clockwise direction, whereas the particles along the depth of a wavelength of the medium take clockwise direction of motion [1]. A schematic of the Rayleigh wave with particle displacement and propagation is shown in figure 1.1 (c). The electromagnetic field associated with Rayleigh wave travels in the direction of the wave propagation and energy of the wave is confined close to the surface.

With proper selection of the crystal cut of the piezo-substrate SH surface waves can be generated. The particle displacement of this type of wave is predominantly parallel to the plane of the surface and transverse to the direction of wave propagation as shown in figure 1.1 (d). The SH-APM is similar to Rayleigh waves but the substrate thickness is of a few acoustic wavelengths and wave reflects between the surfaces as in plates. The Love waves are SAWs that propagate in a waveguide deposited on a substrate whose thickness is much greater than the waveguide layer [1]. These waves are transverse, bring only shear stresses into action and the amplitude decays exponentially with depth. The energy of Love wave is situated mostly in the waveguide layer and close to the interface. FPM is similar to Rayleigh wave, however the velocity of wave depends on the thickness and material of the plate. The velocity of the wave decreases with reduction in the thickness of the plate.

1.2 Generation of surface acoustic waves - The IDT

A comb-like metallic electrodes patterned over the surface of a piezo-substrate in a SAW device is called as interdigital transducer (IDT) [11]. An IDT is usually made of aluminium (Al) using photolithography [4]. An IDT with bond pads for electrical connection fabricated on a piezo-substrate is shown in figure 1.2 (a). The electrical potential applied to the IDT electrodes produces electric field which generates stresses at the surface of the piezo-substrate. The stress developed due to compression and expansion of the substrate allows the SAW to propagate in both sides of the IDT [4]. When an applied potential is sinusoidal with period T, the vibrations add constructively if the distance between IDT fingers p is equal to the half of the acoustic wavelength for the excitation frequency [4]. Figure 1.2 (b) illustrates the constructive generation of the SAW on a piezo-substrate. The stress wave generated at

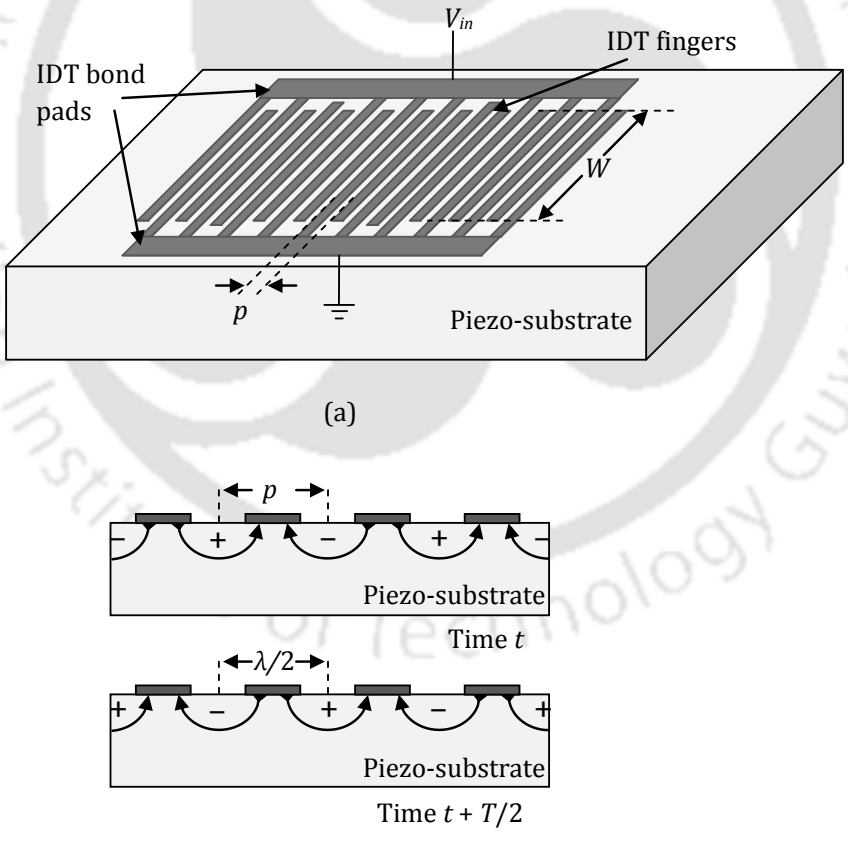

Figure 1.2 (a) Interdigital transducer (IDT) with bond pads on a piezo-substrate. (b) Polarities of applied potentials on IDT fingers at time t and at time $t + T/2$.

time t by a pair of IDT fingers for a given polarity of the applied input potential travels a distance of half acoustic wavelength ($\lambda/2$) in the time interval of half period ($T/2$) with the speed of SAW phase velocity v. As shown in figure 1.2 (b), at time $t + T/2$, the generated stress wave reaches the neighbour IDT finger pair where it adds constructively with the stress wave generated during the next half of the input sinusoid [4].

The stress waves generated by each finger pair add constructively with the stress waves generated by other finger pairs in the subsequent cycles of input excitation resulting in resonance. The resonance frequency or the synchronous frequency f_0 is related to the pitch p of the IDT fingers and SAW phase velocity v as given in equation (1) and equation (2).

$$f_0 = \frac{v}{\lambda} \tag{1}$$

$$\lambda = 2p \tag{2}$$

where, λ is the acoustic wavelength. The bandwidth of the SAW device is determined by the number of finger pairs of the IDT. The 3 dB bandwidth f_b of a SAW device with N number of IDT finger pairs can be estimated [6] as given in equation (3).

$$f_b = \frac{0.88 f_0}{N} \tag{3}$$

The IDTs are fabricated on piezo-substrate using photolithography techniques well established in semiconductor industries [4].

1.3 SAW devices - Basic configurations

The SAW devices are generally operated in two different ways: resonator and delay line [4]. A SAW delay line type device is a two port device, where two IDTs are fabricated at the two ends of the substrate separated by a few wavelengths. One IDT called as a transmitter IDT on electrical excitation generates SAW which propagates towards the other IDT. The IDT at the other end called as a receiver IDT coverts the SAW in electrical output. The pictorial representation of SAW delay line device is shown in figure 1.3 (a).

In SAW resonators, SAW propagates within a resonant cavity such that the wave is reflected back to the generating IDT. The resonator devices are mainly of two types: one port resonator and two port resonator. In one port SAW resonator, a bidirectional IDT is fabricated with a set of reflectors on either side as shown in figure 1.3 (b) [3]. The reflectors could be made of shorted metal strips or grooves. According to the Bragg's frequency, the periodicity of the

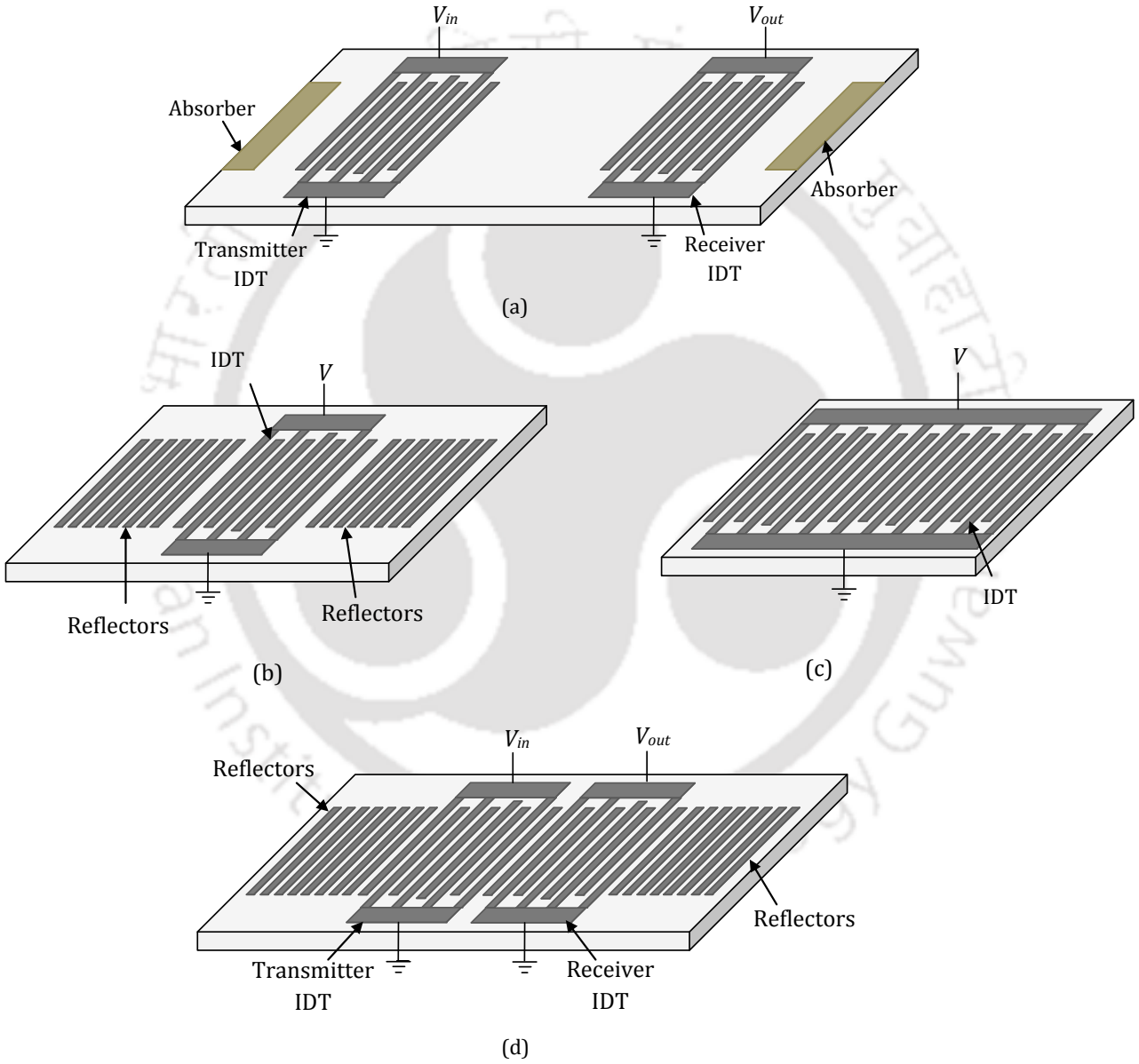

Figure 1.3 Schematic diagrams of SAW devices, (a) SAW delay line device, (b) One-port SAW resonator with reflectors, (c) One-port SAW resonators with long IDT, (d) Two-port SAW resonator with reflectors.

reflector electrodes should be equal to half the wavelength, so that the reflections from individual fingers are in phase and add coherently. Strong reflections are obtained when $N|r_s|>1$, where N is the number of reflector fingers and r_s is the reflection coefficient of a finger. Typically, $|r_s|$ is about 2 % and N is 200 or more [3]. A one port SAW resonator can also be made by using large number of IDT fingers without reflectors as shown in figure 1.3 (c). In this device, multiple reflections within the IDT lead to standing waves and the device resonates at a particular frequency. In case of two port resonator, two sets of reflectors are fabricated on the outer sides of the two bidirectional IDTs as shown in figure 1.3 (d). Two port resonators are used as a controlling element for a high stability oscillator [3].

In conventional SAW devices, the metallic IDTs fabricated on a piezo-substrate cause the secondary effects such as reemission, bulk wave generation, diffraction, phase speed variations, reflections, and electromagnetic coupling [4]. Apart from these effects the IDTs introduce electrical loading, mass loading, resistive loss at high frequency and dispersion of SAWs [7]–[9], [13], [14]. These effects affect the performance of the SAW device. These effects in conventional SAW devices are discussed and verified by simulations based on finite element simulation method (FEM) using COMSOL Multiphysics [14] in chapter 2.

1.4 Problem definition

The main cause of the secondary effects in conventional SAW devices stated in section 1.3 is the presence of metallic IDTs on the piezo-substrate. Effects of mass loading and electrical loading of the IDT electrodes in contact with the substrate are the major reasons for the most of the secondary effects [7]. Therefore, we thought of removing IDTs from the device substrate and coupling electric field through an air gap to eliminate the secondary effects. Apart from elimination of secondary effects we realized the following additional advantages of the proposed non-contact IDT (NCIDT) configuration. As the secondary effects vanish, the accuracy of the designed parameters improves. NCIDT provides entire clean surface of piezo-substrate for sensing applications giving significant increase in sensitivity especially for sensors based on mass load and conductivity. In addition, we would get rid of bonding wires that interfere with the coating process of sensing films [16].

1.5 Literature reports – Electric field coupled SAW devices

Not much published literature is found related to the proposed SAW device configurations. However the electric field coupling between a piezoelectric half-space and a plane at a height is reported by the following authors. Morgan [3] discussed the application of effective permittivity and the coupling between a piezoelectric half-space and a plane at a height. Coupling decreases exponentially with increase the height of air gap, thus the gap has to be a small fraction of wavelength for the concept to be practically effective. Kino [17] presented types of acoustoelectric amplifier and convolver using coupling of field through air gap. The coupling of electric field to piezoelectric substrate using normal mode theory and perturbation theory is well explained in [18], [19]. Ingebrigtsen [20] reported that in order to transmit mechanical force to the piezo-substrate, a direct contact in necessary while electrical forces can be transmitted to the substrate from outside the surface of the substrate in the range of wavelength. The suggestion that the IDTs can be made on a separate substrate permanently bonded with the piezoelectric substrate was given several years ago in a patent by Eda *et al*. [21]. We have analyzed and carried out various observations by simulations and experiments of NCIDT SAW devices and concluded that the proposed configuration has potential applications in the field of signal processing and communication where frequency accuracy is crucial. Other applications include high sensitivity SAW sensors as the entire piezo-substrate is available for sensing and convenient operation as bonding wires are eliminated.

1.6 Scope of the thesis

In this thesis, we present two types of electric field coupled SAW device configurations: 1. SAW device with NCIDT, 2. SAW device with electric field coupled bond pads. The first SAW device comprises of piezoelectric substrate and NCIDT fabricated on non-piezoelectric substrate kept above facing to the piezo-substrate with a small air gap. The second SAW device comprises of piezoelectric substrate, IDT fabricated over the piezo-substrate, and external electrodes with metal plates aligned over the bond pads with or without air gap. The thesis aims in studying the SAW devices with NCIDT and SAW devices with electric field coupled bond pads and their advantages over the conventional SAW devices. The scope of the thesis includes the following.

- Study and simulation of conventional SAW devices such as one port SAW resonator with infinite number of IDT fingers and SAW delay line device, to verify the secondary effects using COMSOL Multiphysics based on FEM.

- Simulation of the proposed SAW devices with NCIDT such as one port SAW resonator with infinite number of IDT fingers and SAW delay line device, and their comparison with the conventional SAW devices; study of various aspects pertinent to the proposed SAW devices that includes effects of permittivity of the holding substrate, thickness of holding substrate, separation between NCIDT and piezo-substrate, thickness of IDT fingers, metallization ratio, and secondary effects in the proposed SAW device with NCIDT.

- Study and simulation of proposed SAW devices with electric field coupled bond pads and comparison with conventional SAW devices.

- Methodology to fabricate the proposed electric field coupled SAW devices and measurements of fabricated SAW devices using network analyzer.

- Experimental validation of the proposed SAW devices with NCIDT and experiment to study the non-ideal conditions such as effects of separation, effects of tilt and effects of orientation.

- Experiments of proposed SAW delay line device with NCIDT and demonstration of a sensor based on mass loading effect.

1.7 Thesis organization

The thesis works have been organized into 7 chapters and the contents are briefly outlined as follows.

In chapter 1, we give brief introduction of SAW, generation of SAW by an IDT, basic configuration of SAW devices, problem definition, and literature reports of electric field coupled SAW devices.

In chapter 2, we introduce various modeling and simulation techniques for SAW devices such as discrete source or delta function method, impulse response method, piezoelectric permittivity method, equivalent circuit model, coupling of modes (COM) model, and finite element simulation of SAW devices using COMSOL Multiphysics (commercial FEM based software). We perform the optimization of mesh density and calculation of free surface velocity. In later part of the chapter presents simulations of conventional SAW devices like a one port SAW resonator in 2 dimension (2D) and in 3D, SAW delay line device, and verification of secondary effects such as mass loading, electrical loading, and bulk acoustic wave (BAW) generation in SAW resonator and SAW delay line, using COMSOL Multiphysics.

Chapter 3 is devoted to the proposed SAW devices with NCIDT. Simulations of a one port SAW resonator with NCIDT in 2D and in 3D, simulation of SAW delay line device are performed. The simulation results are compared with identical conventional SAW device as simulated in chapter 2. Various aspects such as effects of permittivity of the holding substrate, thickness of holding substrate, separation between NCIDT and piezo-substrate, effects of air gap on various device parameters, thickness of IDT fingers are presented and studied by simulation. The secondary effects such as mass loading, electrical loading, and bulk acoustic wave (BAW) generation in proposed SAW devices, resonator and delay line types, with NCIDT are analyzed and the results are compared with the simulation results for conventional SAW devices. Two types of sensors as direct mass load and with sensing film are also simulated for proposed device configuration and the sensitivity is compared with the sensitivity of conventional SAW sensors.

In chapter 4, another SAW device proposed with electric field coupled bond pads is discussed. Simulation of a one port SAW resonator with proposed configuration in 3D is discussed and the simulation results are compared with identical conventional SAW device.

In chapter 5, fabrication of SAW device with NCIDT using UV photolithography and using LPKF PCB prototyping machine is presented.

In chapter 6, we present details of fabrications of the proposed NCIDT SAW devices on Si substrate and on copper clad FR4 printed circuit boards. The testing of the fabricated devices carried out using network analyzer by measurement of scattering parameters. Non-ideal situations in the proposed SAW device such as effects of change in separation, effects of tilt between NCIDT and piezo-substrate are studied experimentally. Measurements on SAW delay

line and sensor based on direct mass loading effect are carried out. The results are compared with the simulation results on the proposed SAW devices under ideal conditions.

Chapter 7 lists the conclusion of the research work and recommendation for future work.

2

Modeling and Simulation of Conventional SAW Devices

In order to describe the function of IDT fabricated on the piezo-substrate in a SAW device several methods of modeling are available such as discrete source or delta function method, impulse response method, piezoelectric permittivity method, matrix representation, coupling of mode (COM) method, numerical techniques using equations, and equivalent circuit method [4], [22]. The finite element method (FEM) is a numerical technique that allows simulating the devices with any number of IDT fingers and easy visualization of the device response for the applied boundary conditions [22], [23]. This chapter mainly describes the simulations of conventional SAW devices such as one port SAW resonators, SAW delay line devices, and the secondary effects of the IDTs on the device response by FEM using COMSOL Multiphysics. Brief descriptions of the modeling techniques used for SAW devices are given in the following sections.

2.1 Discrete source or delta function method

The discrete source method or delta function method is one of the earliest and simplest methods which explain the shape of the IDT frequency response [4]. It does not consider energy, capacitance, and electromechanical coupling coefficient of the material used in the device. The discrete source model is derived from the examination of spatial distribution of charge density or electric field at the surface of piezoelectric substrate. This method associates either two charge spikes of the same sign to each IDT finger or two electric field spikes of the same sign to each interval between adjacent IDT fingers [4]. The spatial distributions of charge density and electric field of two pairs of IDT fingers and infinite pairs of IDT fingers are shown in Figures 2.1 (b) and (c), respectively. The broken line shows the deviation in the spatial distributions of charge density and electric field for two pairs of IDT fingers. The end effects of IDTs in large number of IDT pairs can be neglected. Thus the electrical quantities are assumed periodic in Figures 2.1 (b) and (c). As per the discrete source method, the charge density or electric field spikes normal to the piezo-substrate from IDT fingers are assumed as two delta function sources or can be simplified to one delta function source [4]. The amplitude of each delta function is proportional to the corresponding aperture W of the IDT and sign depends on the polarity of the charge density or electric field. Figure 2.1(d) shows an array of discrete sources at the center of the IDT finger intervals. The frequency response of IDT with discrete source method can now be expressed as

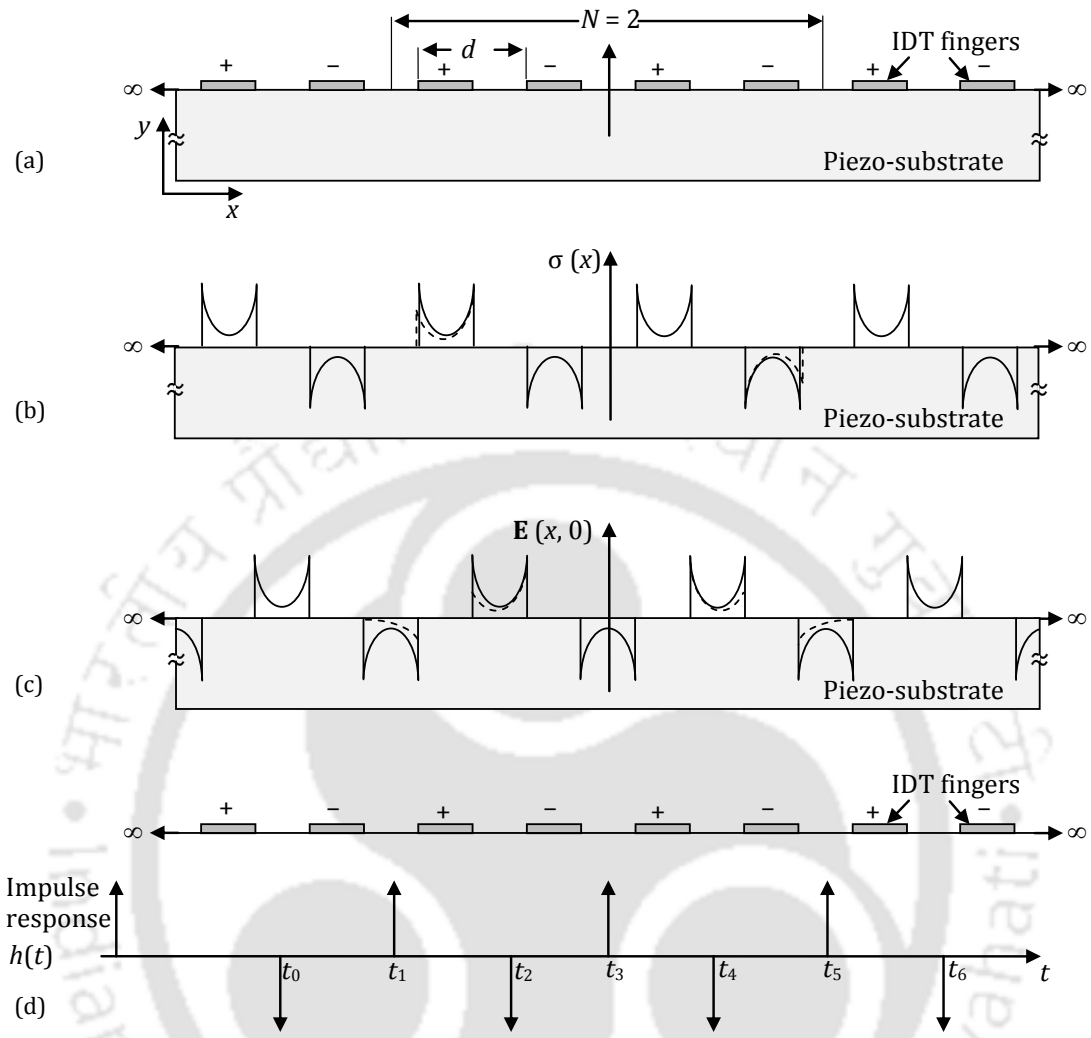

Figure 2.1 (a) Schematic of IDT fabricated on piezo-substrate. (b) Spatial distribution of charge density at the surface of piezo-substrate. (c) Spatial distribution of electric field at the surface of piezo-substrate. (d) Array of discrete sources at the centers of the interval between IDT fingers.

Note: Solid line shows spatial distribution with $N = \infty$, and broken line shows deviation in the spatial distribution for $N = 2$.

$$H(\omega) = \sum_{n=0}^{N-1} (-1)^n A_n e^{-i\omega t_n} \tag{4}$$

where, A_n is the amplitude of impulse, ω is the angular frequency and N is the number of finger pairs in IDT. The expression given in the equation (4) can be approximated as a sinc function. The detailed description of this method is given in [4].

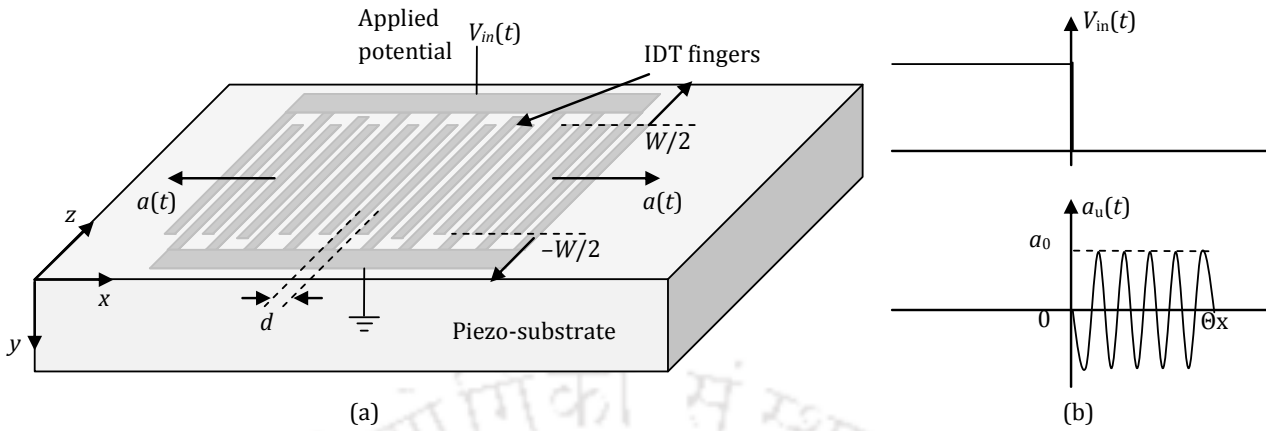

Figure 2.2 (a) Schematic of IDT fabricated on piezo-substrate. (b) Response to unit step voltage input.

2.2 Impulse response method

The impulse response method predicts the absolute amplitude, hence the power of SAW by considering the energy of the wave [4]. A unit step signal is applied to the IDT fabricated on the piezo-substrate and the output response is shown in Figure 2.2(b). If the IDT electrodes are short circuited at t = 0 the response of the device with unit step signal for duration of N/f_0 can be expressed as

$$a_u(t) = \begin{cases} -a_0 \sin(2\pi f_0 t) & \text{for } 0 < t < N/f_0 \\ 0 & \text{for } t > N/f_0 \end{cases} \tag{5}$$

$$a_0 = K_R \sqrt{f_0 C_1/2} \tag{6}$$

where, $C_1 = \varepsilon_P + \varepsilon_0$ is the capacitance per pair per unit length of IDT fingers. Thus the impulse response from (5) and (6) can be expressed as

$$h(t) = \pi\sqrt{2} K_R C_1^{1/2} f_0^{3/2} \cos(2\pi f_0 t), \qquad \text{for } 0 < t < N/f_0 \tag{7}$$

If a sinusoidal signal with unit amplitude is applied to the input, the mean power density transported by the wave can be expressed as

$$P_R = \frac{\pi^2 N^2 a_0^2}{2}|U|^2 = \frac{\pi^2}{4} N^2 K_R f_0 C_1 |U|^2 \quad (8)$$

where, $|U|$ is the amplitude of applied input signal. The detailed description about impulse response method is given in [4].

2.3 Piezoelectric permittivity method

This method of modeling describes the electric potential associated with SAW in terms of actual charge density by considering the surface piezoelectric permittivity and quasi-static approximation. It analyzes the reemission by the IDT fingers but not the reflections from each other. The piezoelectric permittivity method is well described in [4].

2.4 Equivalent circuit model

The Mason equivalent circuit for surface wave transducers is well explained by smith *et al*. [24]. A periodic section of IDT can be represented by an equivalent electromechanical circuit. Two field models described in this method are shown in Figures 2.3 (b) and (c). The cross-

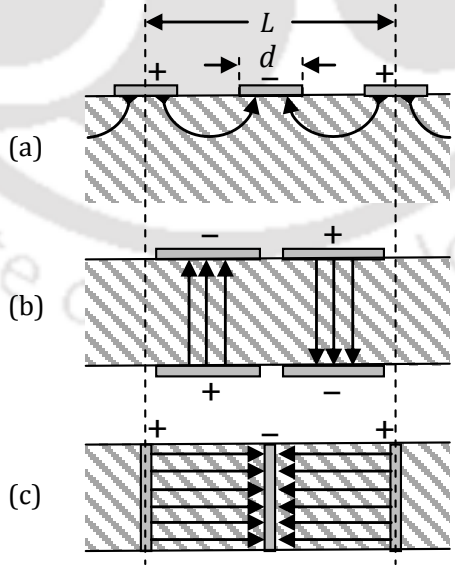

Figure 2.3 (a) Electric field lines in a conventional SAW device. (b) Cross-field approximation. (c) In-line-field approximation.

field model is constituted when SAW propagates in the direction normal to the excitation field. In the in-line-field model, the wave is generated in the direction parallel to the excitation field [4], [22]. Figure 2.3(a) shows electric field lines in a conventional SAW device. The equivalent circuit model method of representation is based on the assumption that one of the two electric fields associated with the SAW device plays dominant role.

The equivalent circuit model of one period of IDT is shown in Figure 2.4. It consists of three ports, viz. two acoustic ports and one electric port. The electrical equivalent of the two acoustic ports is represented as SAW transmission line and third port is represented as electric port where the electric potential is applied and sensed. In this model, θ is expressed as $2\pi f/f_0$, where f is the frequency of the applied input potential and f_0 is the resonance frequency and is the periodic section transit angle. R_0 is the electrical equivalent to Z_0 or mechanical impedance given by

$$R_0 = \frac{Z_0}{\phi^2} \tag{9}$$

where, $\phi = \varsigma C_s/2$ is the turns ratio of an acoustic-to-electric circuit transformer, C_s is the static electrode capacitance of one periodic section, and ς is a piezoelectric constant. In this model, the acoustic forces are converted into electric potentials as $E_n = F_n/\theta$ and SAW velocities are converted into equivalent electric currents $I_n = v_n' \theta$. These transformations allow the mechanical characteristic admittance (similar to the transmission line characteristic impedance expressed in ohms) to be expressed as an equivalent transmission line characteristic admittance as,

$$G_0 = \frac{1}{R_0} = \frac{\omega C_s K^2}{2\pi} \tag{10}$$

where, K^2 represents electromechanical coupling coefficient and its values can be approximated by $-2\Delta v/v$, where, Δv is the change in SAW velocity when the piezoelectric surface is electrically shorted by a thin metal film. The values of K^2 for typical substrates are given in Appendix A. The entire IDT can be realized by connecting acoustic ports in cascade and electrical ports in parallel as shown in Figure 2.5.

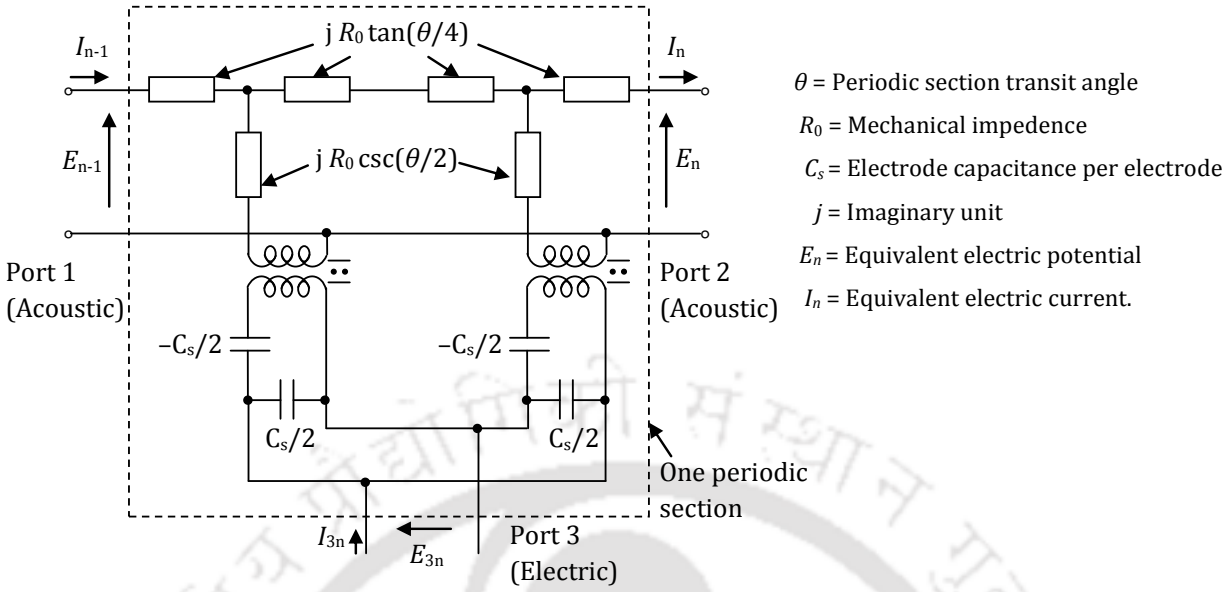

Figure 2.4 Mason equivalent circuit of one period of IDT analyzed by Smith *et al.* [24]

If the generator IDT and receiver IDT of the SAW device are completely matched, the Y parameters of the 3-port network using the equivalent circuit of a period of an IDT can be expressed as

$$\begin{bmatrix} I_1 \\ I_2 \\ I_3 \end{bmatrix} = \begin{bmatrix} -jG_0 \cot N\theta & jG_0 \csc N\theta & -jG_0 \tan(\theta/4) \\ jG_0 \csc N\theta & -jG_0 \cot N\theta & jG_0 \tan(\theta/4) \\ -jG_0 \tan(\theta/4) & jG_0 \tan(\theta/4) & j\omega C_T + 4jNG_0 \tan(\theta/4) \end{bmatrix} \begin{bmatrix} E_1 \\ E_2 \\ E_3 \end{bmatrix} \quad (11)$$

where, $C_T = NC_s$ (total capacitance of IDT) [24]. The overall equivalent circuit of an IDT is shown in Figure 2.6 [4], [25]. The input admittance can be expressed as

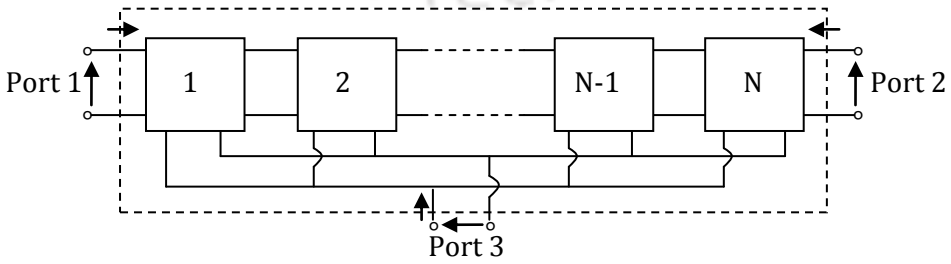

Figure 2.5 Equivalent circuit for entire IDT, made up with N pairs of IDT finger with acoustic ports in cascade and electrical ports in parallel.

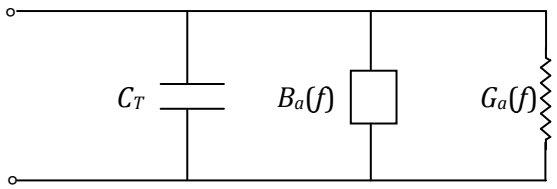

Figure 2.6 Overall equivalent circuit of an IDT.

$$Y(f)=G_a(f)+B_a(f)+j\omega C_T \tag{12}$$

where, $G_a(f)$ is the radiation conductance and $B_a(f)$ is the susceptance given as

$$G_a(f)\approx 8N^2G_0\left|\frac{\sin X}{X}\right|^2 \tag{13}$$

$$B_a(f)=8N^2G_0\left|\frac{\sin(2X)-2X}{2X^2}\right|^2 \tag{14}$$

where, $X = N\pi(f-f_0)/f_0$. The radiation susceptance is a reactive parameter that goes to zero at the resonance frequency. This term is often omitted in calculations near the resonance frequency because it is negligible compared to the total IDT capacitance term.

2.5 Coupling of mode (COM) model

COM model is widely used in designing of SAW devices [4], [23], [26]. This method is based on local analysis of way of two coupled waves evolve when propagating in both directions opposite to each other. This section gives brief description about COM model. The COM model is discussed well by [23] and [27]. The COM model comprises of differential equations governing SAW mode amplitudes $R(x, \omega)$, $S(x, \omega)$ in either side of IDT and the current due to the flow of charges $I(x, \omega)$(see Figure 2.7).

$$\begin{aligned}
\frac{dR(x)}{dx} &= -jk_E R(x)+j\kappa_R e^{-j2k_0x}S(x)+j\alpha_R V e^{-jk_0x}\\
\frac{dS(x)}{dx} &= -jk_E S(x)+j\kappa_s e^{+j2k_0x}R(x)-j\alpha_S V e^{+jk_0x}\\
\frac{dI(x)}{dx} &= +j2\alpha_S R(x)e^{+j2k_0x}+j2\alpha_R S(x)e^{-jk_0x}-j\left(\frac{3\omega C_F/\lambda}{3+j\omega R_F C_F}\right)_S V
\end{aligned} \tag{15}$$

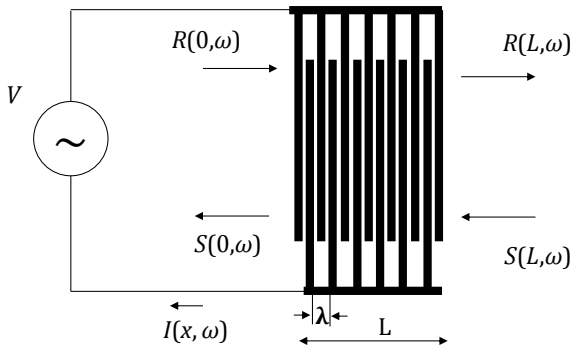

Figure 2.7 Coordinates of an IDT [27].

where, V is the voltage across the IDT electrodes, $k_0=2\pi/\lambda$ is transducer synchronous wave number, and

$$\kappa_E = +\frac{\omega}{v} - \left(\frac{2\alpha_R^2 \omega R_f^2 C_f^{\,2} \lambda}{9+(\omega R_f C_f)^2}\right) - j\left[\gamma + \left(\frac{6\alpha^2 R_f \lambda}{9+(\omega R_f C_f)^2}\right)\right]$$

$$\alpha_R = \frac{3\alpha e^{+j\phi_T}}{3+j\omega C_f R_f}$$

$$\alpha_S = \frac{3\alpha e^{-j\phi_T}}{3+j\omega C_f R_f} \qquad (16)$$

$$\kappa_R = +\kappa_i e^{+j\phi_B} + \frac{2j\alpha^2 R_f \lambda e^{-2j\phi_T}}{3+j\omega C_f R_f}$$

$$\kappa_S = +\kappa_i e^{-j\phi_B} + \frac{2j\alpha^2 R_f \lambda e^{+2j\phi_T}}{3+j\omega C_f R_f}$$

In the above equations $\phi_T = \pi$ and $\phi_B = \pi/2$ are phase offsets of the grating and the potential respectively, and $\omega = 2\pi f$ is the angular frequency. The COM parameters are as follows. v phase velocity of SAW, α transduction coefficient, R_f thin film resistance in one transduction unit, C_f interdigital capacitance in one transduction period, κ the reflection parameter, γ propagation loss per unit length. The suffix R and S represent the values for the corresponding direction of wave propagation shown in Figure 2.7. These parameters can be computed through computer simulation such as FEM or using experimental analysis of a test structure. The COM equations can be represented in P matrix form. The acoustic ports are treated as scattering port and electric port as admittance port and

$$\begin{bmatrix} S(0) \\ R(L) \\ I \end{bmatrix} = \begin{bmatrix} P_{11} & P_{12} & P_{13} \\ P_{21} & P_{22} & P_{23} \\ P_{31} & P_{32} & P_{33} \end{bmatrix} \begin{bmatrix} R(0) \\ S(L) \\ V \end{bmatrix} \tag{12}$$

where,

$$P_{11} = \frac{+jK_S \sin(DL)}{D\cos(DL) + j\Delta\sin(DL)}$$

$$P_{12} = \frac{D}{D\cos(DL) + j\Delta\sin(DL)} e^{-jK_0 L}$$

$$P_{13} = P_{31} + jL\frac{\sin(DL/2)}{DL/2} \times \frac{\alpha_S D\cos(DL/2) + j(K_S\alpha_R + \Delta\alpha_S)\sin(DL/2)}{D\cos(DL) + j\Delta\sin(DL)}$$

$$P_{22} = \frac{+jK_R \sin(DL)}{D\cos(DL) + j\Delta\sin(DL)} e^{-j2K_0 L}$$

$$P_{23} = P_{32} + jL\frac{\sin(DL/2)}{DL/2} \times \frac{\alpha_R D\cos(DL/2) + j(K_R\alpha_S + \Delta\alpha_R)\sin(DL/2)}{D\cos(DL) + j\Delta\sin(DL)}$$

$$P_{33} = +j2\left(\frac{K_S\alpha_R^2 + K_R\alpha_S^2 + 2\Delta\alpha_R\alpha_S}{D^3}\right) \times DL - \frac{D\sin(DL) + j\Delta(1-\cos(DL))}{D\cos(DL) + j\Delta\sin(DL)}$$

$$-2\left(\frac{K_S\alpha_R^2 + K_R\alpha_S^2 + 2\Delta\alpha_R\alpha_S}{D^3}\right) \times \left(\frac{1-\cos(DL)}{D\cos(DL) + j\Delta\sin(DL)}\right) \times j\left(\frac{3\omega C_f L/\lambda}{3 + j\omega R_f C_f}\right)$$

$$\Delta = K_E - K_0$$

$$D = \sqrt{\Delta^2 - K_R K_S}$$

P_{11} and P_{22} are the reflection coefficients, and P_{12} and P_{21} are the transmission coefficients. The remaining terms P_{13} and P_{23} correspond to the excitation coefficients of the IDT and the term P_{33} clearly represents the admittance of the structure relating the current flowing in the electrode (i) and the drive voltage (V). P_{31} and P_{32} terms represent the current generated by the waves arriving at the acoustic ports. Admittance or P_{33} can be calculated from simulations and it is the most useful parameter in the device design.

2.6 Solution of SAW

This section discusses the basics of piezoelectricity, governing equations for SAW propagation, boundary conditions and solutions to the differential equations. Various types of acoustic waves propagate in an elastic medium as described in section 1.1 of chapter 1. The work in this thesis is mainly focused on Rayleigh waves. It is important to study the nature of

the acoustic waves and piezoelectric theory to understand the SAW devices. In this thesis, the term 'SAW' without further qualification is taken to mean Rayleigh waves.

2.6.1 Elasticity in piezoelectric materials

Elasticity in a solid is concerned with the internal forces within it and displacement of solid from its equilibrium position [3]. The forces are expressed by stress T, while the displacements are expressed by strain S. The particle is an elementary region of a material much larger than the inter-atomic distance and much smaller than any characteristic elastic dimensions such as wavelength. Let us assume that in equilibrium state of solid, a particle is located at point $\mathbf{x} = (x_1, x_2, x_3)$ and displaced by an amount $\mathbf{u} = (u_1, u_2, u_3)$, where, the components u_1, u_2 and u_3 are the general components of coordinates x_1, x_2 and x_3, respectively. Thus the particle has been displaced to a new position $\mathbf{x} + \mathbf{u}$ as shown in Figure 2.8. If $\mathbf{u}$ is independent of $\mathbf{x}$ there will be no internal force, since this simply shows a displacement of a material as a whole, and also there will be no force if the material is rotated. The strain at each point can thus be defined as

$$S_{ij}(x_1, x_2, x_3) = \frac{1}{2}\left(\frac{\partial u_i}{\partial x_j} + \frac{\partial u_j}{\partial x_i}\right), \quad i, j = 1,2,3. \tag{13}$$

Thus the strain is related to the internal forces. The strain is a second rank tensor and

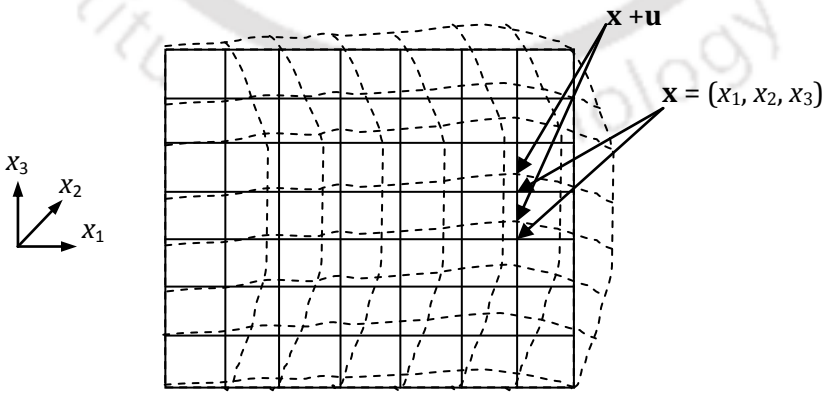

Figure 2.8 Particles position in equilibrium and deformed states of solid body. Note: The deformation of the solid is shown in broken lines [10].

symmetrical as $S_{ij} = S_{ji}$.

The stress T is defined as internal stress in the material *i.e.* force per unit area. The second-rank stress tensor is defined as $T_{ij}(x_1, x_2, x_3)$ and it is symmetric, $T_{ij} = T_{ji}$. According to Hooke's law, each components of stress is given by the linear combination of the strain components and it is expressed as

$$T_{ij(mech)} = \sum_k \sum_l c_{ijkl} S_{kl}, \qquad i, j, k, l = 1, 2, 3. \tag{14}$$

where, c_{ijkl} is the fourth-rank stiffness tensor. These elements are the physical properties of the materials under consideration [3].

2.6.2 Piezoelectricity and constitutive equations

Piezoelectricity phenomenon was discovered by Pierre & Jacques Curie and it was named by Hankel in 1981 [28]. The piezoelectricity is a Greek word which means 'electricity by pressure.' The external force exerted on piezoelectric material results in the generation of electric field at the surface of the material. A simple molecular model of piezoelectric material is given in Figures 2.9 (a) and (b) [28]. Before an external force to the piezoelectric material, the gravity centers of positive and negative charges of each molecules of the piezoelectric material coincide. Thus the external effects of charges reciprocally cancel and electrically neutral molecules appear. By applying an external force to the material, the internal reticular structures of the molecules deform that results in the separation of gravity centers of positive and negative charges of the molecules and generates the electric dipoles. The facing dipoles are mutually cancelled and a distribution of linked charges appears at the surface of the piezoelectric materials. Figure 2.9 (c) shows the linked charges inside the piezoelectric materials after subjecting an external force *F*. The polarization generates an electric field which causes the flow of the free charges existing in the conductor in contact. The free charges will move towards the end where the polarization is of opposite sign and will remain until the free charges neutralize the polarization effects. When an external force is removed the polarization will disappear and material gets equilibrium position. This process can be demonstrated using galvanometer. The demonstration consisting of piezoelectric material with metal plate deposited at both ends and connected to the galvanometer as shown in Figures 2.9 (d) and (e) [28].

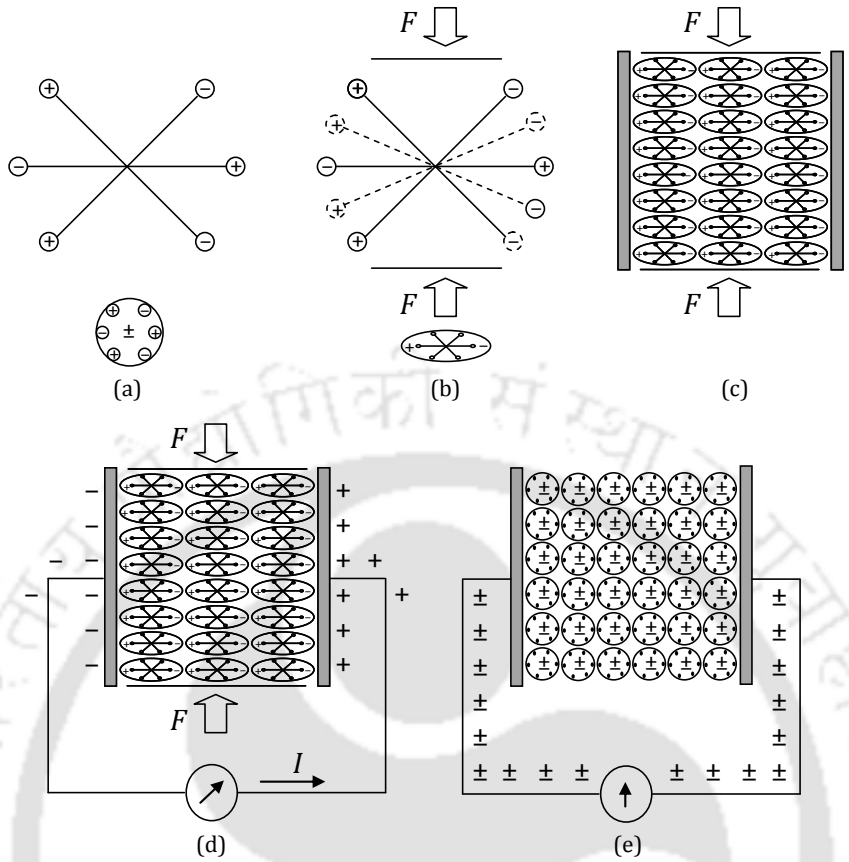

Figure 2.9 Piezoelectricity in piezoelectric materials, (a) An unperturbed single molecule, (b) Molecule subjected to an external force *F*, (c) Polarization effects in the piezoelectric material. (d) Neutralizing current flowing through the external conductor after application of external force *F*. (e) Absence of current in unperturbed material.

Consequently, piezoelectricity can be defined as a phenomenon which couples the elastic stresses and strains to the electric fields and displacements and occurs only in anisotropic materials, whose internal structure lacks a center of symmetry [3]. The stress, $T_{ij(elec)}$ produced by the piezoelectric effect is given by

$$T_{ij(elec)} = \sum_k e_{kij} E_k, \qquad i, j, k, l = 1, 2, 3. \tag{14}$$

where, electric field $E_k = -\frac{\partial V}{\partial x_k}$. Total stress T_{ij} is the sum of stresses due to the electric field E_k and mechanical strain and can be expressed as [3], [12]

$$T_{ij} = \sum_k \sum_l c_{ijkl}^E S_{kl} - \sum_k e_{kij} E_k$$
$$= \sum_k \sum_l c_{ijkl}^E S_{kl} + \sum_k e_{kij} \frac{\partial V}{\partial x_k} \quad (15)$$

From (13) and (15)

$$T_{ij} = \sum_k \sum_l c_{ijkl}^E \frac{\partial^2 u_k}{\partial x_k} + \sum_k e_{kij} \frac{\partial V}{\partial x_k} \quad (16)$$

When an electric field is applied to the dielectric medium, the electric displacement can be expressed by electric field and permittivity tensor ε_{ij} of the dielectric medium. In case of piezoelectric material, the additional electric field displacement caused by the strain is developed due to piezoelectric effect. The total electric displacement D_i can then be given as

$$D_i = \sum_j \varepsilon_{ij}^s E_j + \sum_j \sum_k e_{ijk} S_{jk} \quad (17)$$

where, c_{ijkl}^E is the stiffness tensor for constant electric field (N/m^2), S_{jk} is the strain components, e_{ijk} is the piezoelectric tensor relating elastic to electric fields (C/m^2), ε_{ij}^s is the permittivity tensor for constant stress (F/m), and E_j is the electric field vector (V/m) [3].

2.6.3 Equation of motion

If the stress and strain are functions of time and position then the above equations can be expressed in the terms of equation of motion using Newton's laws [3]. Theoretically, the electric field distribution can be found by solving the equations of Newton and Maxwell simultaneously. For an elementary cube centered at $x' = (x_1', x_2', x_3')$ with edge length of δ, density ρ, and the mass $\rho\delta^3$, the total force in terms of stress along x_i direction is given by

$$\delta^3 \left[\sum_j \frac{\partial T_{ij}}{\partial x_j} \right]_{x'} \quad (18)$$

$$\rho \frac{\partial^2 u_i}{\partial t^2} = \sum_j \frac{\partial T_{ij}}{\partial x_j}, \qquad i, j = 1,2,3. \quad (19)$$

In case of piezoelectric medium elastic waves travel much slowly than the electromagnetic waves. Hence the magnetic field due to these waves is negligible and electric field can be expressed using quasi static approximation. Thus Maxwell equation can be approximated as

$$\text{curl}\, E = -\frac{\partial \mathbf{B}}{\partial t} = 0, \quad \mathbf{E} = -\text{grad}\, V \tag{20}$$

where, **B** is the magnetic field, **E** is the electric field derived from the scalar electric potential V [3].

$$E_i = -\frac{\partial V}{\partial x_i} \tag{21}$$

From equations (13), (15) and (21) the equation of motion for piezoelectric material can be expressed as [3]

$$\rho \frac{\partial^2 u_i}{\partial t^2} = \sum_j \sum_k \left\{ e_{kij} \frac{\partial^2 V}{\partial x_j \partial x_k} + \sum_l c^E_{ijkl} \frac{\partial^2 u_k}{\partial x_j \partial x_l} \right\} \tag{22}$$

In addition, the material is taken to be an insulator there are no free charges. Thus div D = 0. From equation (17)

$$\sum_i \sum_j \left\{ \varepsilon^S_{ij} \frac{\partial^2 V}{\partial x_i \partial x_j} - \sum_k e_{ijk} \frac{\partial^2 u_j}{\partial x_i \partial x_k} \right\} = 0 \tag{23}$$

The degrees of freedom (dependent variables) are the global displacements u_1, u_2, and u_3 in the global x_1, x_2, and x_3 directions, respectively, and the electric potential V can be obtained by solving the equations (22) and (23) using appropriate boundary conditions [3].

2.6.4 Solution of surface wave in piezoelectric media

The detailed description for finding the solution of surface waves in isotropic and anisotropic materials is well explained in [3] and [12]. In this section, the boundary conditions and solutions for surface waves on a piezoelectric medium are briefly elaborated. In case of piezoelectric crystal, care has to be taken in specifying the orientation of the material. For crystalline material, the uppercase X, Y, and Z with directions is defined by convention in relation to the crystal lattice. For example in case of Y cut Z propagating lithium niobate (Y–Z

cut $LiNbO_3$) material x_3 is parallel to crystal Y axis and x_1 is parallel to crystal Z axis. The orientation of x_3 is also referred to as cut, so that for Y–Z cut $LiNbO_3$ the crystal is Y cut. The material tensors stiffness, permittivity and piezoelectric tensors are specified in relation to the X, Y, and Z axes. The literature normally provides X-Y material tensors. For analysis they must first to be rotated into the frame defined by x_1, x_2 and x_3 using tensor transformations. The algorithms for these transformations are well documented in [29] and also given in the Appendix B of this thesis.

The appropriate boundary conditions should be applied in order to determine the phase velocity and amplitude of the wave [3]. Normally, two cases are considered. The first case is called as free surface case where the space above the surface of piezoelectric material is a vacuum and no conductor is present, so that there are no free charges. The second case is called as metalized case where the surface of piezoelectric material is covered with thin metal layer with infinite conductivity and short outs the horizontal components of the electric field **E** [3]. These two cases give different surface wave velocity and measure the coupling between wave and electrical perturbation at the surface. For free surface case, if the wave number of the surface wave is β then the potential in vacuum $\left(x_3 \geq 0\right)$ (see Figure 2.10) using Laplace's equation can be expressed as

$$V = V_0 e^{\left(-|\beta| x_3\right)} e^{j(\omega t - \beta x_1)} \tag{24}$$

where, V_0 is a constant. For metalized surface case the potential at $x_3 = 0$ is zero. In addition, the mechanical stress for either case at $x_3 = 0$ is given as

$$T_{13} = T_{23} = T_{33} = 0 \tag{25}$$

For surface wave solutions in piezoelectric medium, let us consider the partial waves in which the displacements and potential is denoted by $\mathbf{u}'$ and V', take the form

$$\mathbf{u}' = \mathbf{u}_0' e^{\left(j\gamma x_3\right)} e^{j(\omega t - \beta x_1)} \tag{26}$$

$$V' = V_0' e^{\left(j\gamma x_3\right)} e^{j(\omega t - \beta x_1)} \tag{27}$$

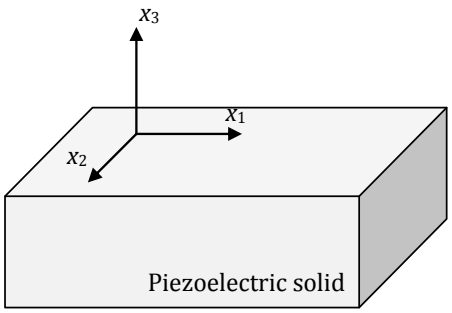

Figure 2.10 Axes for surface wave solution.

where, β is the wave number of the surface wave, assumed to be real. These expressions are to satisfy the equations (22) and (23). By substituting equations (26) and (27) in equations (22) and (23) and these equations are then solved for γ numerically and it gives eight solutions for γ. Consequently, for every solution of γ the relative solutions of $\mathbf{u}'$ and V' are obtained. The partial waves expression for normally considered values of γ are therefore,

$$\mathbf{u}'_m = \mathbf{u}'_{0m} e^{(j\gamma_m x_3)} e^{j(\omega t - \beta x_1)}, \qquad m = 1,2,3,4. \tag{28}$$

$$V'_m = V'_{0m} e^{(j\gamma_m x_3)} e^{j(\omega t - \beta x_1)}, \qquad m = 1,2,3,4 \tag{29}$$

where, $\mathbf{u}'_{0m}$ is the displacement and V'_{0m} is the potential corresponding to γ_m. For half-space a linear sum of these partial waves is assumed as

$$\mathbf{u} = \sum_{m=1}^{4} A_m \mathbf{u}'_m \tag{30}$$

$$V = \sum_{m=1}^{4} A_m V'_m \tag{31}$$

where, A_m is the coefficients such that the solution satisfies the electrical and mechanical boundary conditions for free surface case and metalized surface case. The surface velocity can be determined by ω/β, and displacement and potential are $\mathbf{u}$ and V given by equations (30) and (31) [3].

2.7 Finite element method (FEM)

The finite element method (FEM) is a numerical technique for solving differential equations or integral equations used in almost every discipline of engineering particularly in the areas of stress/strain analysis of solid structures, heat conduction analysis and fluid dynamics. The propagation of SAW governed by differential equations given in equations (22) and (23) must be solved along with complexities in geometry of device, materials used in the device, and proper boundary conditions. This section gives some basic procedures and techniques used in finite element method formulations. The detailed descriptions can be found in [30] and [31].

2.7.1. Input and output information in FEM

In FEM, the following input information about the structure that to be analyzed is given.

1. The geometry of the structure to be solved.
2. Coordinate systems according to the geometry in 3D or 2D.
3. Properties of the materials used in the model. For example, in SAW devices material properties of the piezoelectric substrate such as elasticity matrix, piezoelectric constant, permittivity constant, and density are to be furnished and for IDT electrodes an isotropic material properties such as Young's modulus, density, Poisson ratio, etc. are to be provided.
4. Boundary conditions at the boundaries of the structure are to be provided. For example in case of stress/strain analysis for piezoelectric material, the boundary conditions can be

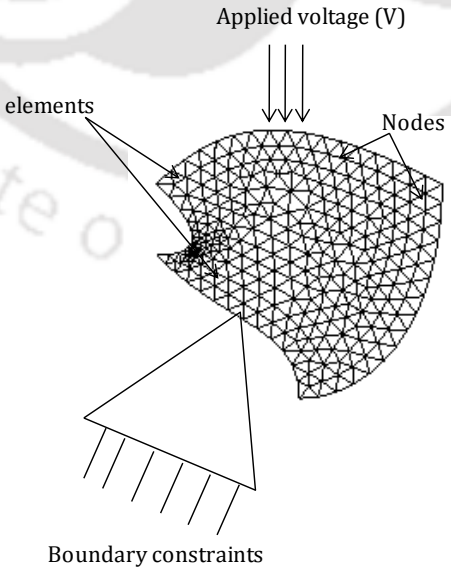

Figure 2.11 Illustration showing a solid body discretized into finite number of elements.

displacement constraints and electric boundary conditions such as electric potential, electric displacement, charge etc.

Further the geometry domains are to be divided into smaller domains called elements which are connected at specific points called nodes as shown in Figure 2.11. The elements created in the geometry can be in the shape of triangular, quadrilateral, tetrahedral, or brick depending on the dimensionality. The output information in case of stress/strain analysis in piezoelectric material involves nodal and elemental information, the solution to the primary unknown quantities, the displacements in all directions, and voltage are determined at nodes. These unknowns are called as degrees of freedom (DOF).

In this thesis, the simulations and analysis of SAW devices are carried out by FEM using piezoelectric module of COMSOL Multiphysics software. The software has well developed solvers, graphical user interface (GUI) and post-processing capabilities. More details of the software can be found in the user guide of the software [15].

2.7.2. Finite element simulation of SAW devices

Simulations of conventional SAW devices using FEM have been reported by many researchers. Some of them are given below. Lerch *et al*. [32] presented an FEM scheme to calculate Eigen modes, and dynamic response to mechanical and electrical excitations of 2D and 3D piezoelectric transducer for any geometry. Rahman *et al*. [33] performed FEM simulation to study SAW based quantum devices. Atashbar *et al.* [34] simulated the mass loading effect of palladium sensing film in the presence of hydrogen gas. Wu *et al.* [35] used Taguchi method on FEM results and established robust design processes for SAW sensors based on the mass loading principle. Ippolito *et al*. [36] performed the FEM based analysis of acoustic waves propagating on layered SAW devices. Wang *et al*. [37] used FEM carry out a study on the effects of change in film properties on the mass sensitivity of SAW sensors. Xu [38] reported FEM based simulation of a SAW filter. Tikka *et al.* [39] reported the finite element modeling of SAW correlator. Subraminian *et al*. [40] used FEM based simulation to design SAW device suitable in remotely readable microaccelerometers. Hamidon *et al.* [41] reported the finite element method on massloading in gallium phosphate surface acoustic wave resonators. In most of the earlier works, the number of DOF to solve is large due to the large size of the SAW structures considered in the model. In order to solve DOF for an entire SAW device, it requires high computing facility and large computation time. Thus a valid approximation and

simplified model are required to perform FE simulation of SAW devices. In this chapter, the conventional SAW devices such as one port SAW resonators and SAW delay line devices are simulated to verify the mass loading effects, electrical loading effects, bulk acoustic wave (BAW) generation, and other secondary effects due to the presence of metallic IDT on the piezo-substrate using COMSOL Multiphysics.

2.8 Simulation for mesh optimization and free surface SAW propagation

The free surface phase velocity of SAW in a piezo-substrate is the characteristics of the substrate and can be regarded as the velocity reference. The free surface phase velocity of SAW in YZ $LiNbO_3$ is calculated as follows using COMSOL Multiphysics. The piezo-substrate material constants such as elastic constants, permittivity constants, stress constants, and density are taken from [42] and are also listed in Appendix C. 2D piezo plain strain module is used for which degrees of freedom are u, v and V. SAW wavelength λ of 16 μm and piezo-substrate depth of 10 λ, is taken for the simulation. The eigenmode analysis provided by COMSOL Multiphysics is used to calculate the eigenmode frequencies of the model. The stress free boundary conditions are applied to all over the boundary of substrate sub-domains except bottom boundary which is kept fix. Periodic boundary conditions are applied for the section of length λ along the piezo-substrate. The expressions for the periodic boundary conditions are given below.

$$U_{left} = (-1)^n U_{right}$$
$$V_{left} = (-1)^n V_{right} \quad (32)$$

U_{left} and V_{left} are the displacement and potential at the left side of boundaries, respectively, and U_{right} and V_{right} are the displacement and potential at the right side of boundaries, respectively. Here, $n = 2w/\lambda$, w is the width of the substrate along the direction of wave propagation and λ is the SAW wavelength. In simulation the value of n is 2. The eigenmode analysis is performed without applying any driven voltage to the model. The eigenmode analysis of the model gives the edges of the stop band [23], [43]. The lower edge frequency is called as resonance frequency f_{sc-} at which the vibration occurs constructive and upper edge frequency is called as anti-resonance frequency f_{sc+} at which the vibration occurs destructive [22], [43]. No propagation of waves occurs in the substrate in this band of frequency [23]. In terms of displacement profile, at resonance frequency the displacement is max at the edge of the resonator while at anti-resonance frequency the displacement is max at the middle of the finger. The displacement profiles of eigenmodes are shown in Figures 2.12 (a) and (b).

The SAW phase velocity of the device in the presence of metallic IDT over the piezo-substrate can be calculated as given below [23].

$$v = p\left(f_{sc+} + f_{sc-}\right) \tag{33}$$

In case of free surface of piezo-substrate both eigenmodes fall at one frequency (see Figure 2.11). The number of mesh elements per wavelength is optimized as follows. The SAW phase

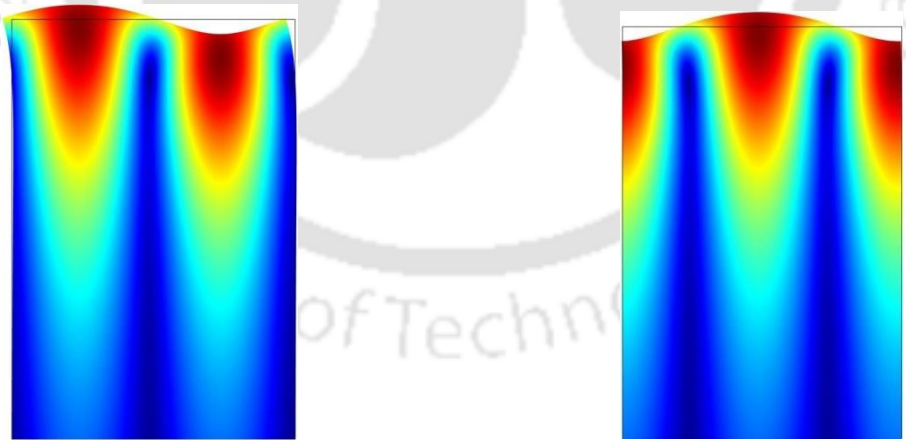

(a) (b)

Figure 2.12 Total displacement profile for a section of length λ = 16 µm of YZ $LiNbO_3$ (a) at eigenmode frequency of 217.369642 MHz (f_{sc-}) showing anti-resonance mode, (b) at eigenmode frequency of 217.369630 MHz (f_{sc+}) showing resonance mode. Note: For simplicity the substrate depth shown is 1.25 λ.

velocities of substrate for SAW wavelength of 16 μm is calculated for various number of mesh elements per wavelength through eigenmode analysis. The SAW phase velocity for different

TABLE 2.1

SAW PHASE VELOCITY AGAINST NUMBER OF MESH ELEMENTS

No. of mesh elements per λ	Resonance frequency for $\boldsymbol{\lambda}$ = 16 μm (MHz)	Velocity v_0 (m/s)
8	217.448921	3479.183
12	217.386285	3478.181
16	217.374817	3477.997
20	217.371586	3477.945
24	217.370407	3477.927
28	217.369885	3477.918
32	217.369630	3477.914
36	217.369493	3477.912
40	217.369414	3477.911
44	217.369366	3477.910
48	217.369335	3477.909

number of mesh elements is shown in Table 2.1.

It is observed from Table 2.1, that the increase in number of mesh elements gives the accurate solutions and SAW phase velocity remains unchanged beyond 44 mesh elements per wavelength. The identical model with SAW wavelength of 4 μm is simulated to validate the result and the response is turned out to be identical. Table 2.2 shows the SAW phase velocities of substrate for SAW wavelength of 4 μm for various number of mesh elements per wavelength. The plot of SAW phase velocity as a function of number of mesh elements per wavelength for the SAW wavelength of 4 μm and 16 μm is shown in Figure 2.13.

A mesh size of 32 elements per wavelength gives an error of 295 Hz (0.00014%) in frequency which is negligible with respect to frequency obtained from a mesh size of 48 elements per wavelength which is maximum possible with the available computational resources. Hence we have used 32 elements per wavelength for all the simulations.

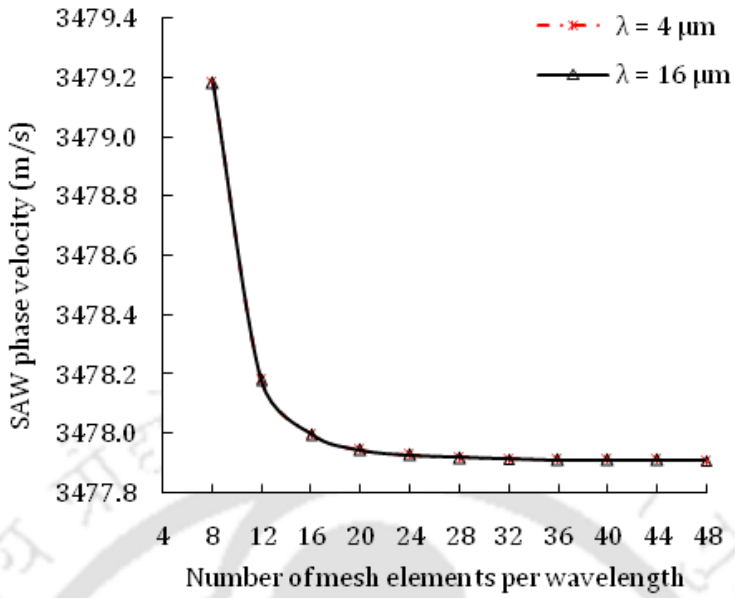

Figure 2.13 SAW phase velocity as a function of number of mesh elements per wavelength.

TABLE 2.2

SAW PHASE VELOCITY AGAINST NUMBER OF MESH ELEMENTS

No. of mesh elements per λ	Resonance frequency for $\boldsymbol{\lambda}$ = 4 μm (MHz)	Velocity v_0 (m/s)
8	869.795685	3479.183
12	869.545139	3478.181
16	869.499269	3477.997
20	869.486346	3477.945
24	869.481627	3477.927
28	869.479541	3477.918
32	869.478519	3477.914
36	869.477972	3477.912
40	869.477656	3477.911
44	869.477463	3477.910
48	869.477340	3477.909

2.9. Simulation of conventional one port SAW resonator based on FEM in 2D

As explained in chapter 1 section 1.3, one port SAW resonator can be designed by large number of IDT finger-pairs where multiple reflections occur between the fingers or by using reflectors either side of a short IDT having less number of fingers [6], [22]. The simulations of conventional SAW resonators by FEM are presented by many researchers [41], [44], [45], however, we simulate it to compare the results of conventional SAW resonator with the results of the proposed SAW resonator.

2.9.1 Simulation methodology

A conventional one port SAW resonator with infinite number of IDT fingers on a piezo-substrate is considered for the simulation. Owing to the periodic nature of IDT structure, one pair of IDT fingers is used and appropriate boundary conditions are applied. 2D geometry of a periodic segment of the resonator considered for the simulation is shown in Figure 2.14. The dimensions used for simulations are as follows: electrode width (d) 4 µm, electrode pitch (p) 8 µm, depth of the piezo-substrate 160 µm (10 λ), and thickness of IDT fingers 0.2 µm. YZ $LiNbO_3$ piezoelectric material is used as a piezo-substrate. The values of elastic constants, permittivity constants, stress constants, and density are given in Appendix C. The bottom surface of the piezo-substrate is kept fix and all other boundaries are stress free. The degrees of freedom of the right periodic boundary (Γ_R) are set to be equal to those from the left periodic boundary (Γ_L) (see Figure. 2.14). In general, the expressions for the periodic boundary conditions are given in equation (32). An alternative driven voltage of 1 V is applied to the IDT fingers. An extremely fine mesh with minimum element quality of 0.7 with 32 mesh elements of per wavelength is adopted for the 2D simulation. The number of degree of freedom solved is in the order of around 2×10^5. The harmonic analysis is performed to find the characteristics and parameters of the resonator.

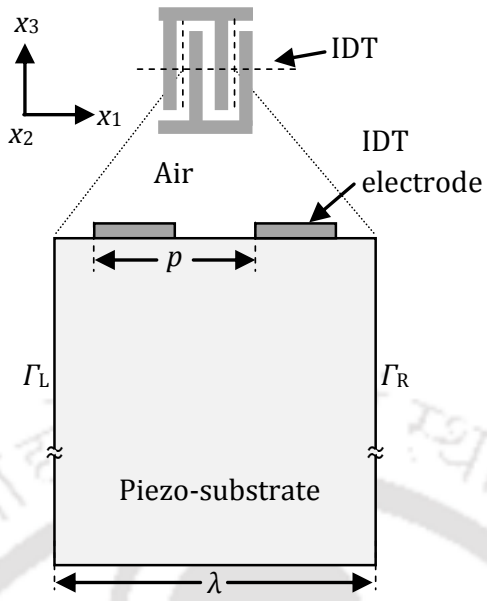

Figure 2.14 2D Geometry of the periodic section used for the simulation.

2.9.2 Results and discussions

The results of simulation of conventional SAW resonator are shown in Figure 2.15 and Figure 2.16. The total displacement profile, *x*-displacement profile and *y*-displacement profile of the resonator at the resonance frequency f_r of 212.8801 MHz are shown for substrate depth of about 3.75 λ in Figures 2.15 (a), (b) and (c), respectively. The substrate depth of 3.75 λ is shown for simplicity. It is shown in Figure 2.15 that the displacement is approaching zero after 1 λ depth of the substrate, which depicts the nature of Rayleigh wave SAW. The resonance frequency of the resonator is identified as the frequency for which the susceptance crosses zero value. The plot of total displacement as a function of normalized frequency given in Figure 2.16(a) shows peak at the resonance frequency. The normalized frequency is expressed as $\eta = 2pf/v_0$, where, v_0 = 3477.914 m/s is the free surface velocity of the substrate as calculated in section 2.8. The curves of harmonic admittance per period as a function of normalized frequency for conventional SAW resonator are shown in Figures 2.16 (b) and (c). The harmonic admittance per period of NCIDT SAW resonator is measured at the IDT electrodes [22], [46], [47].

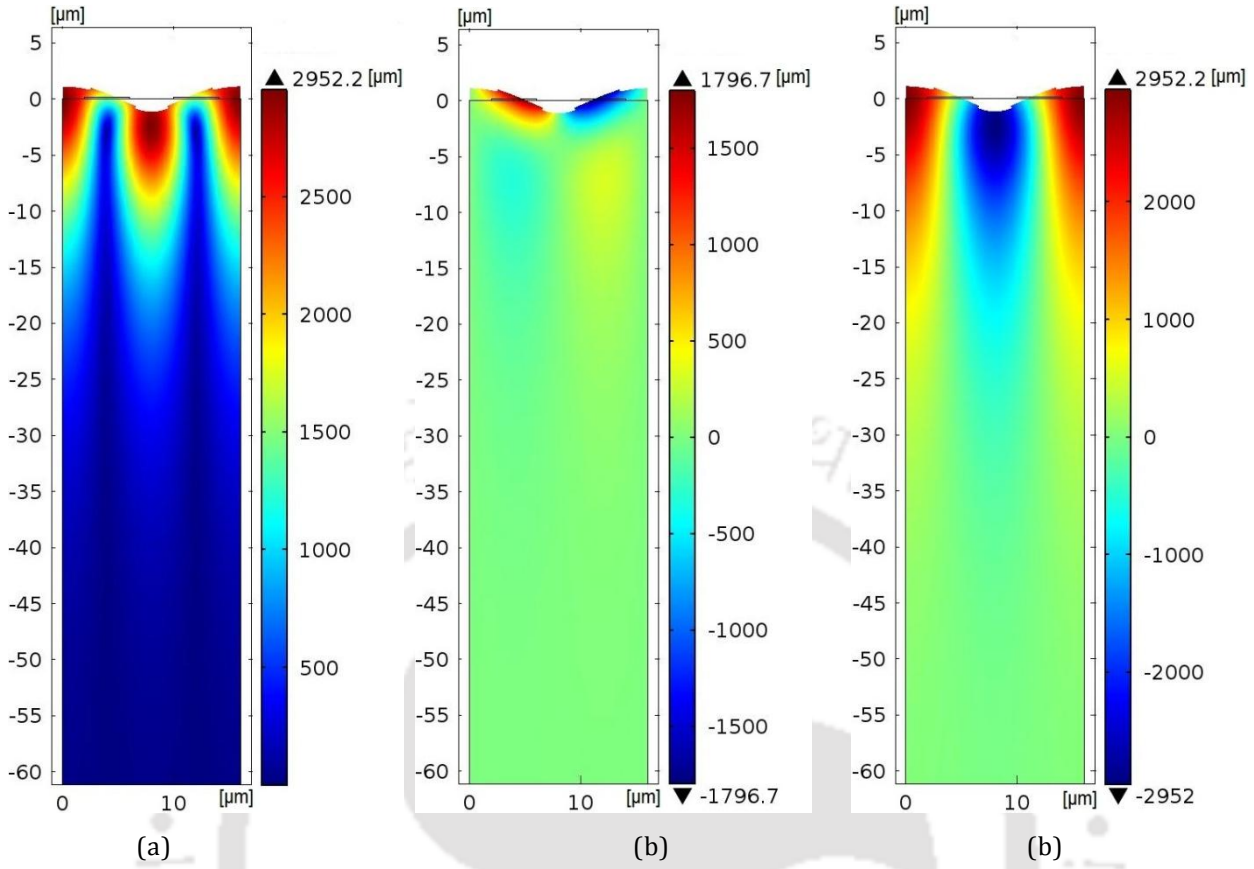

(a) (b) (b)

Figure 2.15 Displacement profile in a SAW resonator at resonance frequency 212.8801 MHz with deformed shape, (a) Total displacement profile, (b) *x* displacement profile, (c) *y* displacement profile. Note: For simplicity the substrate depth shown in the Figure is about 3.75 λ.

Figure 2.16(b) shows the closer view of curve of harmonic admittance per period as a function of normalized frequency near the resonance frequency. Figure 2.16(c) shows the curve of harmonic admittance per period as a function of normalized frequency which includes both the resonance and anti-resonance frequencies. The value of harmonic admittance is around 10^6 S at resonance frequency. In the case of real device, it would be lower due to finite aperture, attenuation and damping. This simulation does not consider the attenuation or damping and assumes infinite width of the aperture of IDT fingers in x_2 direction.

The free surface resonance frequency f_0 calculated from the eigenmode analysis of the piezo-substrate is 217.3696 MHz. With reference to f_0, the resonance frequency of the conventional SAW resonator is 4.4895 MHz lower. The resonance frequency is affected by the mechanical and electrical properties as mass loading and conductivity of the metallic IDT fabricated on

the piezo-substrate affects SAW phase velocity and it requires consideration to these factors while designing [4], [9]. The simulations related to secondary effects are given in section 2.12.

The quality factor Q_r at resonance frequency of the convention SAW resonators is calculated from Figure 2.16(b). The expression for quality factor is given as [22], [48]

$$Q_r = \frac{f_r}{\Delta f} \tag{34}$$

where, Δf is the bandwidth at half of the peak-conductance [22], [48] (see Figure 2.16(b)). The quality factor of the conventional SAW resonator computed from simulation is 168151757. The capacitance ratio which is a measure of the resonator performance is calculated from Figure 2.16(c). The capacitance ratio γ is expressed as [22]

$$\gamma = \frac{f_r^2}{f_a^2 - f_r^2} \tag{35}$$

where, f_a is anti-resonance frequency (see Figure 2.16(c)). The capacitance ratio for the conventional SAW resonator computed from simulation is 28.

2.10. Simulation of conventional one-port SAW resonator based on FEM in 3D

The results in the previous section are obtained with 2D FEM by considering infinite aperture of IDT fingers. In this section, a conventional SAW resonator with finite aperture having infinite number of IDT fingers with a simplified model is simulated. For 3D simulation, piezo solid application mode of COMSOL Multiphysics is used. One pair of periodic IDT fingers is used for the simulation. The dimensions used for 3D simulation are the same as 2D simulation except the depth of piezo-substrate h_s and aperture W. The depth of piezo-substrate is truncated to 5 λ since SAW energy concentrates near the substrate depth of one wavelength. The simplified model is used to reduce the number of nodes and reduce computation cost. The material constants used for the simulation are given in Appendix C. The bottom surface of the substrate is fixed and all other boundaries are stress free. It is possible by modeling a thin

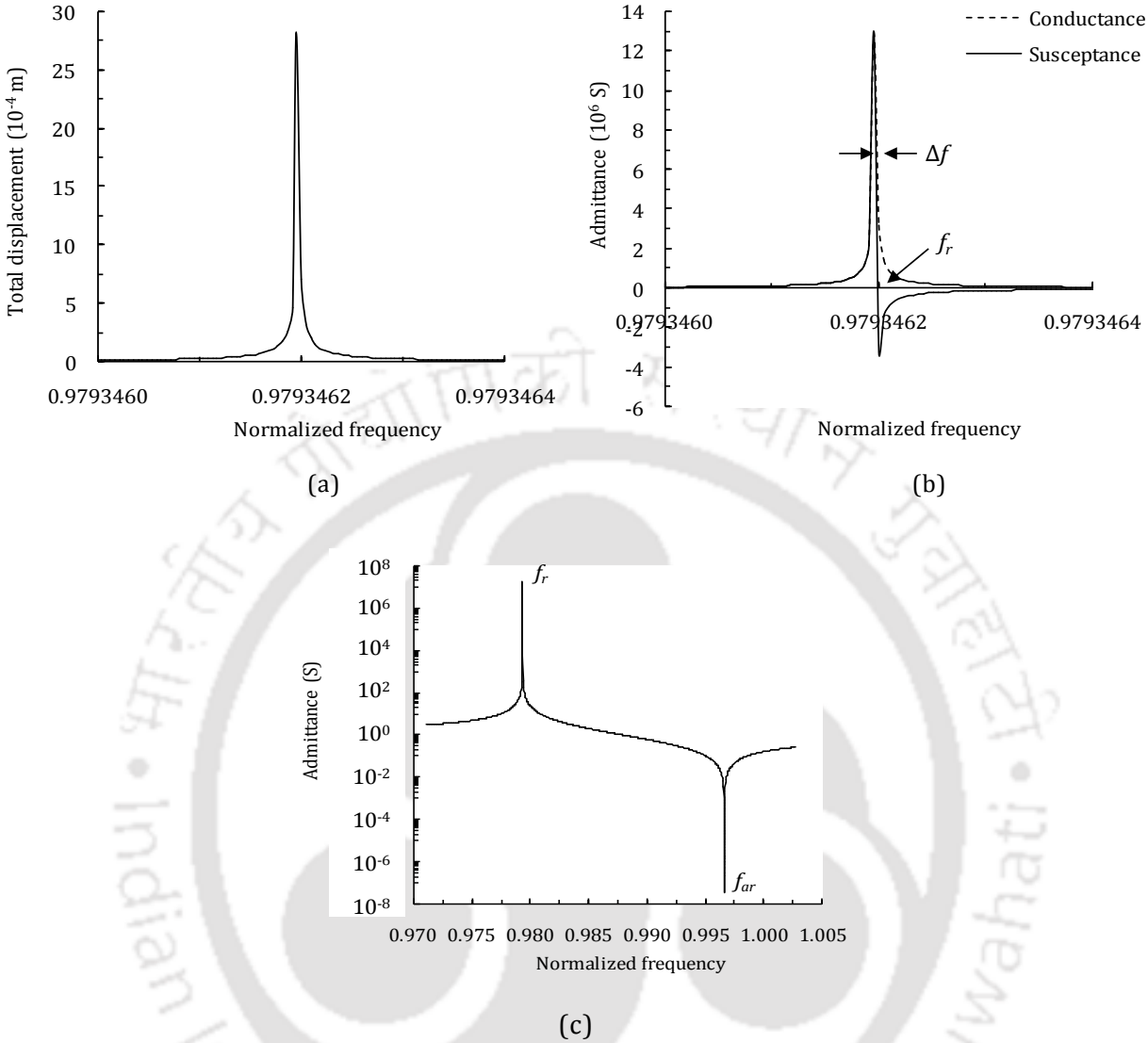

Figure 2.16 Results of simulation of a SAW resonator, (a) Plot of total displacement as a function of normalized frequency, (b) Plot of harmonic admittance as a function of normalized frequency, (c) Plot of harmonic admittance in log scale as a function of normalized frequency.

strip of thickness of W in x_2 direction and applying zero displacement constraint in the x_2 direction on the both side boundaries normal to the direction of wave propagation. Rayleigh SAW has no variation and no component of displacement vectors in x_2 direction [41]. The periodic boundary condition is applied to left (Γ_L) and right (Γ_R) sides of the periodic section as given in section 2.8. The eigenmode analysis is performed to compute the resonance frequency of the SAW resonator. Table 2.3 shows the resonance frequency and anti-resonance frequency of conventional SAW resonator against various values of W.

TABLE 2.3
VARIATION IN RESONANCE FREQUENCY WITH APERTURE *W*

Aperture *W* (μm)	Resonance frequency (MHz)	Anti-resonance frequency (MHz)
2	212.143	214.441
3	212.131	214.439
4	212.119	214.433
6	212.079	214.386
8	212.050	214.375

The resonance frequency is identified from the list of eigenmode frequencies and their displacement amplitude, the mode of vibration and the charge distribution on the IDT fingers are studied. At resonance frequency the displacement is maximum between the fingers of the resonator while at anti-resonance frequency the displacement is maximum in the middle of the finger as given in section 2.8. The charge distribution is symmetry and antisymmetry at resonance and antiresonance frequencies.

The harmonic analysis of 3D model SAW resonator is performed for various values of *W*. Figures 2.17 (a), (b) and (c) show the total displacement, *x* displacement and *y* displacement profile with deformed shape of 3D model SAW resonator at resonance frequency, respectively. The plots of harmonic admittance as a function of normalized frequency for aperture widths of 4 μm and 6 μm are shown in Figure 2.18. The harmonic admittance value at resonance calculated for this model is in the order of 10^{-2} S. It is observed that the value of harmonic admittance for given aperture is proportional to the aperture width. Thus the minimum aperture length is adequate to simulate a SAW resonator to study the resonance frequency, harmonic admittance and other parameters of the resonator. By this way one can minimize the computational cost as mentioned in the section 2.7.

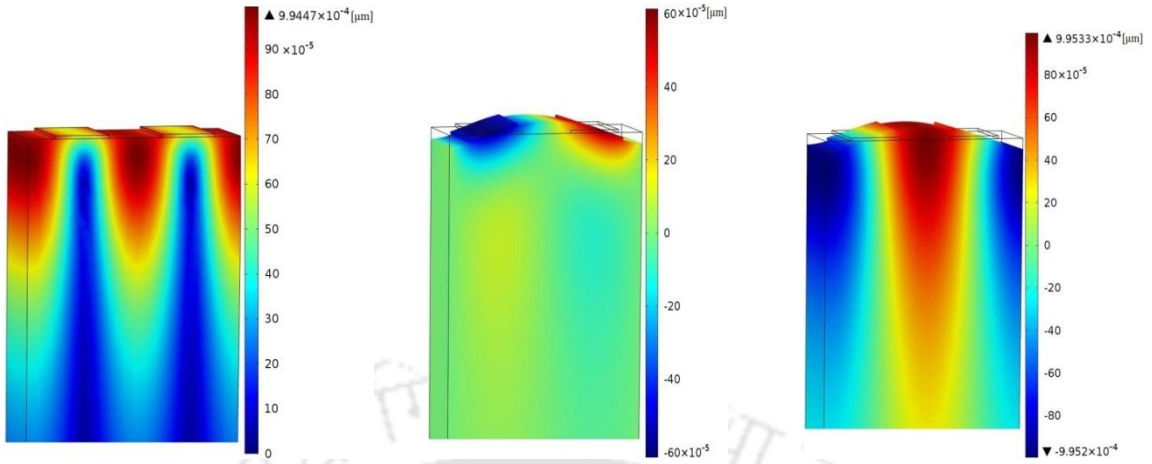

(a) (b) (c)

Figure 2.17. Displacement profiles at resonance frequency 212.119 MHz, (a) Total displacement profile, (b) *x* displacement profile with deformed shape, (c) *y* displacement profile with deformed shape. Note: For simplicity the substrate length shown in the Figure is 1.75 λ.

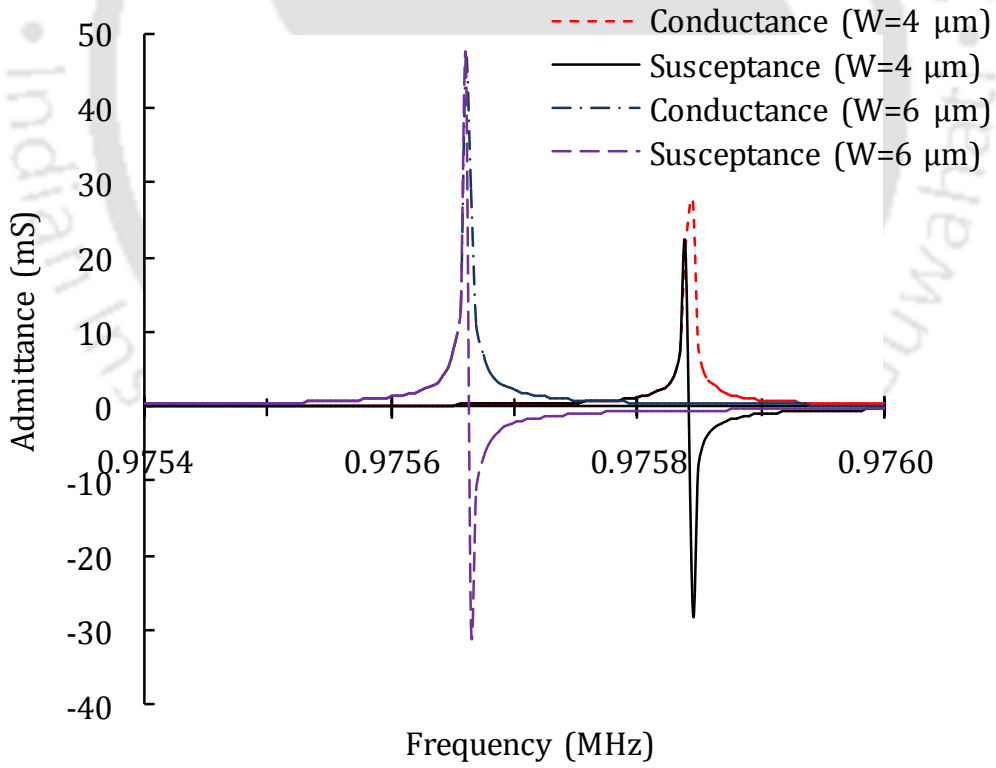

Figure 2.18 Harmonic admittance as a function of normalized frequency for aperture *W* of 4 µm and 6 µm.

2.11 Simulation of a conventional SAW delay line

The conventional SAW delay line device has been simulated using FEM by many researchers [34], [49], [50]. In this section, a conventional SAW delay line device is simulated to compare the simulation results with the proposed SAW delay line device configuration described in the next chapter.

2.11.1. Simulation methodology

A SAW delay line device with delay of 3 λ (λ = 4 μm) is simulated by FEM using COMSOL Multiphysics. In this simulation, three pairs of IDT fingers for transmitter IDT and receiver IDT fabricated at the two ends of the piezo-substrate are considered. The dimensions used for simulations are as follows: electrode width (d) 1 μm, electrode pitch (p) 2 μm, depth of the piezo-substrate 40 μm (10 λ), and thickness of IDT fingers 0.2 μm. YZ $LiNbO_3$ piezoelectric material is used as a piezo-substrate and aluminium metal is used as IDT electrodes. The values of elastic constants, permittivity constants, stress constants, and density are given in Appendix C. 2D geometry of SAW delay line device used for simulation is shown in Figure 2.19. Following boundary conditions are applied to the model. The top surface of the substrate is assumed stress free and bottom surface is fixed in its position. The critical damping is assumed at the edge of the transmitter B_L, receiver B_R, and bottom of the substrate B_B to avoid reflections of the acoustic waves as shown in Figure 2.19. The equations relating to critical damping are provided in Appendix D. The alternate fingers are shorted and 1 V sinusoidal driven voltage of its resonance frequency is applied. The resonance frequency is about 840 MHz. An optimized mesh density is used for the simulation. To analyze the propagation of SAW over the delay line, transient analysis is performed using direct solver

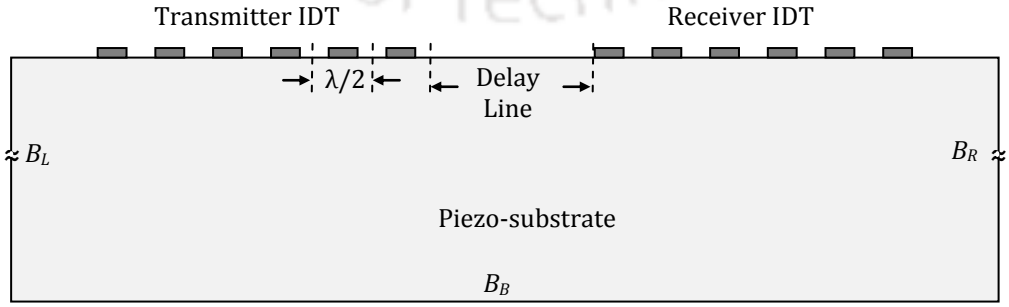

Figure 2.19 2D schematic of the SAW delay line device used in simulation.

SPOOLES available in COMSOL Multiphysics [15] with the time interval of 0.1 ns for duration up to 10 ns. The displacements and potential at the receiver electrode are recorded at every instant.

2.11.2. Results and discussions

The transient analysis of SAW delay line device is performed for the time duration of 15 ns. Figure 2.20 (a) shows the total displacement profile of SAW delay line device at time 10 ns. The output electrical potential, *x* displacement and *y* displacement is measured at the receiver IDT electrodes. The plots of output potential, *x* displacement and *y* displacement as a function of time are shown in Figures 2.8 (b), (c) and (d). The output electric potential 0.3 V is obtained at the receiver IDT electrodes. In SAW delay line device, delay time is one of the important parameter. The instant of signal arrival at the receiver is estimated from the envelope of the waveform shown in Figure 2.20 and the delay time is about 3.50 ns. The delay time calculated from the free surface velocity of 3478 m/s is 3.45 ns. *x* displacement and *y* displacement of about 3×10^{-11} m and 5×10^{-11} m are obtained at time 10 ns. An identical SAW delay line device with proposed configuration is simulated in chapter 3 and the results are compared. In addition, the delay line device is used to study the effects of BAW generation in SAW device.

2.12 Secondary effects of IDT fabricated on piezo-substrate

The intuitive presentation of IDT assumes an ideal operation of an IDT [4]. In practice, it gives several secondary effects that affect the propagation of SAW and response of SAW devices. The major effects are mass loading, electrical loading, dispersion, BAW generation, reflections, reemission, diffraction, phase speed variations, electromagnetic feed through [4]. The main cause of these secondary effects in conventional SAW devices is the presence of metallic IDTs on the piezo-substrate. The mechanical and electrical properties of metallic IDT are the major reasons of most of the secondary effects. The following sections describe the secondary effects in conventional SAW devices by FEM using COMSOL Multiphysics.

2.12.1 Simulation to study the mass loading effects of IDT

The mechanical properties of IDT electrodes which are fabricated on the device substrate strongly affect the physical and electrical properties of the propagation of SAW in SAW

devices [7], [17]. Acoustic wave perturbs as it propagates under the IDT electrodes [17]. The presence of metallic IDT over the piezo-substrate gives mechanical loading or mass loading effects. The mass loading effects due to the presence IDT electrodes can be separated into three primary categories: inertial effects, energy trapping, and intrinsic stress [41], [23].

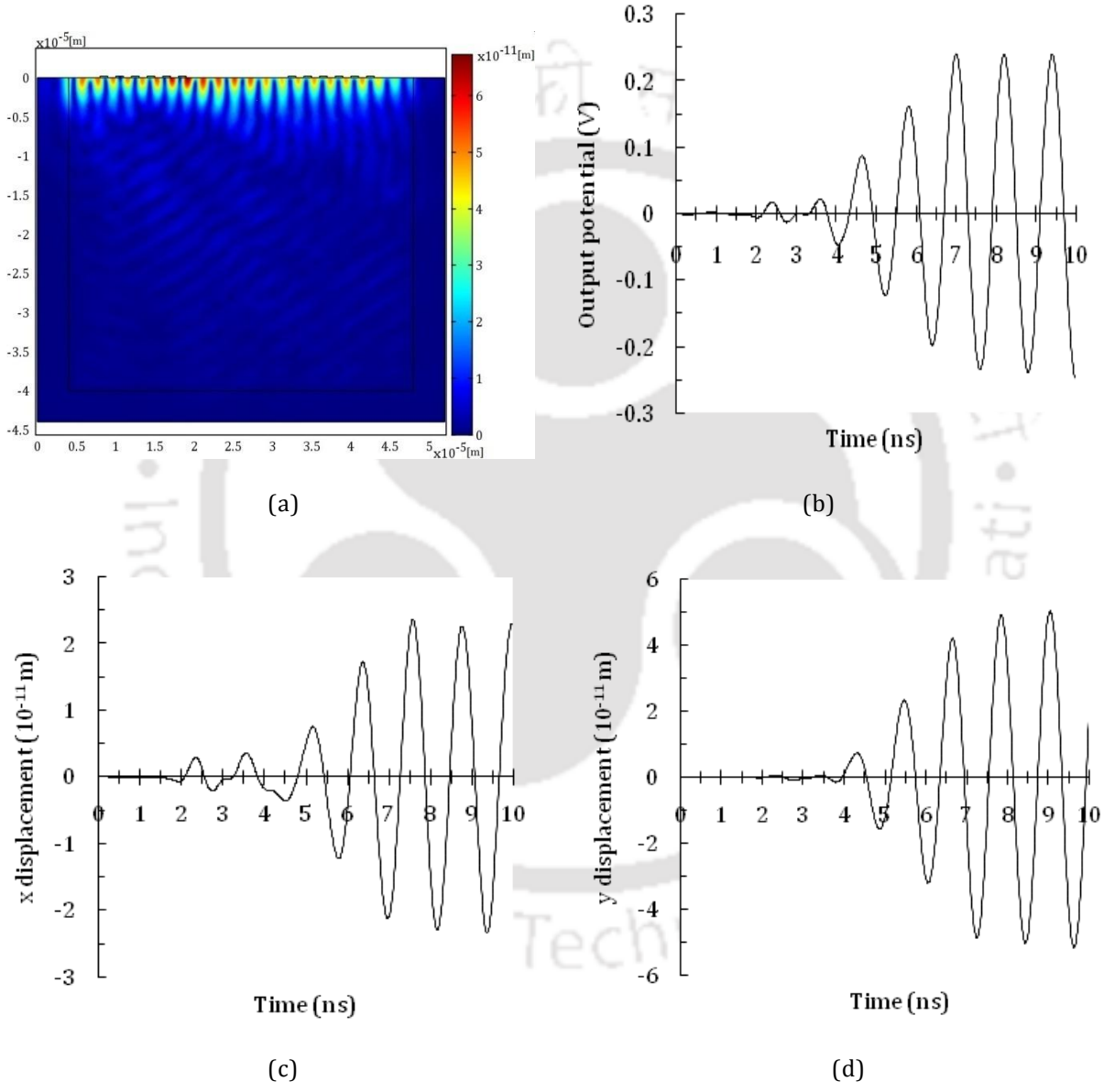

Figure 2.20 Results of simulation of a conventional SAW delay line device, (a) Total displacement profile at time 10 ns, and (b) Output electric potential, (c) *x* displacement, (d) *y* displacement at the receiver IDT.

Inertial effects caused by addition of mass to the surface of piezo-substrate provide a convenient means of frequency adjustment and are significant source of frequency aging due to contamination. In energy trapping, the mass loading combined with the size of the electrodes plays an important role in energy trapping under the electrodes [41], [51].

It creates the regions with different cut-off frequencies and it allows the confinement of acoustic energy. The number of trapped modes to only one can be controlled by controlling mass loading and electrodes dimensions. The final effect is due to intrinsic stresses in the electrodes layers and mechanical strains due to mismatch in thermal expansion of the electrodes and substrate interface [41]. At low temperature this effect is less than the other two effects. Accurate prediction of mass load due to IDT electrode is crucial for the development of high frequency devices. At high frequency the IDT electrode thickness is no longer negligible compared to the SAW wavelength. Consequently, the mass loading effects are significant and result in slowing of SAW and strong reflections [23]. The mass loading effect on SAW device response due to IDT electrodes is well-known and reported by many researchers [7], [41], [22], [23]. The velocity change due to loading effects of IDT can be expressed as a power series expansion on the relative electrode thickness h_e/λ as [23]

$$\frac{v-v_0}{v_0} \approx \left[\frac{\Delta v}{v}\right]_e + \left[\frac{\Delta v}{v}\right]_{m1}\left(\frac{h_e}{\lambda}\right) + \left[\frac{\Delta v}{v}\right]_{m1}\left(\frac{h_e}{\lambda}\right)^2 + \ldots\ldots\ldots \tag{36}$$

where, v_0 denotes the free surface SAW phase velocity. The expansion coefficients depend on the electrode geometry. The first term on the right side in equation (36) shows the electrical loading which is explained in subsection 2.12.2. The second and third terms show the linear shift in velocity due to mechanical loading. In practical case mass loading must be controlled to avoid undue dispersion [3]. The mass loading effect is well explained through Auld's perturbation theory [3]. In this section, a series of simulations of a one port SAW resonator with infinitely long IDT are performed to study the electrode mass loading effects. The SAW phase velocity is calculated for different metallization ratios and electrode thicknesses of IDT and change in SAW phase velocity is observed. The reduction in metallization ratio and thickness of electrodes are considered as reduction of mass loading on SAW device. The metallization ratio (MR) is defined as the ratio of width of the IDT finger d and pitch of the

IDT finger p, [11] as shown in Figure 2.21. The electrode thickness h_e is normalized with the SAW wavelength λ. The expression for MR is given below.

$$\mathrm{MR} = \frac{d}{p} \tag{37}$$

A one port SAW resonator of wavelength of 16 μm is simulated to study the effects of MR and electrode thickness on SAW phase velocity. The dimensions and boundary conditions used for simulation are as given in section 2.9. The eigenmode analysis is performed to find the SAW phase velocity for various MRs and electrode thicknesses. The SAW phase velocities for various MRs and electrode thicknesses are calculated using equation (33). The MR is varied from 0.0125 to 0.9 and thickness is varied from 0 to 0.6 μm. The normalized SAW phase velocity as a function of MR for various values of electrode thickness is shown in Figure 2.22 (b). The normalized SAW phase velocity is given as v/v_0 where, v is the velocity of SAW resonator for various values of MR and electrode thickness, and v_0 = 3477.914 m/s is the free surface SAW phase velocity as calculated in section 2.8. From Figure 2.22 (b) it is observed that the SAW phase velocity of the resonator decreases as the MR and electrode thickness increase.

A one port SAW resonator with massless IDT electrodes with different MR is simulated. The normalized SAW phase velocity as function of MR for massless IDT SAW resonator is given in Figure 2.22 (b). From Figure 2.22 (b), it is observed that the SAW phase velocity of SAW resonator with massless IDT electrodes is more than SAW resonator with metallic IDT electrodes. However the velocity is less than the free surface SAW phase velocity due to electrical loading effects.

The absolute value of the reflection coefficient per period $|\kappa_p|$ of SAW resonator is expressed as [23]

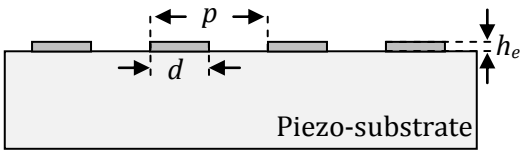

Figure 2.21 IDT metallization ratio and finger thickness.

$$\left|\kappa_p\right| = \pi \frac{f_{sc+} - f_{sc-}}{f_0} \tag{38}$$

where, f_0 is the center frequency of stopband of resonator. The absolute value of the reflection coefficient per period of one port SAW resonator for various values of MR and electrode thickness h_e is calculated. The reflection coefficient per period $\left|\kappa_p\right|$ as a function of MR for various values of electrode thicknesses is shown in Figure 2.22 (b). In order to get minimum reflection coefficient for a given MR a suitable electrode thickness can be chosen. This allows the design of IDT without internal reflections [52].

The effective electromechanical coupling coefficient K_{eff}^2 of SAW resonator is expressed as [53]

$$K_{eff}^2 = 2 \times \frac{f_a - f_r}{f_r} \times 100\% \tag{39}$$

where, f_a and f_r are the antiresonance and resonance frequency of the resonator [53].

The effective electromechanical coupling coefficient K_{eff}^2 as a function of MR for various values of electrode thickness is shown in Figure 2.22 (c).

The change in electrode width or MR influences the SAW phase velocity and reflection coefficient of the device. The increase in the MR reduces the phase velocity and increases the electromechanical coupling coefficient. By this way the antiresonance frequency f_a is also shifted. The change in electrode thickness causes the shift in resonance frequency f_r and change in electrode width results shift in both resonance frequency f_r and antiresonance frequency f_a [23].

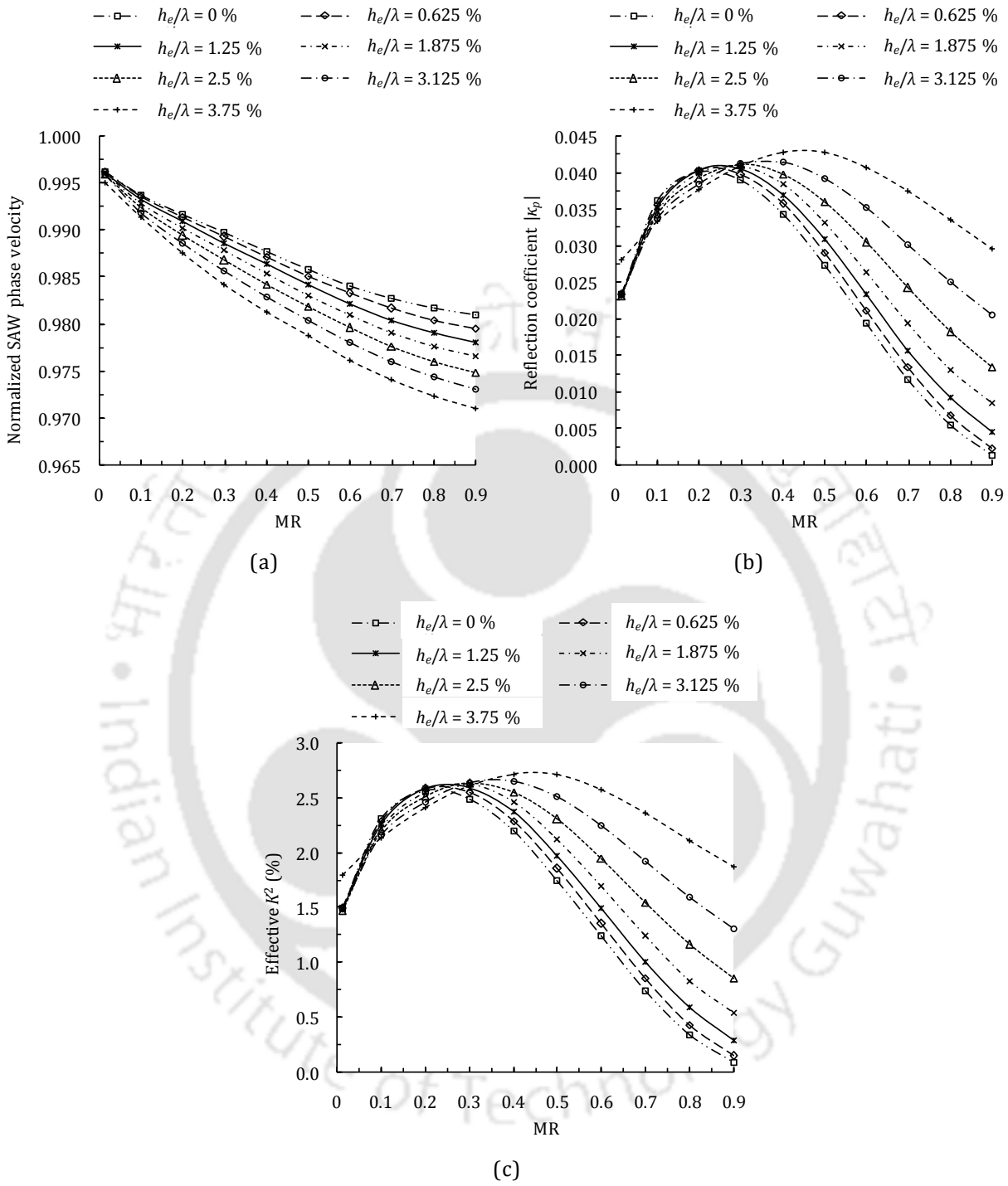

Figure 2.22 (a) Normalized SAW phase velocity as a function of MR at various electrode thicknesses h_e. (b) Absolute value of the reflection coefficient per period $|\kappa_p|$ as a function of MR at various electrode thicknesses. (c) Effective electromechanical coupling coefficient K_{eff}^2 as a function of MR at various electrode thicknesses.

2.12.2. Simulation to study the electrical loading effects of IDT

The metallic IDT fabricated over the piezo-substrate short-circuits the parallel components of the electric field associated with the SAW under the IDT electrodes [3], [7]. This effect is known as electrical loading [7]. As given in equation (36) the first term in the right side of the equation shows the electrical loading due to IDT electrodes [23]. The conductive electrodes short circuit the electric fields and slow the SAW velocity and energy flow in the wave. The term is roughly proportional to the piezoelectric coupling coefficient [3]. The perturbation theory estimates the change in velocity due to electrical loading as given below [3].

$$\frac{v-v_0}{v_0} \approx \frac{\left(\varepsilon_0 + \varepsilon_P^T\right)\left|\phi_s\right|^2 \omega}{4P_s} \tag{40}$$

where, $\varepsilon_P^T = \left[\varepsilon_{33}^T \varepsilon_{11}^T - \left(\varepsilon_{13}^T\right)^2\right]^{1/2}$ is the permittivity tensor for constant strain, ϕ_s is the surface potential associated with the wave, and P_s is the wave power per unit width in x_2 direction. The short circuit of surface electric field due to metallic thin conductor over the piezo-substrate is reported by many researches. Schulz *et al.* [54] reported the relative change in the SAW velocity caused by the thin conducting film on surface of several piezo-substrates. Vistini *et al.* [55] reported velocity dispersions in the bus bars and in transducers due to both mechanical and electrical loading. Morgan [3] reported the electrical loading in an array of regular electrodes and gave a simplified account of the work of Bløtekjaer *et al.* [56], [57]. This section describes simulation for the short circuit of electric field due to the presence of metallic IDT electrode on the surface of piezo-substrate by FEM using COMSOL Multiphysics. These simulation results are compared with the simulation results of proposed SAW device in chapter 3.

A conventional one port SAW resonator with massless IDT electrodes is simulated. The massless electrodes are considered to avoid the mass loading effects. The dimensions and boundary conditions used for this study of simulation are taken the same as used in section 2.9. Eigenmode analysis is performed to find the phase velocity of SAW. The phase velocity is calculated as given in equation (33). A series of eigenmode analysis of one port SAW resonator with massless electrode with different MR is performed. The electric field *x*-component associated with the surface wave is calculated at the surface of the device

substrate at resonance frequency. Surface electric field *x*-component calculated at the surface of the device substrate as a function of MR is shown in Figure 2.23 (a).

As theory implies, the application of sinusoidal electric potential on IDT generates sinusoidal deformation on the substrate thus the electric field distribution to the surface of the substrate should be sinusoidal. It is observed from simulation results shown in Figure 2.23 (a) that the surface electric field *x*-component under the IDT fingers is short-circuited due to conductive properties of the IDT electrodes (see Figure 2.23 (a)). Consequently, the resonance frequency of the device is reduced. However, the resonance frequency is more than the device with mass loaded IDT. The normalized resonance frequency versus MR of massless electrodes of one port SAW resonator is shown in Figure 2.23 (b). It is observed from Figure 2.23 (b) that for small values of MR of IDT electrodes, the resonance frequency of the resonator approaches to the resonance frequency calculated from the free surface SAW velocity, since the short circuit effect reduces with reduction in the relative metalized area. The resonance frequency calculated for λ = 16 μm with free surface SAW velocity of 3477.914 m/s is 217.3696 MHz.

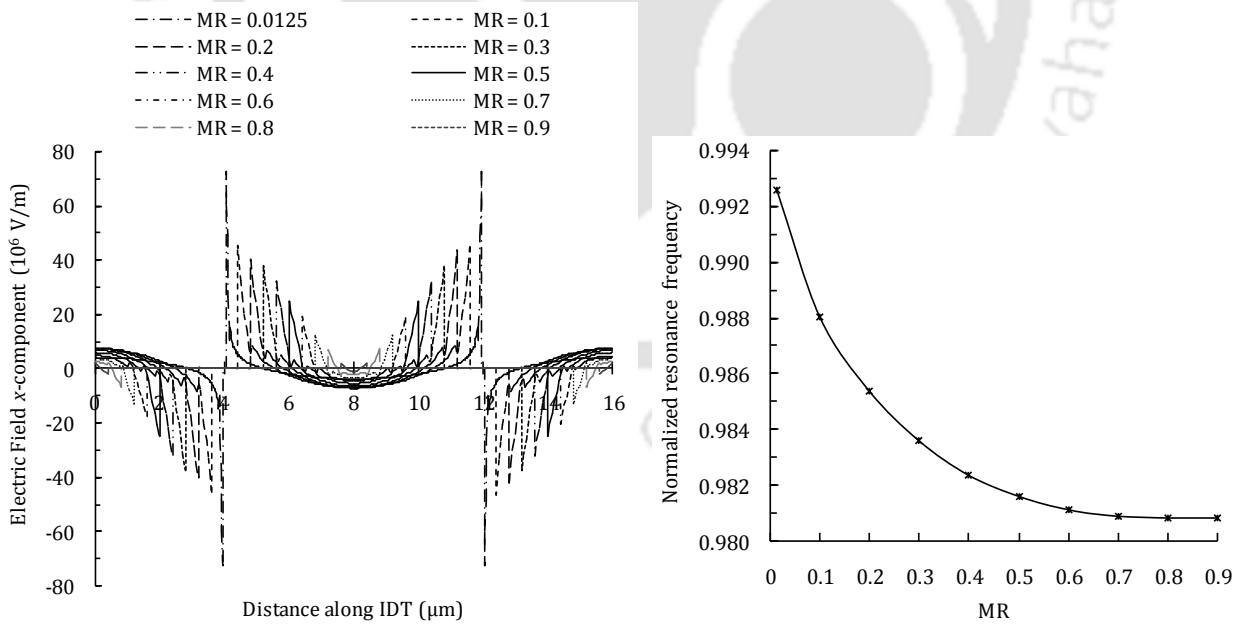

(a) (b)

Figure 2.23 (a) Plot of *x*-component of electric field along IDT for various values of metallization ratio MR. (b) Plot of normalized resonance frequency versus MR.

2.12.3. Simulation to study the generation of BAW

IDTs fabricated on the piezo-substrate generate not only SAW but also enhance BAW which propagates into interior of the piezo-substrate at an angle from the transducer such that the periodic electric field and bulk wave are in phase [4], [22], [58]. These waves are reflected from the bottom surface of the substrate and they are detected at the output IDT as a spurious response [22]. This type of BAW is called as deep bulk acoustic wave (DBAW). There is another kind of BAW which arrives at the output IDT without reflection from the bottom surface of the substrate and is called as surface skimming bulk wave (SSBW) [22]. The generation and effects of BAWs in SAW devices have been reported by following researchers. Milsom *et al.* [58] reported the radiation of BAW by IDT along with surface waves and distortion in the surface wave response. Honkanen *et al.* [59] studied the parasitic excitation of BAW in leaky SAW (LSAW) transducers at high frequency and proposed the theoretical formula for the dependence of the level of BAW excitation on COM parameters. Gamble *et al.* [60] used finite element method (FEM) to simulate bulk wave generation caused by mass loading of transducers fabricated on YZ $LiNbO_3$ substrate and reported that thick electrodes increase the electrical coupling of a uniform SAW transducer to shear vertical BAW at frequency approximately twice of the SAW center frequency. Deng [61] performed the design and fabrication of high frequency BAW transducer using IDT where the BAW is generated into interior of liquid without the need of impedance matching. Hashimoto *et al.* [62] theoretically investigated the effect of BAW radiation on the admittance of IDT in one-port SAW resonators.

Under certain circumstances the generated BAW from IDT is converted into SH-SAW by strong internal reflections and interact with BAW generated by IDT thus the net amount of BAW radiated power is highly dependent upon the number of IDT fingers. Reilly *et al.* [63] presented the generation of Rayleigh wave and BAW using IDT on YZ $LiNbO_3$. Wagner *et al.* [64] simulated using green's function and angular spectrum of waves and reported that the unintended excitation of BAW by IDT causes spurious responses in the stop bands of the SAW filters. The IDTs generate BAW in the direction $\pm\theta$ symmetrical about the normal to the surface of the piezo-substrate as shown in Figure 2.24. The constructive interference of the propagating BAW occurs for the condition given below.

$$2d\sin\theta = \lambda_B = v_B / f \tag{41}$$

where, λ_B is the BAW wavelength and v_B is the BAW velocity into the substrate, d is the width of the electrode, and λ is the wavelength of SAW. If f_0 is the synchronous or resonance frequency of SAW, then the cut off frequency of this effect can be derived from equation (41) as

$$f\frac{\sin\theta}{v_B(\theta)} = \frac{1}{2d} = \frac{f_0}{v} \qquad \Rightarrow f > \frac{v_{Bmin}}{2d} \tag{42}$$

Thus the minimal speed of the bulk wave (v_{Bmin}) is generally greater than the SAW velocity v. As mentioned in the previous section the generated BAWs interfere with the SAW and affect the performance of the device. The radiated BAW power from IDT highly depends on the number of IDT finger pairs and BAW radiation becomes small for IDTs with large number of

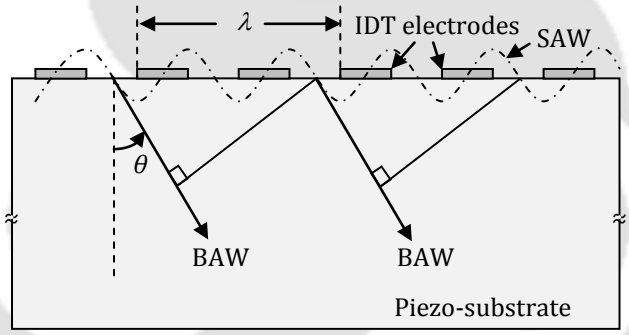

Figure 2.24 Schematic diagram of BAW radiation with an angle θ.

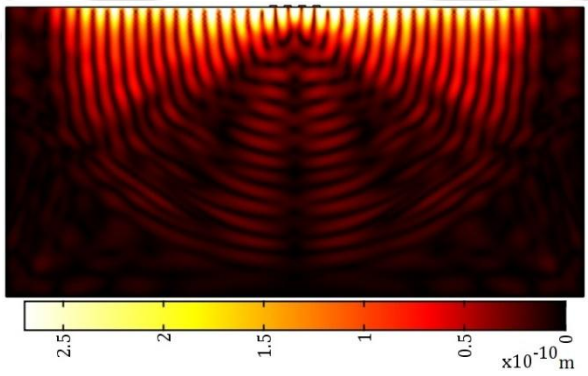

Figure 2.25 Displacement profile in SAW substrate with two pairs of IDT fingers showing BAW generation at different angles normal to the surface of piezo-substrate.

finger pairs [58]. The total power generated by IDT in the form of bulk wave can be expressed in integration form as

$$P_B = \int_{-s_n}^{s_n} \mathrm{Im}\left\{\Gamma(s)\bar{\sigma}(\omega s)\bar{\sigma}(\omega s)^* ds\right\} \quad (43)$$

where, $s = 1/v_B$ is the slowness of the bulk wave, Γ is the real function for the numerical value of s, $\bar{\sigma}$ is the free charge density at the surface, and $\pm s_n$ is the slowness of BAW along the x_1 direction [58].

A simple structure consists of two pairs of IDT fingers in the middle of piezo-substrate as YZ $LiNbO_3$ is taken to demonstrate the BAW radiation into interior of the piezo-substrate. The displacement profile in the simulated structure is shown in Figure 2.25.

The radiation angle of DBAW increases with increase in the frequency of the device [22]. In a SAW filter of 100 MHz center frequency, Hashimoto [22] reported spurious response in the range of 130–200 MHz due to DBAW and spurious response in the range of 170–200 MHz due to SSBW. Most of the DBAW can be eliminated by sanding the opposite face of the piezo-substrate or by using the absorber the bottom of the substrate, however, it does not affect SSBW. A multistrip coupler between input and output IDT is also another method to eliminate the effects of BAW radiation [4].

(a) BAW generation in conventional SAW delay line devices

The SAW delay line device with delay line of 3λ (λ= 4 μm) is simulated in 2D structure to perform the study of BAW generation by FEM using COMSOL Multiphysics as described in section 2.11. The transit time analysis is performed for time duration of 15 ns. The total displacement of the substrate is recorded at different intervals of time during the analysis. Figure 2.26 (a) to (h) show the total displacement profile of generation and propagation of SAW over the surface of the piezo-substrate and BAW into the piezo-substrate observed at time 2.50 ns, 3.10 ns, 3.45 ns, 4.09 ns, 5.21 ns, 6.38 ns, 7.57 ns, and 11.20 ns.

Considering free surface SAW phase velocity of 3477.914 m/s as calculated in section 2.8, the ideal time taken by SAW to propagate from transmitter to the receiver is 3.45 ns. The total displacement profile shown in Figure 2.26 clearly shows that BAW generates from IDT and travels inside the substrate. However the BAW attenuates as it travels along the depth of the medium. The values of total displacement amplitude observed at the first IDT finger of the

receiver IDT at times 2.50 ns is 0.901 $\times 10^{-12}$ m as extracted from Figures 2.26 (a). These displacements are purely due to transverse components of BAW as they are observed at the time before SAW reaches at the receiver IDT. Thus the addition of BAW into SAW at the receiver is noticeable. It is clearly evident from the total displacement profile shown in Figure 2.26 (c) to (h) that, as time progresses, the BAW propagates in several angles into the interior of the substrate. The BAW radiation angles, α calculated from Figure 2.26 (h) are 37°, 49°, and 70°.

An identical SAW delay line device with massless IDT electrodes (h_e = 0 μm) is simulated. The values of total displacement amplitude observed at the first IDT finger of the receiver IDT at time 2.50 ns is 0.297 $\times 10^{-12}$ m as extracted from Figure 2.27. It can be seen from Figure 2.26 (a) and Figure 2.27 that the BAW displacement in massless IDT is about 32.96 % less than the BAW displacement observed for aluminium IDT of thickness 200 nm. Hence, the mass loading of IDT increases BAW amplitude.

(b) BAW generation in conventional SAW resonator devices

In this section, simulation of a one port SAW resonator is performed to find out the BAW velocity and the effects of IDT mass loading, electrical loading, and depth of the piezo-substrate on the BAW velocity. Initially, the resonator wavelength of 16 μm with depth of 10λ is simulated. Free surface of the substrate is taken to calculate the BAW velocity. The subdomain settings, boundary setting are the same as used in section 2.8. An eigenmode analysis is performed to get different modes of BAW generation inside the piezo-substrate.

The BAW velocity is calculated from the modes of BAW obtained from the simulation. The different modes of BAW generation are shown in Figure 2.28. The BAW velocity is then calculated from the eigenmode frequency obtained for different modes and the depth of the piezo-substrate.

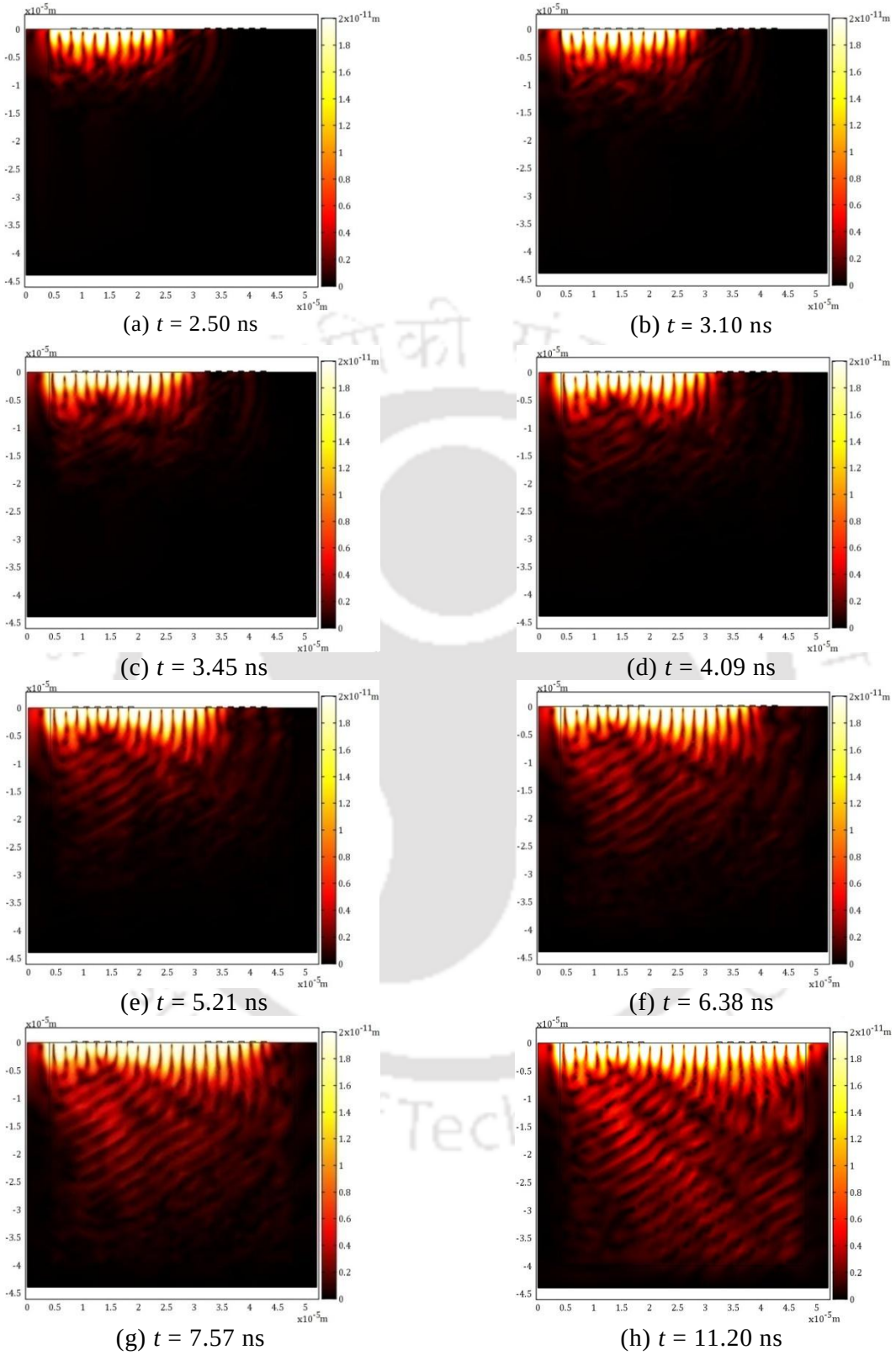

(a) t = 2.50 ns (b) t = 3.10 ns

(c) t = 3.45 ns (d) t = 4.09 ns

(e) t = 5.21 ns (f) t = 6.38 ns

(g) t = 7.57 ns (h) t = 11.20 ns

Figure 2.26 Total displacement profile of the SAW delay line device with IDT electrode thickness of 200 nm, showing propagation of SAW on the surface of the substrate BAW into the interior of the substrate observed as time progresses.

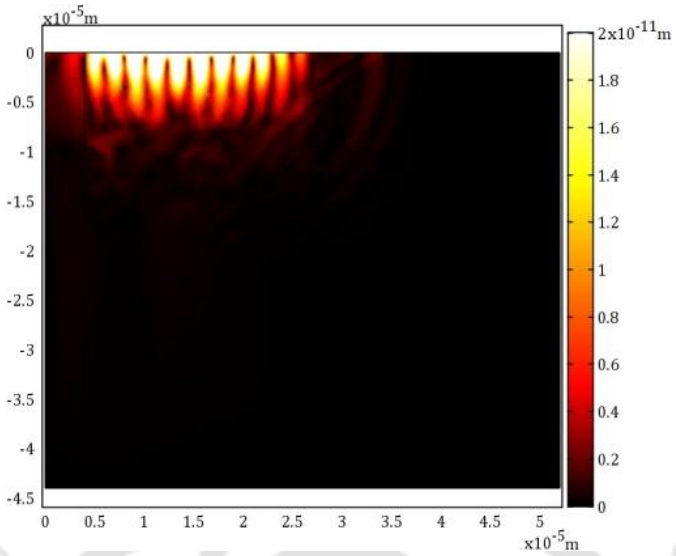

Figure 2.27 Total displacement profile of the SAW delay line device with massless IDT electrode thickness, showing propagation of SAW on the surface of the substrate BAW into the interior of the substrate observed at time 2.50 ns.

The calculated velocity at different modes of the BAW is tabulated in Table 2.4. The BAW velocity calculated from FEM based simulation for the piezo-substrate as YZ $LiNbO_3$ is 6609.395 m/s. The effects of mass loading and electrical loading on BAW velocity are demonstrated using IDT finger thickness h_e of 0.2 μm and massless IDT fingers thickness h_e of 0 μm, respectively. The eigenmode frequencies are calculated at different modes of the BAW for both configurations. The simulation is repeated for resonator of wavelength of 4 μm.

The simulation results are shown in Figure 2.29 and Figure 2.30. Figure 2.29 shows the difference of acoustic velocities between free surface velocities for various depths of the piezo-substrate. The depth of the substrate is taken as 120 μm, 160 μm, 200 μm, and 240 μm. Figure 2.30 shows the difference of acoustic velocities between free surface velocities for resonator of wavelengths of 4 μm and 16 μm with massless IDT electrodes and with IDT electrode thickness of 0.2 μm.

TABLE 2.4

BAW VELOCITIES CALCULATED FROM DIFFERENT MODES OF BAW

Modes	Depth in terms of BAW λ	SAW resonator of SAW λ =16 μm	
		Eigenmode frequency (MHz)	Velocity (m/s)
SAW	-	217.369630	3477.914
BAW I	λ/4	10.327179	6609.395
BAW II	3λ/4	30.981537	6609.395
BAW III	5λ/4	51.635895	6609.395
BAW IV	7λ/4	72.290254	6609.395
BAW V	9λ/4	92.944612	6609.395
BAW VI	11λ/4	113.598970	6609.395

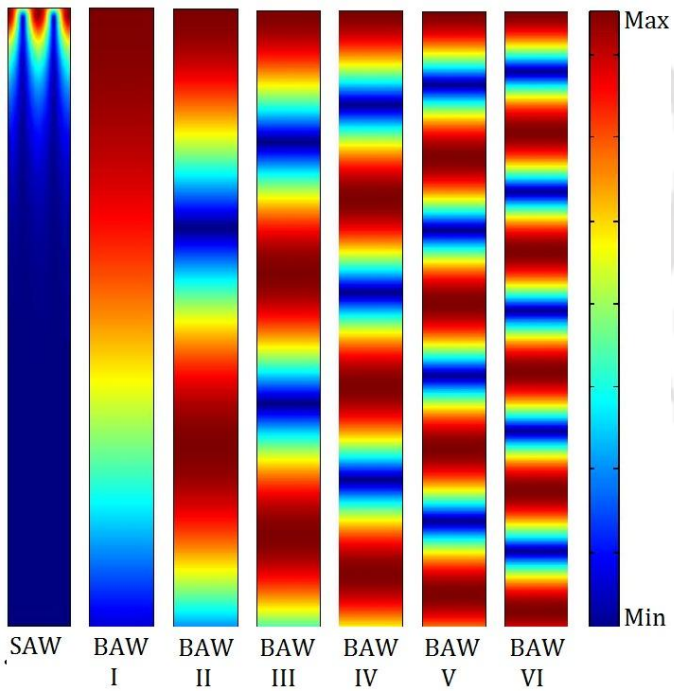

Figure 2.28 Total displacement profile of free surface piezo-substrate showing different modes of BAW.

Form Figure 2.29 it is observed that the increase in depth of the substrate results in less change in BAW velocity as the end effects are small fraction of the device depth. From Figure 2.30 it is observed that the electrical loading of the IDT electrodes has imperceptible effect on

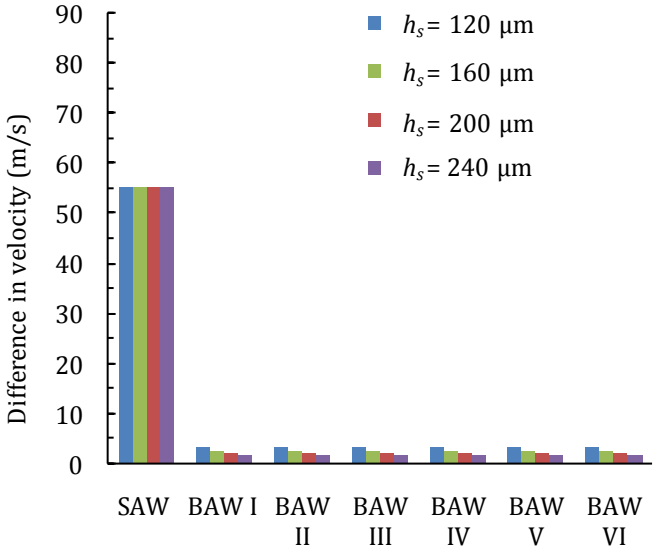

Figure 2.29 Change in acoustic velocity for SAW and various BAW modes at different depth h_s of the piezo-substrate and h_e of 0.2 µm.

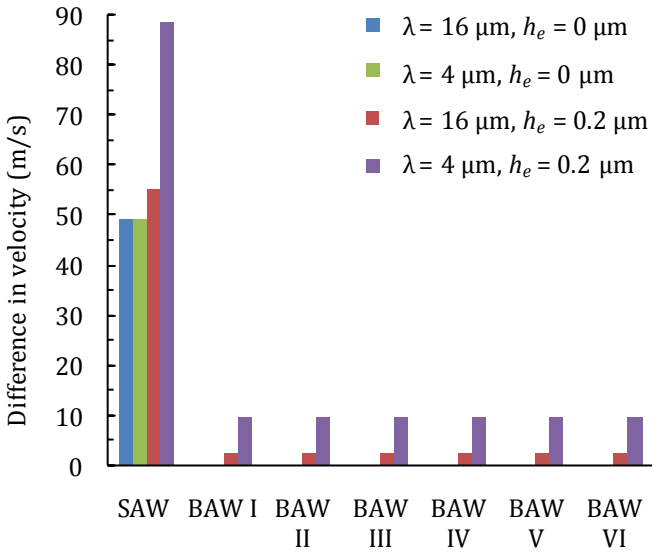

Figure 2.30 Change in acoustic velocity for SAW and various BAW modes for substrate depth of 160 µm.

the BAW velocity. The BAW velocity is more affected by the mass load of IDT. Also, the BAW velocity is more affected in the high frequency device (see Figure 2.30). In conclusion the effects of BAW on SAW devices are more predominant in high frequency devices and for thinner piezo-substrates.

2.13 Summary

This chapter discusses a brief introduction to various modeling techniques such as delta function method or discrete source method, impulse response method, piezoelectric permittivity method, equivalent circuit method, COM model, and numerical simulation methods like FEM. The piezoelectricity, equation of motion, and solution to surface waves in piezoelectric media are presented.

Simulations are performed based on FEM using COMSOL Multiphysics to determine the free surface SAW phase velocity and adequate mesh density for the simulation. Simulation of one port SAW resonator is carried out so that the results will be used to compare the proposed SAW device configuration. Various device parameters such as quality factor and capacitance ratio are calculated. The effect of aperture of SAW resonator on resonance frequency and harmonic admittance is examined. It is shown that a small aperture length is sufficient to model a SAW resonator to study the resonance frequency, harmonic admittance and other parameters of the resonator.

Simulation of SAW delay line is performed to find out the delay time and attenuation in the output electric potential. The secondary effects caused by the presence of metallic IDT over the surface of the piezo-substrate are demonstrated by simulation in COMSOL Multiphysics. The effects of mass loading and electrical loading are studied. The device parameters such as velocity dispersion, reflection coefficient, and effective permittivity as a function of metallization ratio are presented.

Further, BAW generation inside the piezo-substrate in conventional SAW delay line and resonator devices is shown and the BAW velocity and displacements are determined. It is observed that the electrical loading of the IDT electrodes has negligible effect on the BAW velocity. The BAW velocity and amplitude are more affected by the mass load of IDT.

3

SAW Devices with Non-contact IDT

Chapter 2 has presented the theory of piezoelectricity, generation of surface acoustic wave (SAW), modeling of SAW devices, and simulation of one port SAW resonator and SAW delay line device. In addition, the secondary effects caused by the presence of metallic IDT in conventional SAW devices have been investigated and their effects on the characteristics of the SAW devices have been discussed.

In this thesis, we propose two types of SAW devices: 1. SAW devices with non-contact interdigital transducer (NCIDT) and 2. SAW devices with electric field coupled bond pads. The first proposed SAW device comprises of plain piezo-substrate and NCIDT patterned on a non-piezoelectric substrate. The NCDIT is kept facing the piezo-substrate with uniform air gap much smaller than the SAW wavelength. The second SAW device comprises of IDTs fabricated on the piezo-substrate, and external metal plates placed over the bond pads with or without air gap. The pictorial representation of one periodic section of conventional SAW device, proposed SAW device with NCIDT, and proposed SAW device with electric field coupled bond pads is shown in Figures 3.1 (a), (b) and (c), respectively.

SAW devices with electric field coupled bond pads are presented in chapter 4, and SAW devices with the NCIDT are studied in this chapter. COMSOL Multiphysics is used to simulate

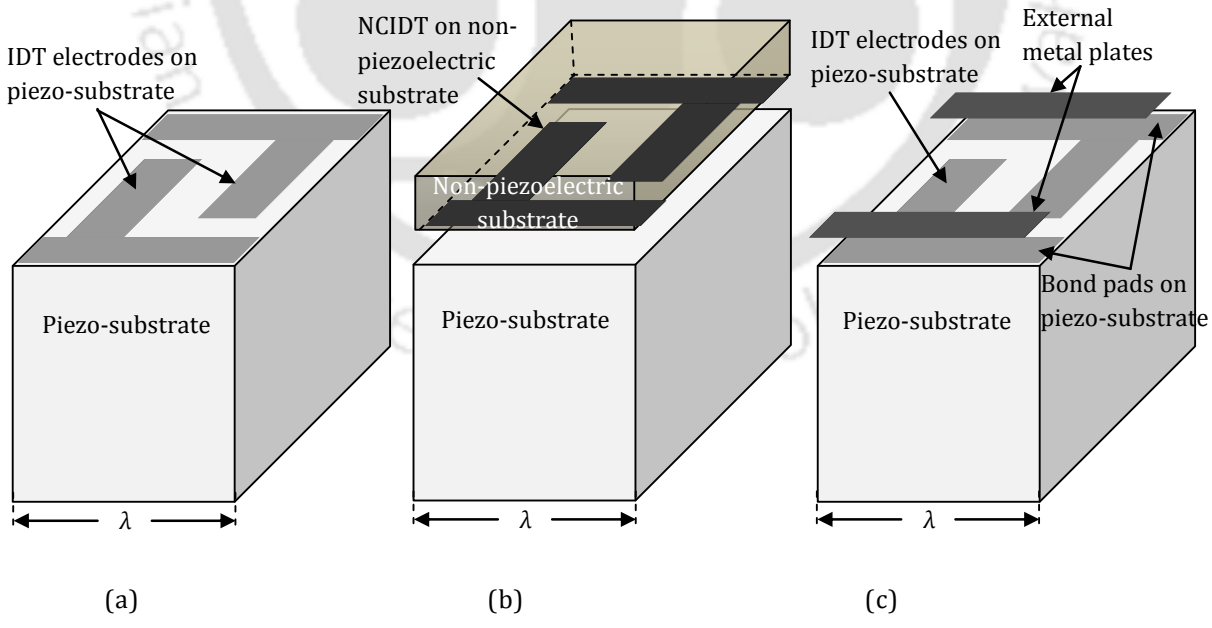

Figure 3.1 Pictorial representation of one period of (a) conventional SAW device, (b) proposed SAW device with NCIDT, (c) proposed SAW device with electric field coupled bond pads.

the SAW devices and the results of simulation are compared with the results for identical conventional SAW devices presented in chapter 2. One port SAW resonator and delay line SAW devices using NCIDT have been simulated. The effects of variations in air gap and tilt in NCIDT plane are studied. The advantages of proposed SAW devices over conventional SAW devices are discussed. Simulations of sensors using the proposed and conventional SAW devices are performed and their sensitivities are compared.

3.1 SAW devices with NCIDT – Theory and operation

In the conventional SAW devices IDTs are fabricated on the surface of the piezo-substrate and are used to convert electrical energy into mechanical energy and vice versa. The IDTs over the piezo-substrate generate SAW by application of electrical signal due to reverse piezoelectric effect and generate electrical potential from SAW by direct piezoelectric effect [4] [20]. However, there exist secondary effects such as reemission, bulk wave generation, diffraction, phase speed variations, reflections, and electromagnetic coupling. The resistive loss occurs at high frequency due to small size of IDT fingers. The presence of metallic electrodes on the surface causes changes in electrical and mechanical impedances at the surface and introduces dispersion of the wave. As discussed in chapter 2, the main cause of these secondary effects in the conventional SAW devices is the presence of metallic IDTs over the piezo-substrate. The mass loading and electrical loading effects of the IDT electrodes in contact with the piezo-substrate are the major reasons of most of the secondary effects. These effects can be overcome by separating IDTs from the piezo-substrate by a small air gap and coupling electric field through the air gap. Ingebrigtsen [20] reported that in order to transmit mechanical force to the piezo-substrate a direct contact in necessary while electrical forces can be transmitted to the substrate from outside the substrate within a wavelength distance.

In the proposed SAW devices NCIDT is fabricated on a non-piezoelectric substrate and kept facing the piezo-substrate with air gap smaller than the SAW wavelength. It does not require any fabrication process on the piezo-substrate. The RF signal applied to the NCIDT electrodes generates electric field that passes through air and couples to the piezo-substrate. The electric field coupled by the periodic IDT structure generates constructive deformation on the device substrate by inverse piezoelectric effect [20]. The NCIDT is used to pick up electric potential from SAW generated on the piezo-substrate by direct piezoelectric effect. The

suggestion of making separate IDT on glass or silicon substrate permanently bonded with piezo-substrate was given several years ago in a patent by Eda *et al.* [21], but the devices have not been discussed or analyzed in any published research literature. We have analyzed SAW devices with NCIDT by carrying out rigorous simulations and experiments, and concluded that the proposed configuration has potential applications in the field of signal processing and communication, where frequency accuracy is crucial. Other applications include high sensitivity SAW sensors as the entire piezo-substrate is available for sensing and convenient operation as bonding wires are eliminated. Not much published literature is found related to the proposed device configuration. However the electric field coupling between a piezoelectric half-space and a plane at a height is reported by the following authors. Morgan [3] discussed the application of effective permittivity and the coupling between a piezoelectric half-space and a plane at a height. Coupling decreases exponentially with increase in the air gap, thus the gap has to be a small fraction of wavelength for the concept to be practically effective. Kino [17] presented types of acoustoelectric amplifier and convolver using coupling of field through air gap. The coupling of electric field to piezoelectric substrate using normal mode theory and perturbation theory is well-explained in [13] [18]. Lakin [13] reported an approximate expression for the perturbation in propagation wavenumber of SAW in piezoelectric crystal where the source of perturbation is a surface separated from the piezoelectric crystal with an air gap. The resultant perturbation is expressed in terms of perturbing electrical impedance, an effective dielectric constant for the piezoelectric, the air gap spacing, and a perturbation coupling constant. Ingebrigtsen [20] reported that the small air gap between piezo-substrate and adjoining medium may drastically reduce the coupling. Thus the air gap between piezo-substrate and adjoining medium must be very small compared to the wavelength. Auld *et al.* [65] presented the normal mode expansion for the analysis of acoustic waves based on orthogonality relations between the modes of acoustic waves and can be used to relate the perturbation and propagation constants of a particular mode to the properties of the modes of the unperturbed system and modes of the perturbation. Kino *et al.* [66] presented the normal mode theory for Rayleigh wave amplifier in which the wave travelling over the piezo-substrate is amplified by interaction with the drift carriers in an adjacent semiconductor placed above to the piezo-substrate with a small air gap.

The simulation of the proposed SAW devices with NCIDT by FEM using COMSOL Multiphysics is described below. In addition, the following sections include the comparison of the results of

simulations with that of conventional SAW devices, various aspects of construction of NCIDT SAW devices, secondary effects, and application to gas sensors.

3.2 Simulation of one port SAW resonator with NCIDT based on FEM in 2D

A one port SAW resonator can be designed by using a large number of IDT finger-pairs where multiple reflections occur between the fingers or by using reflectors either side of a short IDT having less number of fingers as explained in chapter 1, section 1.3, [6], [22]. The simulations of conventional SAW resonator by FEM are described in chapter 2, section 2.9. This section of the chapter presents simulation of the proposed one port SAW resonator with NCIDT in 2D by FEM using COMSOL Multiphysics. The simulation results of the resonator with NCIDT are compared with the simulation results of an identical conventional SAW resonator.

3.2.1 Structure of one port SAW resonator with NCIDT

As discussed in chapter 2, the presence of metallic IDT over the piezo-substrate gives mass loading and electrical loading which produce several secondary effects in the device and perturb the SAW velocity. Therefore in the proposed configuration of SAW devices, the IDT is separated from the piezo-substrate and it is called as non-contact IDT (NCIDT). The NCIDT is fabricated on a non-piezoelectric substrate and kept above facing to the piezo-substrate with a uniform air gap. The electric field generated from the NCIDT couples to the piezo-substrate through the air gap and generates SAW on the piezo-substrate and vice versa.

The proposed one port SAW resonator with infinite number of IDT fingers fabricated on a non-piezoelectric substrate is considered in the simulation. Owing to the periodic nature of NCIDT structure, one pair of NCIDT finger is used to model the proposed one port SAW resonator and periodic boundary conditions are applied. The 2D geometry structure of one port SAW resonator with NCIDT is shown in Figure 3.2.

3.2.2 Simulation methodology

A one port SAW resonator with NCIDT patterned on single crystal silicon (Si) wafer having infinite number of IDT fingers is considered for FEM simulation. Owing to periodic nature of IDT structure, a one pair of IDT electrodes is used to model the NCIDT SAW resonator as used

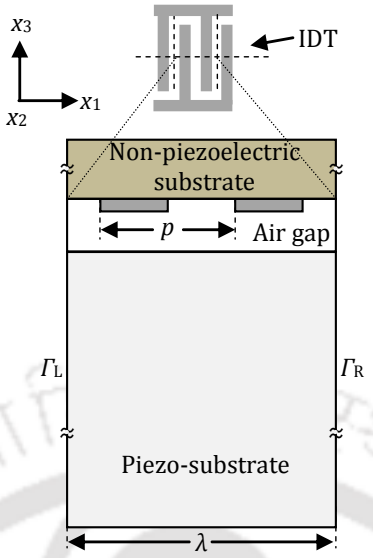

Figure 3.2 2D geometry of one port SAW resonator with NCIDT used in simulation.

in Chapter 2, Section 2.9, and periodic boundary conditions are applied. The simulation is carried out by FEM using piezo plain strain application mode provided in COMSOL Multiphysics [13]. The 2D geometry of a periodic segment of the NCIDT SAW resonator considered in the simulation is shown in Figure 3.2. The dimensions used in the simulation are as follows: NCIDT finger width (d) 4 μm, electrode pitch (p) 8 μm, depth of the piezo-substrate (h_s) 160 μm (10 λ) in $-x_3$ direction, thickness of IDT fingers (h_e) 0.2 μm, holding substrate thickness (h_h) truncated to 16 μm in x_3 direction. The thickness of holding substrate is found to be adequate in a simulation described in section 3.5. The YZ $LiNbO_3$ piezoelectric material is used as the piezo-substrate. The values of elastic constants, permittivity constants, stress constants, and density are given in Appendix C. Silicon (Si) substrate is used as the holding substrate for the NCIDT. The NCIDT is placed parallel over the piezo-substrate with air gap (h_a) of 4 μm which is practical [17]. The bottom surface of the piezo-substrate is kept fixed and all other boundaries are stress-free. Periodic boundary conditions are set in x_1 direction. The boundary conditions of the right boundary (Γ_R) are set equal to those of the left boundary (Γ_L) (see Figure 3.2). In general, the expression for periodic boundary conditions for one port SAW resonator model is given in equation (32).

An alternating voltage of 1 V is applied to the NCIDT fingers. An extremely fine mesh with minimum element quality of 0.7 and the number of mesh elements of 32 per wavelength are adopted for the 2D simulation. The number of degrees of freedom solved is in the order of 2 ×

10^5. The harmonic analysis is performed to find the characteristics and parameters of the resonator.

3.2.2 Results and discussions

The results of simulation of the proposed NCIDT SAW resonator are shown in Figures 3.3 and 3.4. The total displacement profile, *x*-displacement profile and *y*-displacement profile of the NCIDT SAW resonator at resonance frequency of 217.3633 MHz are shown in Figures 3.3 (a), (b) and (c), respectively. Since the displacement profile at the top surface is dominant, the displacement profile in Figure 3.3 is shown up to a depth of about 4λ in the piezo-substrate and the part of the holding substrate 0.16λ thick is shown.

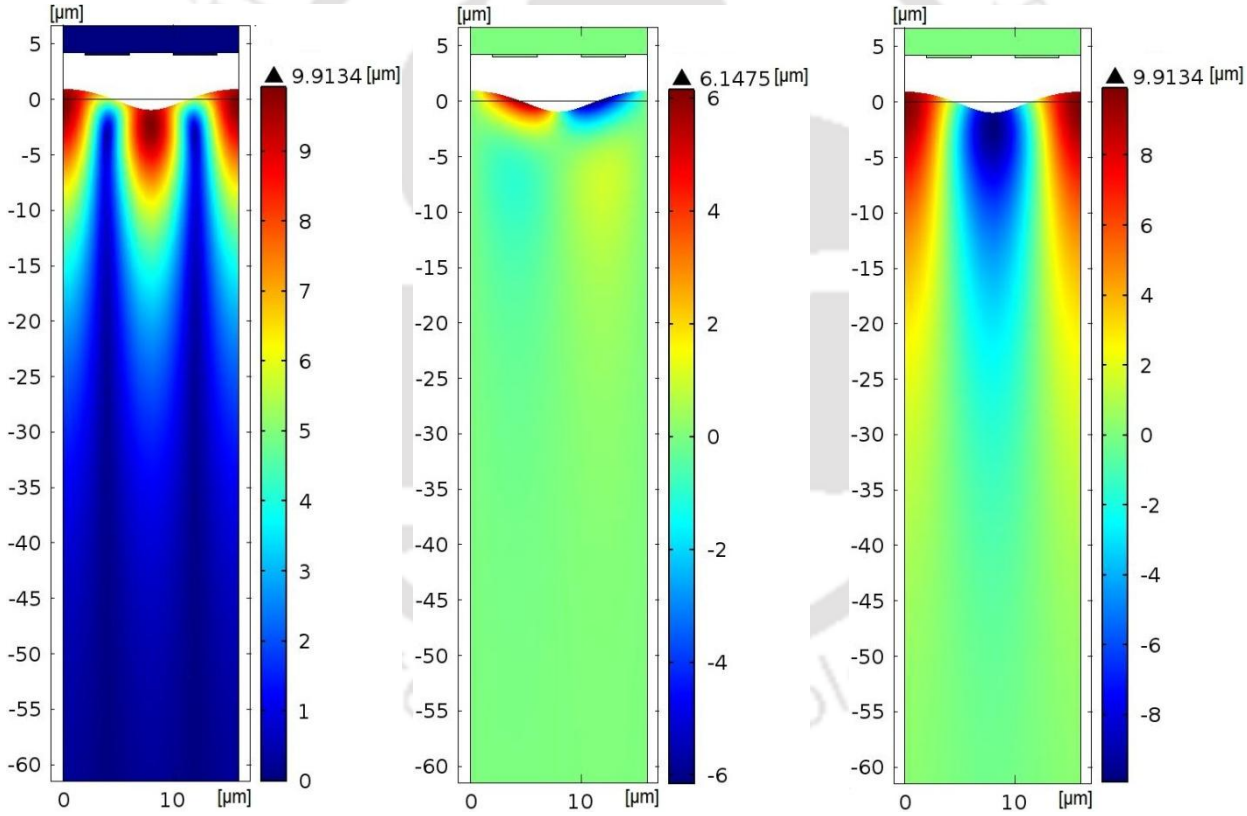

Figure 3.3 Displacement profile of the one port resonator at resonance frequency 217.3633 MHz with deformed shape. (a) Total displacement profile, (b) x-displacement profile and, (c) *y*-displacement profile. Note: To give emphasis to the top surface, the displacement profile in the figure is shown up to the substrate depth of about 4λ.

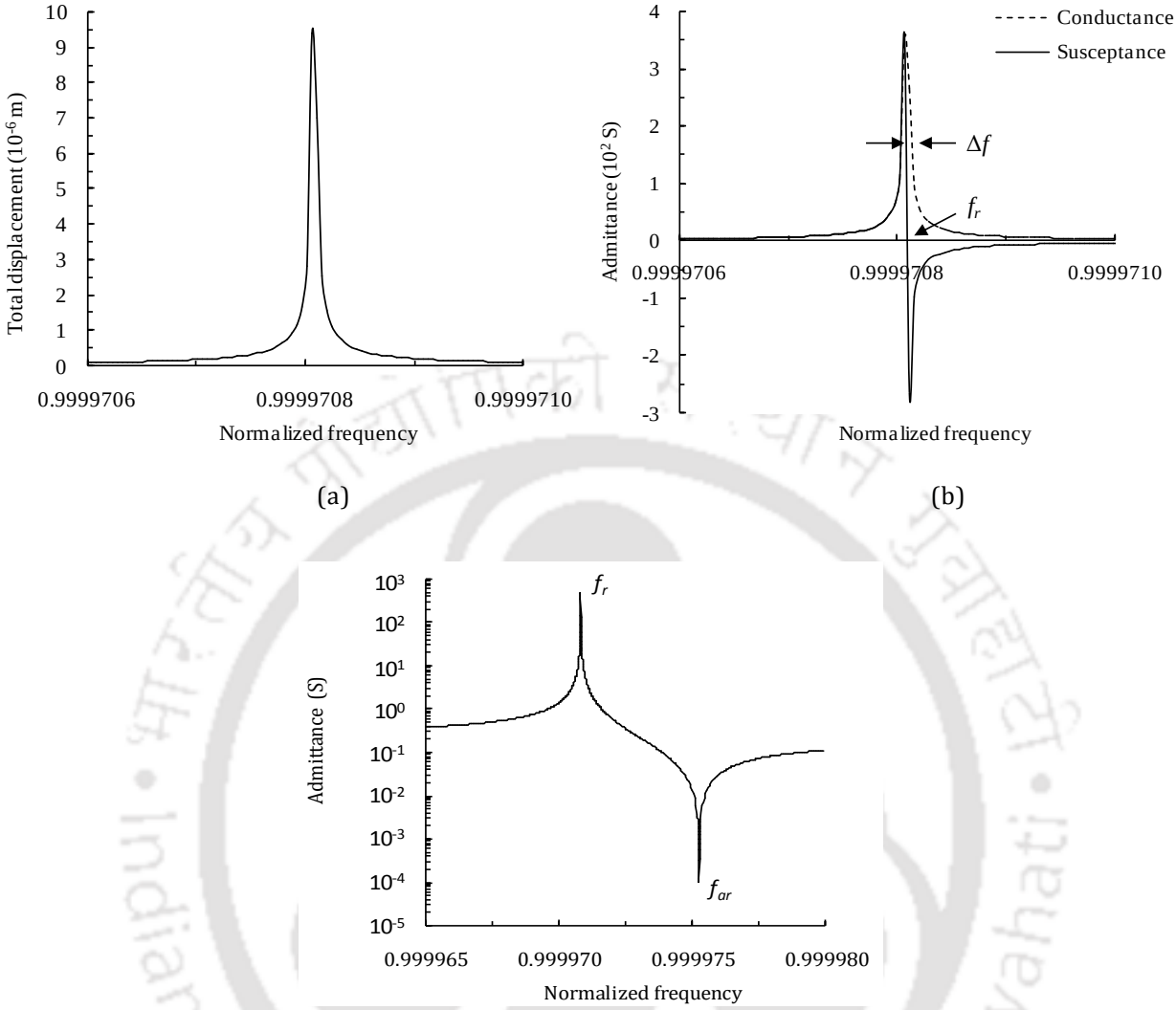

Figure 3.4 Results of simulation of the one port resonator. (a) Plot of total displacement versus normalized frequency, (b) plot of harmonic admittance versus normalized frequency, and (c) plot of magnitude of harmonic admittance versus normalized frequency.

Figure 3.3 shows that the displacement in the piezo-substrate diminishes below 1λ depth of the piezo-substrate, which depicts the nature of Rayleigh SAW. The plot of total displacement as a function of normalized frequency in Figure 3.4 (a) shows peak at the resonance frequency. The normalized frequency is expressed as $\eta = 2pf/v_0$ [48], where, v_0 = 3477.914 m/s, is the free surface velocity of the substrate as calculated in section 2.8. The curves of harmonic admittance per period as a function of normalized frequency for the NCIDT SAW resonator are shown in Figures 3.4 (b) and (c). The harmonic admittance per period of NCIDT

SAW resonator is measured at NCIDT electrodes [15]. Figure 3.4 (b) shows conductance and susceptance plots around the resonance frequency. The resonance frequency of the resonator is identified as the frequency at which the susceptance plot crosses zero value. Figure 3.4 (c) shows the plot of harmonic admittance per period on logarithmic scale covering both the resonance and antiresonance frequencies. The value of harmonic admittance is about 10^2 S at resonance frequency. In real devices, it would be lower due to attenuation, damping and finite aperture. This simulation does not consider attenuation and damping, and assumes infinite aperture in x_2 direction.

The simulation results of NCDIT SAW resonator and of conventional SAW resonator are compared. Simulations of conventional SAW devices are presented in chapter 2. Table 3.1 shows comparison of resonance frequency, total displacement and admittance for the NCIDT SAW resonator and an identical conventional SAW resonator. The resonance frequency f_0 of an identical device with free surface is calculated from the eigenmode analysis of the piezo-substrate of equal dimensions and is found to be 217.3696 MHz. With reference to free surface resonance frequency f_0, the resonance frequency of the conventional SAW resonator is 4.4895 MHz lower, whereas the resonance frequency of the NCIDT SAW resonator is remarkably close, 6.34 kHz lower. The slight deviation in resonance frequency of NCIDT resonator is mostly the effect of permittivity of the holding substrate [3]. The effects of holding substrate on the resonance frequency and SAW phase velocity are discussed in section 3.5. From Table 3.1 it is observed that the total displacement of the NCIDT SAW resonator is about 2 orders lower than the conventional SAW resonator. The value of harmonic admittance at resonance in the NCIDT SAW resonator is about 4 orders lower than

TABLE 3.1
COMPARISON OF PARAMETERS OF NCDIT SAW RESONATOR AND CONVENTIONAL SAW RESONATOR

	Resonance frequency	Magnitude of total displacement	Admittance
Proposed SAW resonator with NCIDT	217.3633 MHz	9.4 µm	503.6 S
Conventional SAW resonator	212.8801 MHz	2822.3 µm	18296913.7 S

The resonance frequency of identical device with free surface calculated from eigenmode analysis is 217.3696 MHz.

the conventional SAW resonator. However, the resonance frequency of the NCIDT SAW resonator is remarkably close to the resonance frequency with free surface. Hence the NCIDT SAW devices have applications in the field of signal processing and communication where frequency accuracy is crucial.

The effectiveness of SAW excitation is characterized by the transaction coefficient per period α_p given as [48]

$$\alpha_p^2 = \frac{1}{4} G_r \gamma_p \tag{44}$$

where, G_r is the conductance at resonance frequency and γ_p is the attenuation per period [17] [19]. To compare the NCIDT and conventional structures, the ratio of the corresponding transaction coefficients can be roughly estimated from the ratio of the corresponding conductance peaks. From Figure 2.16 (b) and Figure 3.4 (b), the ratio of the corresponding conductance peaks shows that the excitation efficiency in NCIDT resonator is about 4 orders lower than conventional resonator. To overcome the reduction in the excitation efficiency, the NCIDT SAW device needs to be operated with adequately high gain amplifier and often high voltage excitation.

The quality factor Q_r at resonance frequency f_r of the NCIDT SAW resonators is calculated using equation (34). The quality factor of the NCIDT SAW resonator is compared with the conventional SAW resonator. As calculated from Figure 3.4 (b) and Figure 2.16 (b) it is found that the quality factor of the NCIDT SAW resonator is 97254269 about 40 % less than the quality factor of the conventional SAW resonator.

The capacitance ratio which is a measure of the resonator performance is calculated from Figure 3.4 (c). The expression for capacitance ratio is given in equation (35). The capacitance ratio for the NCIDT SAW resonator is 112390 which is about 4000 times the capacitance ratio of the conventional SAW resonator.

3.3 Simulation of one port SAW resonator with NCIDT based on FEM in 3D

The simulation of NCIDT one port SAW resonator in 2D with infinite aperture is discussed in the previous section. In this section NCIDT one port SAW resonator with finite aperture is simulated with simplified model in 3D. The values of admittance and transduction coefficient of the NCIDT SAW resonator are compared with the conventional SAW resonator.

For 3D simulation, piezo-solid application mode provided in COMSOL Multiphysics is used. A section of the device with one pair of IDT electrodes is used with periodic boundary conditions in the simulation. The dimensions of the device are the same as that used for the conventional device described in section 2.10. The dimensions used for the 3D simulation are as follows: NCIDT finger width (d) 4 μm, electrode pitch (p) 8 μm, electrode finger thickness (h_e) 0.2 μm, holding substrate of silicon with thickness (h_h) truncated to 8 μm in x_3 direction, depth of the piezo-substrate truncated to 5λ in $-x_3$ direction, and aperture in x_2 direction (aperture) varied from 2 μm to 8 μm. The NCIDT is placed parallel over the piezo-substrate with air gap of 4 μm which is practical [17]. The depth of piezo-substrate is truncated to 5λ since SAW energy is concentrated near the substrate depth of one wavelength and the number of nodes to be solved is realizable. The thickness of holding substrate is found to be adequate from the simulation results given in section 3.5. YZ $LiNbO_3$ piezoelectric material is used for the piezo-substrate. The values of elastic constants, permittivity constants, stress constants, and density for the substrate used in the simulation are given in the Appendix C. The bottom surface is fixed and zero displacement constraint is applied in x_2 direction normal to the direction of wave propagation which is valid in the case of Rayleigh SAW. The periodic boundary condition is applied to left (Γ_L) and right (Γ_R) sides of device substrate. The eigenmode analysis is performed to compute the resonance frequency of the NCIDT SAW resonator. Table 3.2 shows the resonance frequency and antiresonance frequency of NCIDT SAW resonator with various values of aperture W.

TABLE 3.2
VARIATIONS IN RESONANCE AND ANTIRESONANCE FREQUENCIES WITH CHANGE IN APERTURE (W) FOR NCIDT SAW RESONATOR

Aperture, W (μm)	Resonance Frequency (MHz)	Antiresonance Frequency (MHz)
2	216.997	217.001
3	216.980	216.981
4	216.913	216.958
6	216.949	216.945
8	216.923	216.907

The resonance frequency is identified from the list of eigenmode frequencies and their displacement amplitude, the mode of vibration and the charge distribution on the IDT fingers. At the resonance frequency the displacement is maximum at the middle of the space between two IDTs, while for the antiresonance frequency the displacement is maximum at the middle of the fingers as discussed in section 2.8. The charge distribution is symmetric and antisymmetric at resonance and antiresonance frequencies, respectively.

The harmonic analysis of 3D model of NCIDT SAW resonator is performed for various values of aperture width. Figures 3.5 (a), (b) and (c) show the total displacement profile, x-displacement profile, and y-displacement profile of the NCIDT SAW resonator at resonance frequency, respectively. The plot of harmonic admittance as a function of normalized frequency for aperture width of 4 μm and 6 μm is shown in Figure 3.6. The harmonic admittance value at resonance calculated for this model is in order of 10^{-6} S. It is observed that the admittance value for given aperture is proportional to the aperture. However, to study the resonance frequency, harmonic admittance and other parameters of the resonator suitably small aperture length is sufficient to model the NCIDT SAW resonator. By this way one can minimize the computational cost as mentioned in the section 2.7. The simulations of 3D model of NCIDT and conventional SAW resonator are performed with frequency resolution of 1 kHz which is sufficient and manageable in the available computing resources. The results of simulation of NCIDT SAW resonator are compared with the simulation results

for an identical conventional SAW resonator given in Chapter 2, Section 2.10. The Table of comparison for NCDIT SAW resonator and conventional SAW resonator showing resonance frequency and admittance for the aperture of 4 μm is shown in Table 3.3.

The free surface resonance frequency f_0 calculated from the eigenmode analysis of the piezo-substrate is 217.0645 MHz. With reference to free surface resonance frequency f_0, the resonance frequency of the conventional SAW resonator is 4.9464 MHz lower, whereas the resonance frequency of NCIDT SAW resonator is remarkably close, 104.5 kHz lower.

The slight deviation in resonance frequency of NCIDT resonator is mostly the effect of permittivity of the holding substrate [19] [67]. From Table 3.3 it is observed that the value of harmonic admittance at resonance for the NCIDT SAW resonator is about 4 orders lower than the conventional SAW resonator.

TABLE 3.3
COMPARISON OF PARAMETERS OF NCDIT SAW RESONATOR AND IDENTICAL CONVENTIONAL SAW RESONATOR USING 3D MODEL FOR APERTURE OF 4 μm

	Resonance frequency	Admittance
Proposed SAW resonator with NCIDT	216.960 MHz	3.5 μS
Conventional SAW resonator	212.119 MHz	30000 μS
The resonance frequency of an identical device with free surface calculated from eigenmode analysis is 217.3696 MHz.		

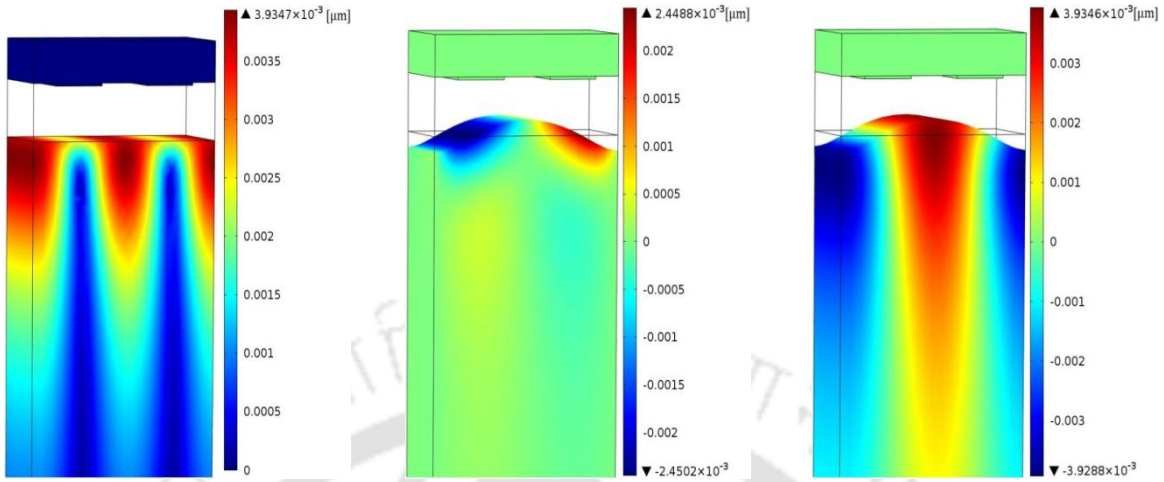

(a) (b) (c)

Figure 3.5 Displacement profiles at resonance frequency 216.960 MHz (a) Total displacement profile. (b) *x*-displacement profile with deformed shape. (c) *y*-displacement profile with deformed shape. Note: For simplicity the substrate depth of around 1 λ and holding substrate height of around 0.14 λ are shown in Figure.

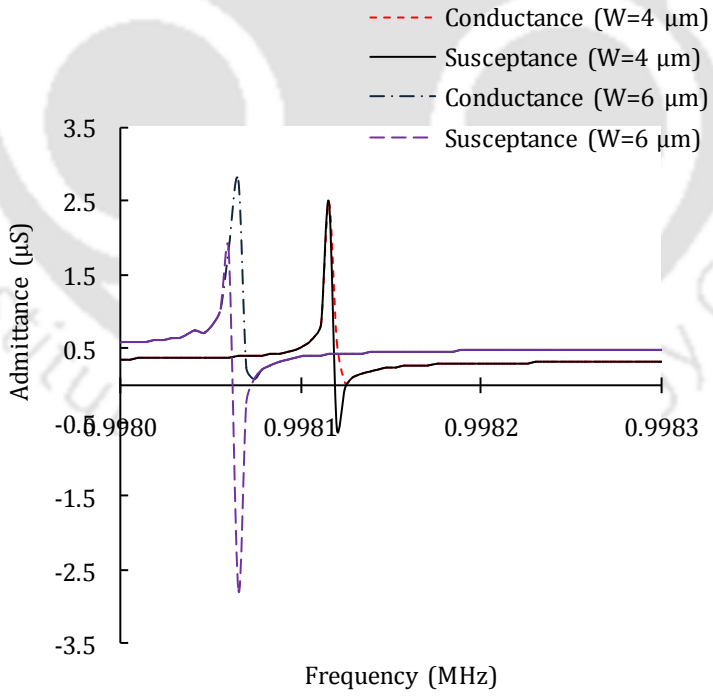

Figure 3.6. Harmonic admittance as a function of normalized frequency for various values of *W*.

3.4 Simulation of a SAW delay line device with NCIDT

In this section, an NCIDT SAW delay line device is simulated by FEM using COMSOL Multiphysics. The simulation results for the NCIDT SAW delay line device are compared with the simulation results of the conventional SAW delay line device.

3.4.1. Simulation methodology

The NCIDT SAW delay line device with delay line of 3λ for λ = 4 μm is simulated by FEM using COMSOL Multiphysics. In this simulation, three pairs of IDT fingers in transmitter IDT and receiver IDT are considered. The dimensions used for simulation are as follows: NCIDT finger width (d) 1 μm, electrode pitch (p) 2 μm, depth of the piezo-substrate 10λ in $-x_3$ direction, thickness of electrode finger (h_e) 0.2 μm, holding substrate thickness (h_h) truncated to 7 μm in x_3 direction. The NCIDT is placed above parallel to the piezo-substrate with a uniform air gap of 1 μm. 2D geometry used for simulation is shown in Figure 3.7. YZ $LiNbO_3$ material is used for piezo-substrate, Al metal is used for IDT electrodes, and glass substrate is used for holding the NCIDT. The values of elastic constants, permittivity constants, stress constants, and density used for simulation are the same as employed in Chapter 2 and are listed in Appendix C. The following boundary conditions are applied to the model. The top surface of the substrate is assumed as stress free, the bottom surface is fixed in its position. The critical damping is assumed at the edge of the transmitter B_L, receiver B_R, and bottom B_B of the device substrate as shown in Figure 3.7 to avoid reflections of the acoustic waves. The equations for critical damping are provided in Appendix D. The alternate fingers are short-circuited and 1 V sinusoidal driven voltage at the resonance frequency is applied to the transmitter NCIDT

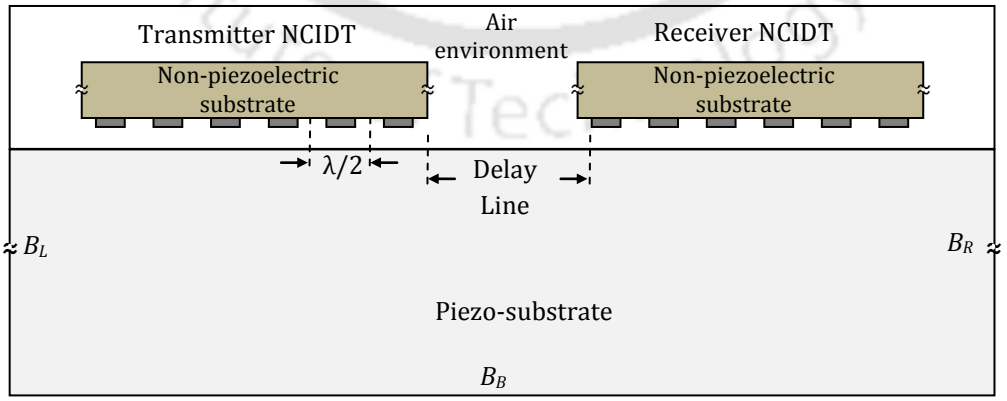

Figure 3.7 2D model of the SAW delay line device used in the simulation.

electrodes. The resonance frequency of the NCIDT SAW delay line is 870 MHz. An optimized mesh density is used for the simulation. To analyze the propagation of SAW over the delay line, transient analysis is performed using direct solver SPOOLES available in COMSOL Multiphysics [15] for 15 ns with a time interval of 0.1 ns, and the displacements and potential at the receiver electrode are recorded.

3.4.2. Results and discussions

The transient analysis of NCIDT SAW delay line is performed for time duration of 15 ns for a sine wave burst input of 1 V amplitude. Figure 3.8 (a) shows the total displacement profile in the SAW delay line at time 10 ns from the instant of application of the input. The output potential, *x* displacement, and *y* displacement at the receiver as a function time are shown in Figures 3.8 (b), (c), and (d). The output potential of around 0.4 mV peak is obtained at the receiver NCIDT electrodes at the end of 10 ns. In SAW delay line device, delay time is one of the important parameters. The instant of signal arrival at the receiver is estimated from the envelope of the waveform and the delay time is about 3.50 ns. The delay time calculated from the free surface velocity of 3478 m/s is 3.45 ns. The peak amplitudes of *x* displacement and *y* displacement at around 10 ns are approximately 3×10^{-13} m and 5×10^{-13} m, respectively.

The simulation results of NCIDT SAW delay line are compared with the simulation results of conventional SAW delay line device. The simulation of an identical conventional SAW delay line was performed in section 2.11. The comparison of the simulation results of NCIDT SAW delay line and conventional SAW delay line is given in Table 3.4. The table shows approximate values of delay time, output electric potential, x displacement, and y displacement at about 10 ns. From Table 3.4, it can be observed that the output electric potential of NCIDT SAW delay line is about 3 orders lower than the conventional delay line device. The x displacement and y displacement of NCIDT SAW delay line are 2 orders lower than the conventional delay line device. However, the delay times of the conventional and the NCIDT SAW delay line devices are close to the delay time calculated from the free surface velocity.

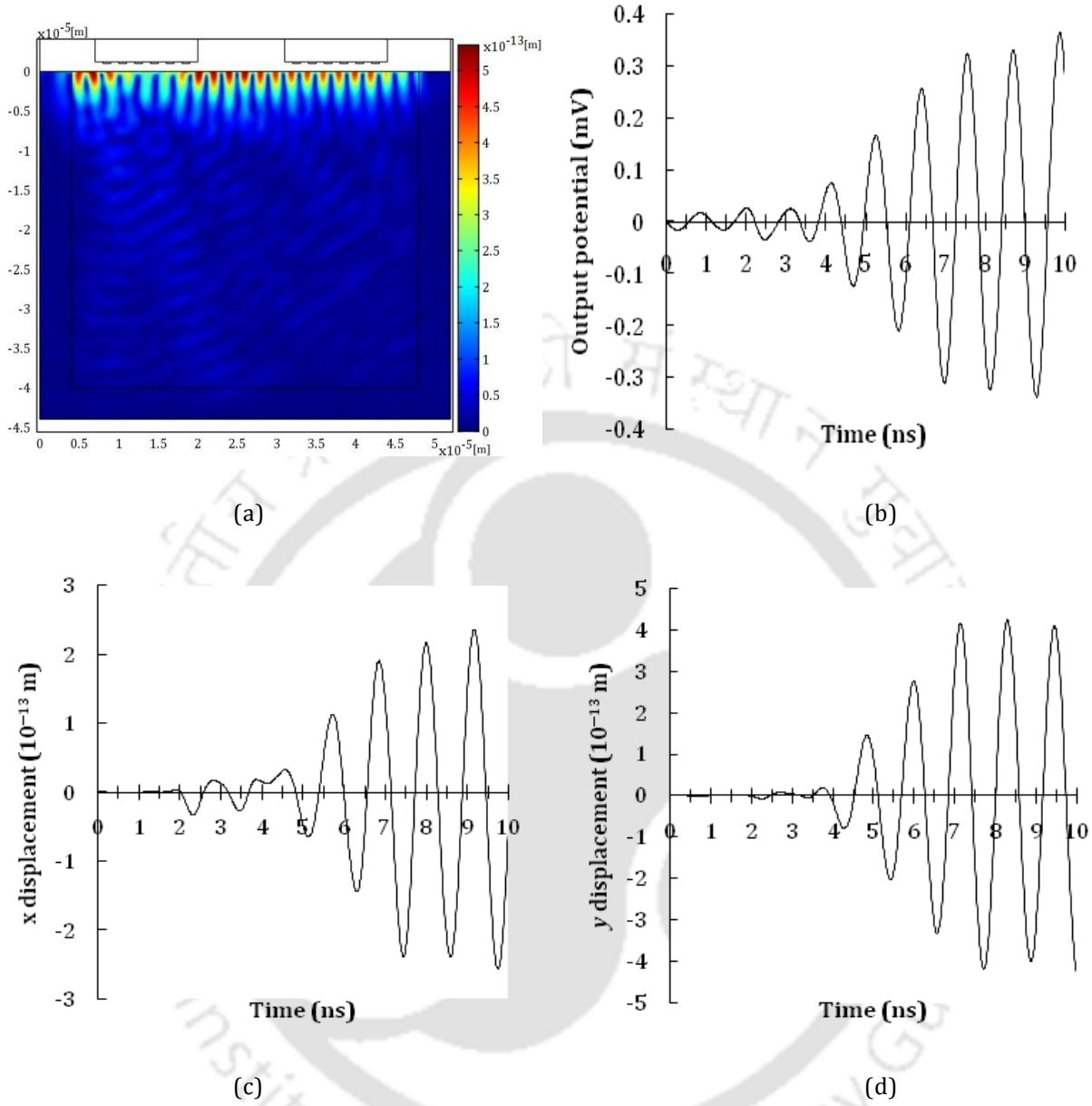

Figure 3.8 Results of simulation of NCIDT SAW delay line. (a) Total displacement profile of NCIDT SAW delay line at time 10 ns. (b) Output potential, (c) *x* displacement and (d) *y* displacement at the receiver electrode as a function of time.

TABLE 3.4
COMPARISON OF NCDIT SAW DELAY LINE AND CONVENTIONAL SAW DELAY LINE

	Delay time	Output electric potential	*x* displacement	*y* displacement
Proposed NCIDT SAW delay line	3.5 ns	0.4 mV	3×10^{-13} m	5×10^{-13} m
Conventional SAW delay line	3.5 ns	300 mV	3×10^{-11} m	5×10^{-11} m

Note: The electric potential and displacement values are the peak values of the waveforms at about 10 ns. The delay time calculated using the free surface velocity of 3478 m/s is 3.45 ns.

3.5 Different aspects of NCIDT SAW devices

In the proposed NCIDT SAW devices, the IDTs are separated from the piezo-substrate, are fabricated on a non-piezoelectric substrate and kept facing the piezo-substrate with an air gap. The proposed device configuration eliminates mass loading effects in the device due to the absence of the IDTs on the device substrate and reduces electrical loading due to the air gap.

Since the proposed devices employ a holding substrate for NCIDT and have air gap between NCIDT and piezo-substrate, the following aspects are investigated: Effect of thickness of the holding substrate, effect of permittivity of the holding substrate, and effect of air gap variation on SAW phase velocity and other parameters. The practical effectiveness of NCIDT SAW devices is also discussed.

3.5.1 Effect of properties of the holding substrate on SAW phase velocity

In the proposed configuration of SAW device a holding substrate is used to support the IDT floating in air. The dielectric constant of the holding substrate plays role in changing the SAW phase velocity and device response [13]. The perturbation effects due to the presence of an object above the surface of the substrate are reported by many authors. Kino *et al.* [66] applied the normal mode theory for Rayleigh wave amplifier and discussed the effect of an air gap between the interacting media, the effect of the semiconductor thickness, and the effect of the permittivity of the substrate used to support the semiconductor. Wixforth *et al.* [68]

presented the change in SAW velocity as a function of conductivity and it is expressed as given below.

$$\frac{\Delta v}{v_0} = \frac{K_{eff}^2}{2} \frac{1}{1+\left(\omega_c + \omega\right)^2} \tag{45}$$

where, K_{eff}^2 is the effective coupling coefficient, $\omega_c = \sigma / \left(\varepsilon_1 + \varepsilon_2\right)$ is the conductivity relaxation frequency, ε_1 and ε_2 are the dielectric constants of the piezoelectric substrate and the half-space above, respectively. Elkordy [69] used the expression given in [68] and studied voltage tunable SAW hybrid devices where the electric field accompanying the propagating SAW couples to the mobile carriers in a semiconductor placed with an air gap above the piezo-substrate.

In this section the effect of dielectric constants on the SAW phase velocity is simulated by FEM using COMSOL Multiphysics. The effect of holding substrate on the resonance frequency, in fact SAW phase velocity, is demonstrated in three ways, (a) By varying the thickness of holding substrate, (b) By using different materials for the holding substrate, and (c) With and without the holding substrate.

(a) Effect of change in thickness of holding substrate on SAW phase velocity

A one port SAW resonator with NCIDT patterned on Si substrate having infinite number of IDT fingers and λ = 16 μm is considered for simulation. Owing to periodic nature of the IDT structure, one pair of IDT electrodes is used to model the NCIDT SAW resonator as described in Section 3.1, and periodic boundary conditions are applied. The simulation is carried out by FEM using piezo plain strain application mode provided in COMSOL Multiphysics [15]. The 2D geometry of a periodic segment of NCIDT SAW resonator considered for simulation is shown in Figure 3.9. The dimensions used for simulation are as given in Section 3.1. The thickness of holding substrate is varied from 0.06λ to 2λ. The boundary conditions and meshing used for simulation are as given in Section 3.1. The eigenmode analysis is performed to calculate the resonance frequency and antiresonance frequency. The SAW phase velocity is calculated using equation (33).

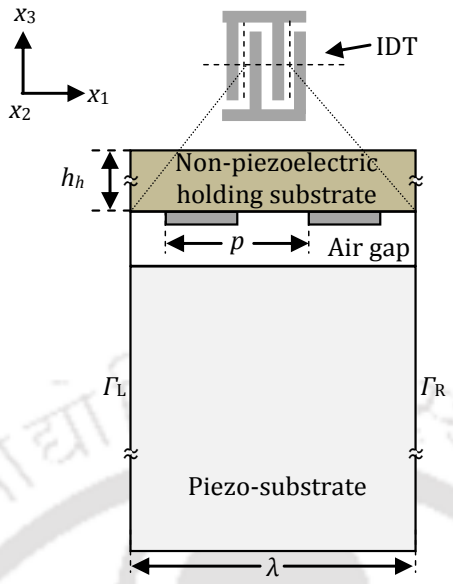

Figure 3.9 2D geometry of one port SAW resonator with NCIDT used in the simulation to study the effect of thickness of the holding substrate.

A series of simulations using COMSOL Multiphysics is performed to calculate the resonance frequency and anti-resonance frequency of the resonator and consequently the SAW phase velocity for various thicknesses h_h of the substrate used to hold the NCIDT. The plot of

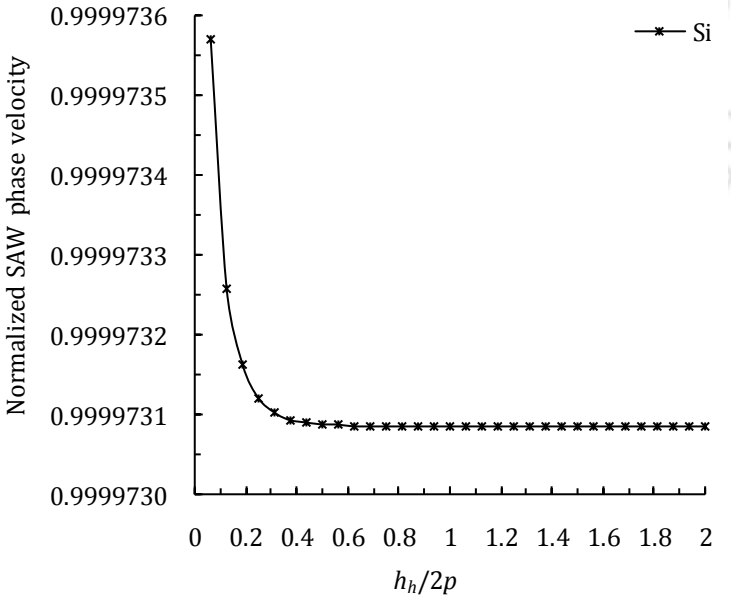

Figure 3.10 Normalized SAW phase velocity as a function of normalized thickness of holding substrate.

normalized SAW phase velocity (v/v_0) as a function of normalized thickness of the holding substrate is illustrated in Figure 3.10. It is observed that the SAW phase velocity decreases as the thickness of the holding substrate increases. The SAW phase velocity is almost saturated for the thickness of the holding substrate greater than 0.5λ and the change in velocity is negligible. In practice, the effect of the thickness of holding substrate on SAW phase velocity is negligible as in real devices the thickness of holding substrate will be much greater than 0.5λ. Accordingly the simulations carried out in the thesis consider adequate thickness for the holding substrate.

(b) Different materials used for holding substrate

The simulation is continued to study the effects of the various properties of materials used for the holding substrate on SAW phase velocity. Apart from Si, the material chosen for the holding substrate are Poly Si, FR4, and SiO_2. The simulation methodology adopted is the same as followed in subsection 3.5.1(a). The simulation is repeated for various thicknesses of the holding substrate for each material. The eigenmode analysis is performed to calculate the resonance frequency and antiresonance frequency of the SAW resonator in COMSOL Multiphysics and the SAW phase velocity is calculated using equation (33). Table 3.5 gives resonance frequency and SAW phase velocity of one port NCIDT SAW resonator with holding substrate thickness of 16 μm and air gap of 4 μm for different materials of holding substrate. Table 3.5 shows that the resonance frequency and SAW phase velocity are equal for FR4 and poly Si that have very close permittivity values, and it implies that the permittivity of the holding substrate is the sole dominant parameter affecting the SAW phase velocity and consequently the resonance frequency of the SAW resonator. Using the free surface SAW phase velocity of 3477.914 m/s, the resonance frequency with free surface is 217.36963 MHz

TABLE 3.5
RESONANCE FREQUENCY AND SAW PHASE VELOCITY FOR DIFFERENT HOLDING SUBSTRATES

Holding substrate material	Permittivity (F/m)	Resonance frequency (MHz)	SAW phase velocity (m/s)
Si	11.7	217.363294	3477.820566
FR4	4.5	217.363326	3477.824804
Poly Si	4.5	217.363326	3477.824804
SiO_2	4.2	217.363330	3477.825229

for λ = 16 μm. With Si, Poly Si, FR4, and SiO_2 as the holding substrates in NCIDT SAW resonator, the plots of normalized SAW phase velocity (v/v_0) as a function of normalized thickness of the holding substrate are shown in Figure 3.11. In all the four cases the change in the SAW phase velocity is negligible for the holding substrate thicknesses of greater than 0.5λ. For the SAW phase velocity to be close to free surface velocity, the permittivity of the holding substrate should be as low as possible.

(c) NCIDT with and without holding substrate

The NCIDT SAW resonator of 16 μm wavelength with and without holding substrate is simulated. Silicon is used as the holding substrate and its thickness is 16 μm and the air gap is 4 μm. The boundary conditions and other dimensions are as mentioned in subsection 3.5.1(a). The displacement profiles of the NCIDT SAW resonator with and without holding substrate are shown in Figure 3.12. The SAW phase velocity and resonance frequency with and without holding substrate are tabulated in Table 3.6. From Table 3.6, it can be seen that with reference to free surface resonance frequency f_0, the resonance frequency of the NCIDT SAW resonator with holding substrate is 6.34 kHz lower, whereas the resonance frequency of NCIDT SAW resonator without holding substrate is 6.099 kHz lower. It can be concluded that

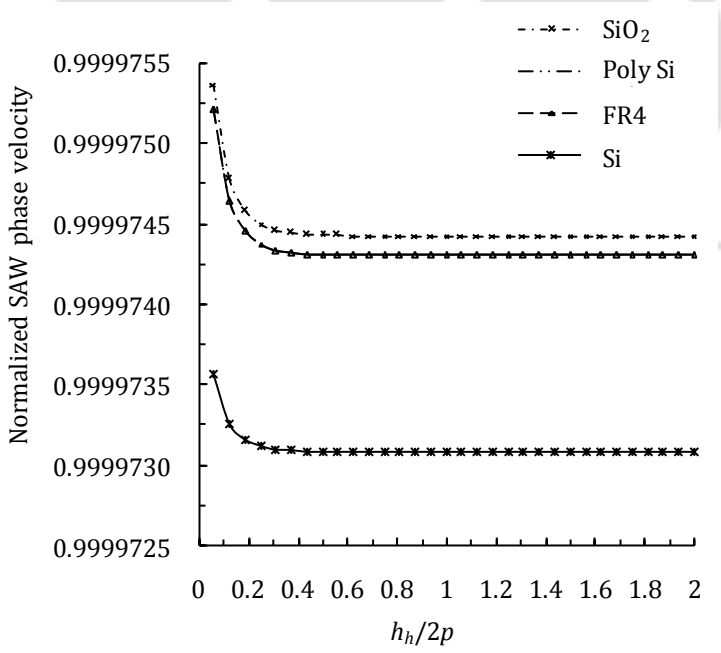

Figure 3.11 SAW phase velocity normalized with free surface velocity versus normalized thickness of holding substrate for various materials as holding substrate.

TABLE 3.6
RESONANCE FREQUENCIES AND SAW PHASE VELOCITIES OF NCIDT SAW RESONATOR WITHOUT AND WITH HOLDING SUBSTRATE

	Wavelength (μm)	Resonance frequency (MHz)	SAW phase velocity (m/s)
Free surface piezo-substrate	16	217.369630	3477.914173
NCIDT without holding substrate	16	217.363531	3477.855077
NCIDT with holding substrate	16	217.363290	3477.820566

the effect of short-circuiting of electric field by NCIDT is more prominent than the effect of permittivity of the holding substrate. The effect of short circuiting of electric field due to metallic IDT is discussed in section 3.6.

3.5.2 Effect of air gap on SAW phase velocity

This section presents the effect of air gap between NCDIT and piezo-substrate on the SAW phase velocity, resonance frequency, reflection coefficient, and coupling coefficient. Several researchers have reported the perturbation of the phase velocity with electric field coupling through air gap. Morgan [3] discussed the application of effective permittivity and the

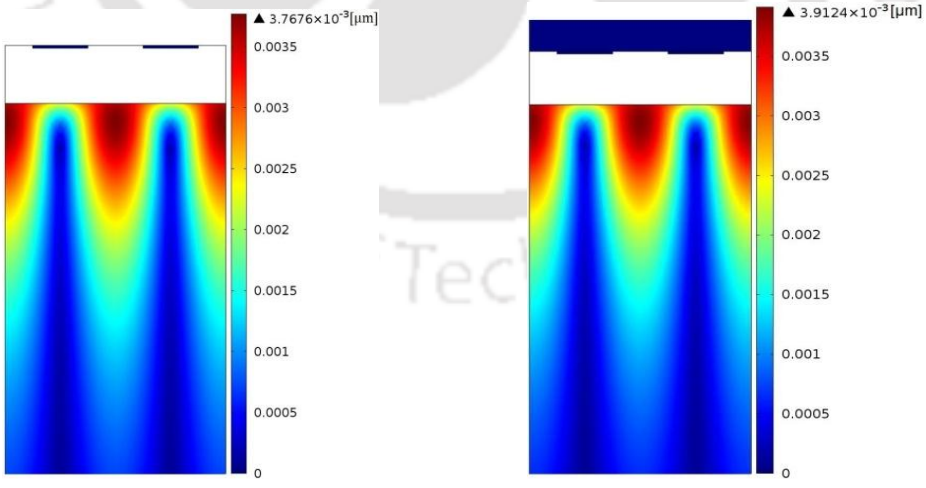

(a) (b)

Figure 3.12 Displacement profiles of NCIDT SAW resonators, (a) without holding substrate, (b) with holding substrate.

coupling between a piezoelectric half-space and a plane at a height. Coupling decreases exponentially with increase in the air gap, thus the gap has to be a small fraction of wavelength for the concept to be practically effective. Lakin [13] reported the perturbation theory for electromagnetic coupling to elastic surface waves on piezoelectric substrate and stated the following results. The normalized relative change in SAW phase velocity (δ_v) is given by

$$\delta_v = \frac{1-\tanh kh_a}{1+\varepsilon \tanh kh_a} \tag{46}$$

where h_a is air gap, k is the wave number, and ε is the permittivity of the material. The theoretical results for the decrease in the normalized perturbation coupling due to an increased air gap h_a are presented. The relative change in the coupling with air gap spacing is strongly influenced by the effective relative dielectric constants of the piezoelectric material. Ingebrigtsen [20] reported that a small air gap between piezo-substrate and adjoining medium may drastically reduce the coupling. Kino *et al.* [66] gave the normal mode theory for the Rayleigh wave amplifier. The relative velocity perturbation for a conducting plane at a distance of h_a with that at zero separation is expressed as

$$\frac{\Delta v(h_a)}{v(0)} = \frac{\left[1-\tanh(\beta_a h_a)\right]e^{-2\beta_a h_a}}{1+(\varepsilon_p/\varepsilon_0)\tanh(\beta_a h_a)} \tag{47}$$

where β_a is the unperturbed Rayleigh wave propagation constant, ε_p is the effective permittivity of the piezo-substrate[66]. The result obtained for YZ $LiNbO_3$ from equation (47) is verified with the direct field calculation reported by Campbell and Jones [67].

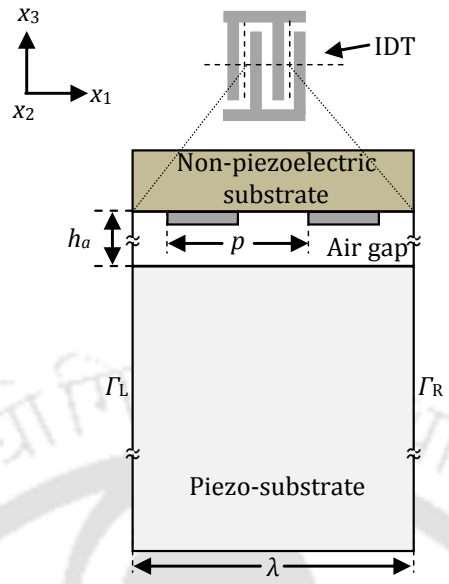

Figure 3.13 2D geometry of one port SAW resonator with NCIDT used in the simulation to study the effect of air gap between NCIDT and piezo-substrate.

The results of simulation of a one port SAW resonator with NCIDT having infinite number of IDT fingers patterned on Si substrate are given below. Owing to the periodic nature of IDT structure, one pair of IDT fingers as described in Section 3.1 is used with periodic boundary conditions. The simulation is carried out by FEM using piezo plain strain application mode provided by COMSOL Multiphysics. The 2D geometry of a periodic segment of NCIDT SAW resonator considered for simulation is shown in Figure 3.13. The dimensions used for simulation are as given in Section 3.1. The thickness of holding substrate is 16 μm. The air gap (h_a) between NCIDT and piezo-substrate is varied from 0.06 λ to 1.5 λ. The boundary conditions and meshing used for simulation are as given in Section 3.1. The eigenmode analysis is performed to determine the resonance frequency and anti-resonance frequency.

A series of simulations is performed to calculate the resonance frequency and anti-resonance frequency of the resonator for various values of air gap between NCIDT and the piezo-substrate. The SAW phase velocity v is calculated using equation (33). The plot of normalized SAW phase velocity (v/v_0) as a function of normalized air gap ($h_a/2p$) is shown in Figure 3.14. With the increase in the air gap, the effects of the permittivity of the holding substrate and the conductivity of IDT on the SAW velocity reduce, and the SAW phase velocity approaches the free surface velocity v_0 of the piezo-substrate.

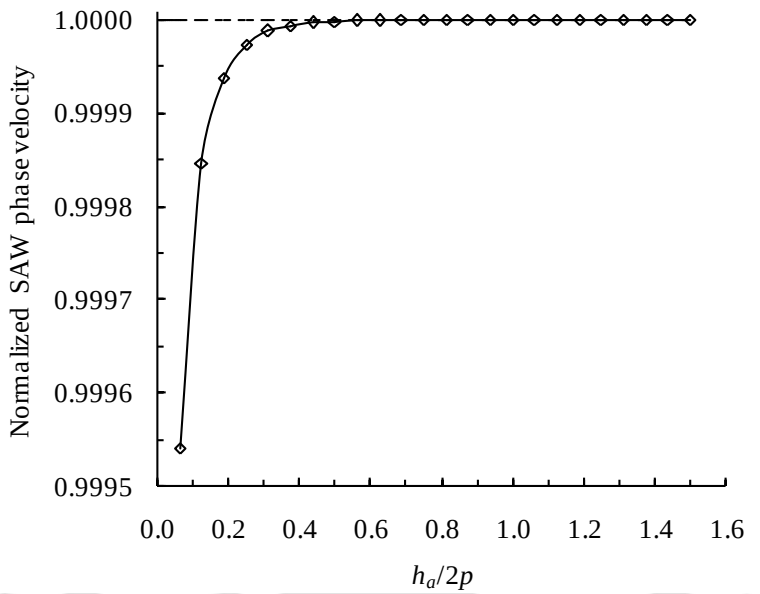

Figure 3.14 Normalized SAW phase velocity versus normalized air gap between NCIDT and piezo-substrate.

The electromechanical coupling coefficient K^2 of the NCIDT SAW device for various values of air gap between NCIDT and piezo-substrate is calculated. The electromechanical coupling coefficient K^2 is calculated from free surface velocity v_f for NCIDT configuration and metalized surface velocity v_m for NCIDT configuration. The expression for electromechanical coupling coefficient K^2 is expressed below [3], [70].

$$K^2 = 2\left(\frac{v_f - v_m}{v_f}\right) \tag{48}$$

The plot of electromechanical coupling coefficient K^2 as a function of normalized air gap between NCIDT and piezo-substrate is shown in Figure 3.15. The K^2 decreases sharply as the air gap increases. The K^2 of the NCIDT SAW resonator is 0.001 % for air gap of $\lambda/4$ (4 μm) and is close to zero for air gaps greater than $\lambda/2$. The low coupling of the device can be overcome to a large extent by using the large number of IDT finger pairs [6]. Owing to the reduced coupling, the NCIDT SAW device needs to be operated with adequately high gain amplifier and often high voltage excitation.

The presence of metallic electrodes on the surface causes changes in electrical and mechanical impedances at the surface and results in reflections whenever SAW encounters an IDT [4]. In conventional SAW devices, these reflections are significant as the substrate possesses strong electromechanical coupling and the material used for IDT has mechanical impedance very different from that of substrate material. In NCIDT, the effects related with the mechanical properties of the electrodes are completely eliminated due to separation of IDT from the piezo-substrate, and the effects related with the electrical properties of the electrodes are reduced to great extent due to the air gap between the piezo-substrate and NCIDT. The reflection coefficient $|\kappa_p|$ is one of the important parameters in the design of SAW resonators. The reflection coefficient of a transducer should be ideally zero while the reflection coefficient of a reflector should be one [3]. The reflections from electrodes cause considerable distortion, and reduce the frequency at which the conductance is maximum and susceptance is zero as reported by Skeie [71] and Morgan [3]. The reflections from IDT fingers can be reduced by splitting fingers into two [4].

The reflection coefficient per period of the NCIDT SAW resonator is calculated for various values of air gap between NCIDT and piezo-substrate. The reflection coefficient per period of the resonator is calculated from the upper and lower edges f_{sc+} and f_{sc-} of the stopband. The reflection coefficient per period $|\kappa_p|$ can be expressed as

$$|\kappa_p| = \pi\left(\frac{f_{sc+} - f_{sc-}}{f_0}\right) \tag{49}$$

where, f_0 is the center frequency of the stopband [23]. The plot of reflection coefficient per period $|\kappa_p|$ as a function of normalized air gap between NCIDT and piezo-substrate is shown in Figure 3.16. The reflection coefficient per period of NCIDT SAW resonator decreases sharply as the air gap increases. The reflection coefficient per period of the NCIDT SAW resonator is 0.014×10^{-3} for air gap of $\lambda/4$ (4 μm), and is close to zero for air gaps greater than ($\lambda/2$). If the reflectivity is weak, the SAW amplitude will not vary much over a distance of a few electrodes [3].

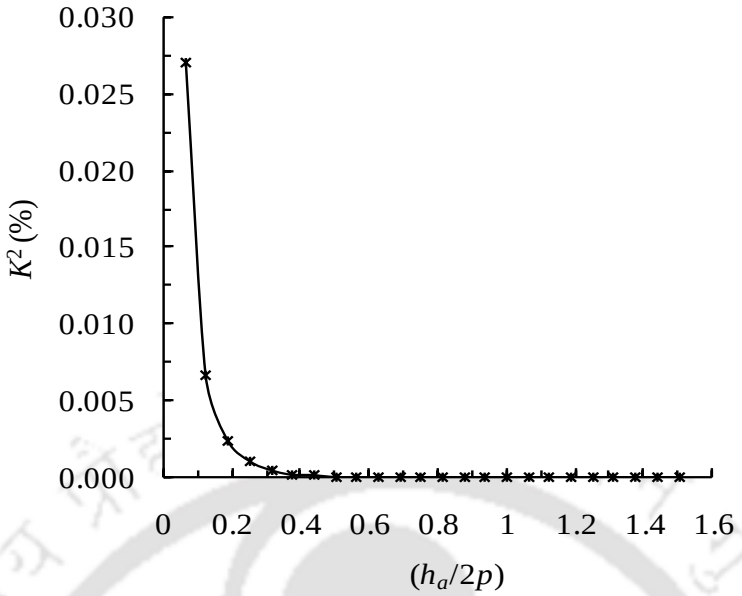

Figure 3.15 Electromechanical coupling coefficient versus normalized air gap between NCIDT and piezo-substrate.

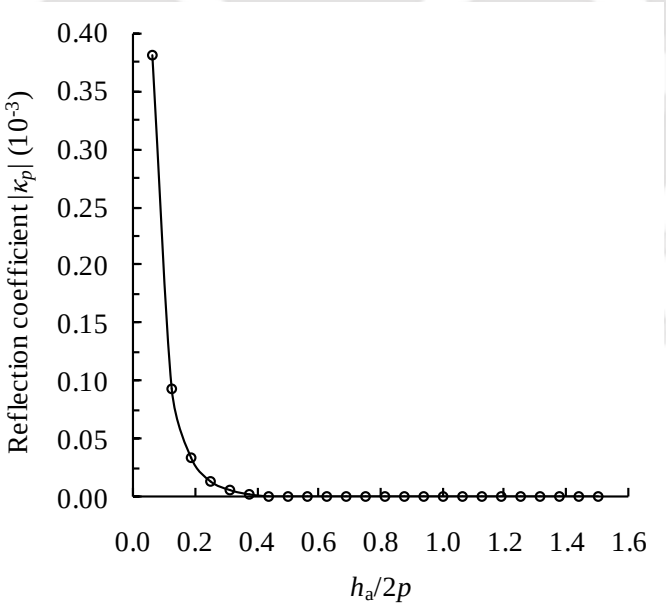

Figure 3.16 Reflection coefficient per period versus normalized air gap between NCIDT and piezo-substrate.

3.6 Secondary effects in NCIDT SAW devices

Chapter 2 discusses the secondary effects in conventional SAW devices. The IDTs in conventional SAW devices are fabricated over a piezo-substrate and induce secondary effects mainly due to mass loading and electrical loading of the metallic IDTs. In the proposed SAW devices, the NCIDTs are separated from the piezo-substrate and are made on a holding substrate. The electric field is coupled through a small air gap between NCIDT and the piezo-substrate. The following subsections investigate secondary effects in NCIDT SAW devices.

3.6.1 Mass loading effects of NCIDT in NCIDT SAW devices

The mass loading effects due to the presence of metallic IDT over the piezo-substrate in conventional SAW devices are presented in section 2.12. Similarly, the mass loading effects in the proposed NCIDT SAW devices are examined by changing the metallization ratio (MR) and the thickness of the NCIDT electrode fingers. The air gap between NCIDT and piezo-substrate is fixed at $\lambda/4$ (4 μm). The simulation results of the NCIDT SAW devices are compared with the simulation results of the conventional SAW devices given in section 2.12.

A one port NCIDT SAW resonator with different MRs is simulated for various thicknesses of NCIDT electrodes in COMSOL Mutiphysics. An identical conventional SAW device is simulated in section 2.12.1. A one port SAW resonator of wavelength of 16 μm is simulated. The air gap between NCIDT and piezo-substrate is fixed at 4 μm ($\lambda/4$). The dimensions and boundary conditions used for simulation are the same as given in section 3.2. The eigenmode analysis is performed to find the SAW phase velocity for various MRs and electrode thicknesses. The SAW phase velocity is calculated using equation (33). The MR is varied from 0.0125 to 0.9 for electrode thickness h_e ranging from 0 to 0.6 μm.

The plot of normalized SAW phase velocity as a function of MR for various values of electrode thicknesses is shown in Figure 3.17 (a). The normalized SAW phase velocity is given as v/v_0 where, v is the velocity of NCIDT SAW resonator for various values of MR and electrode thicknesses, and v_0 = 3477.914 m/s is the free surface SAW phase velocity as calculated in section 2.8.

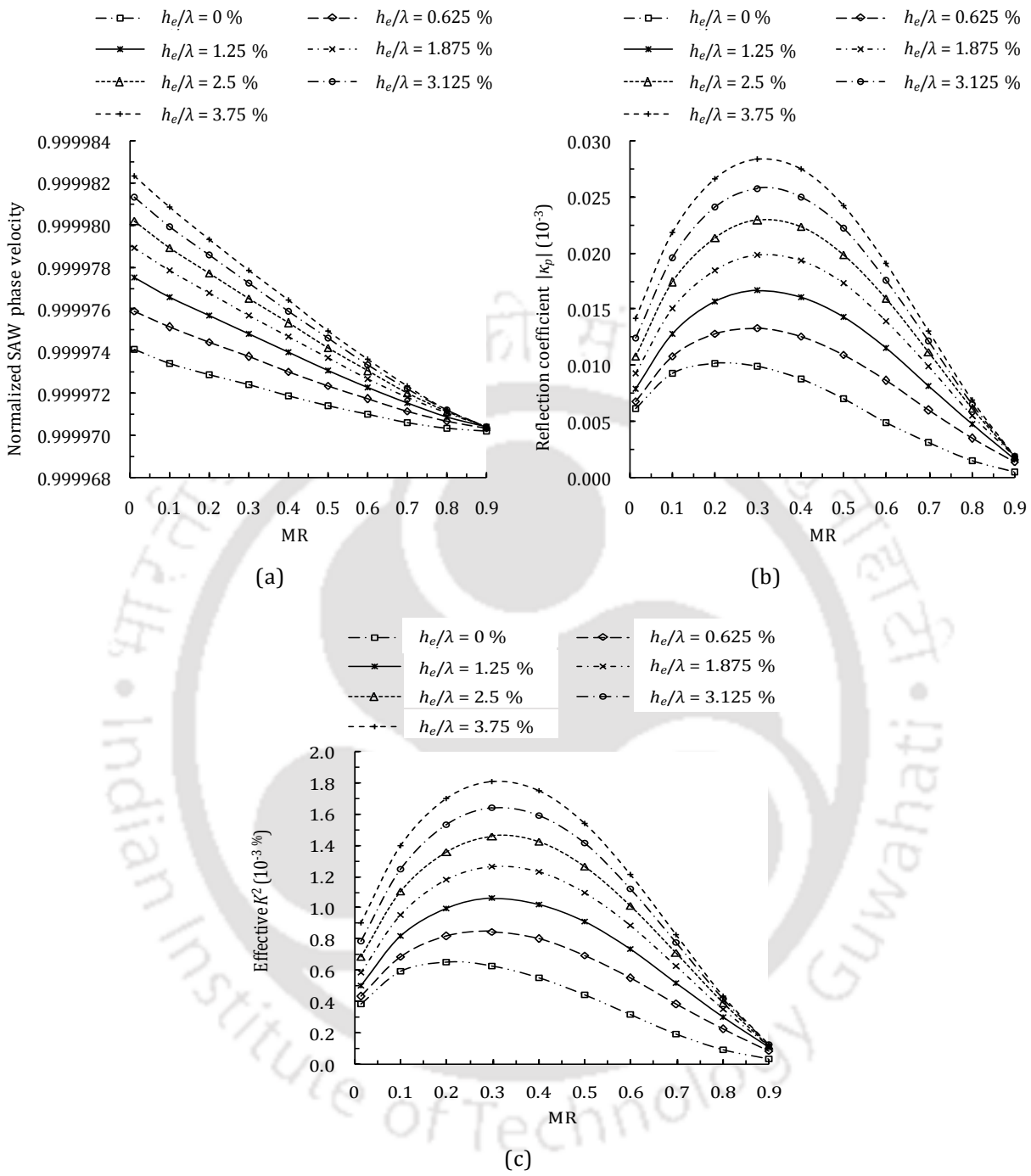

Figure 3.17 Results of simulation of NCIDT SAW resonator for varying metallization ratio (MR) and electrode thicknesses h_e. (a) Normalized SAW phase velocity versus MR for various electrode thicknesses, (b) Absolute value of the reflection coefficient per period $|\kappa_p|$ versus MR for various electrode thicknesses, (c) Effective electromechanical coupling coefficient K_{eff}^2 versus MR for various electrode thicknesses.

From Figure 3.17 (a) it is observed that the effect of MR and electrode thickness on SAW phase velocity in the NCIDT SAW device is negligible, about 0.0008%. The slight decrease in SAW phase velocity with increase in MR and electrode thickness may be attributed to distortion of electric field and change in permittivity, both effects greatly reduced due to the air gap.

The absolute value of the reflection coefficient per period $|\kappa_p|$ of NCIDT SAW resonator for different MRs and electrode thicknesses is computed using equation (38). The plot of $|\kappa_p|$ as a function of MR for various values of electrode thicknesses is shown in Figure 3.17 (b). In general, $|\kappa_p|$ is about 3 orders lower than the conventional SAW resonator and maximum for MR of about 0.3. For a given MR, $|\kappa_p|$ is greater for greater thicknesses of NCIDT electrodes.

The effective electromechanical coupling coefficient K_{eff}^2 of NCIDT SAW resonator is calculated using equation (39). The plot of K_{eff}^2 as a function of MR for various values of electrode thicknesses is shown in Figure 3.17 (c). As compared to an identical conventional SAW device, K_{eff}^2 in an NCIDT SAW device is 3 orders lower since the electric field is coupled through air gap. However the coupling coefficient in NCIDT SAW devices can be improved to large extent by using large number of IDT finger pairs. From Figure 3.17 (c), it is observed that K_{eff}^2 in NCIDT SAW device is maximum at MR of about 0.3. Since mechanical effects like reflection from IDT in NCIDT SAW devices are completely eliminated, MR of 0.3 is recommended instead of 0.5 for maximum coupling coefficient.

The Following three devices are compared for more insight into the loading effect of IDT in SAW devices. Figure 3.18 shows the plots of normalized SAW phase velocity versus MR for three identical devices: NCIDT SAW resonator with h_e = 0.2 μm, conventional SAW resonator with h_e = 0.2 μm and conventional SAW resonator with h_e = 0 μm which simulates massless electrodes. From Figure 3.18 the following observations are noted. With reference to the free surface SAW phase velocity, the change in velocity is greatest (2.2%) in conventional SAW resonator for maximum MR of 0.9. The change in velocity is a little lower (at 1.8%) when massless electrodes have been simulated. It implies that the effect of short circuiting electric field is more significant than the mass loading effect in the case under consideration. Comparatively, the change in SAW velocity is negligible for NCIDT with an air gap of 4 μm.

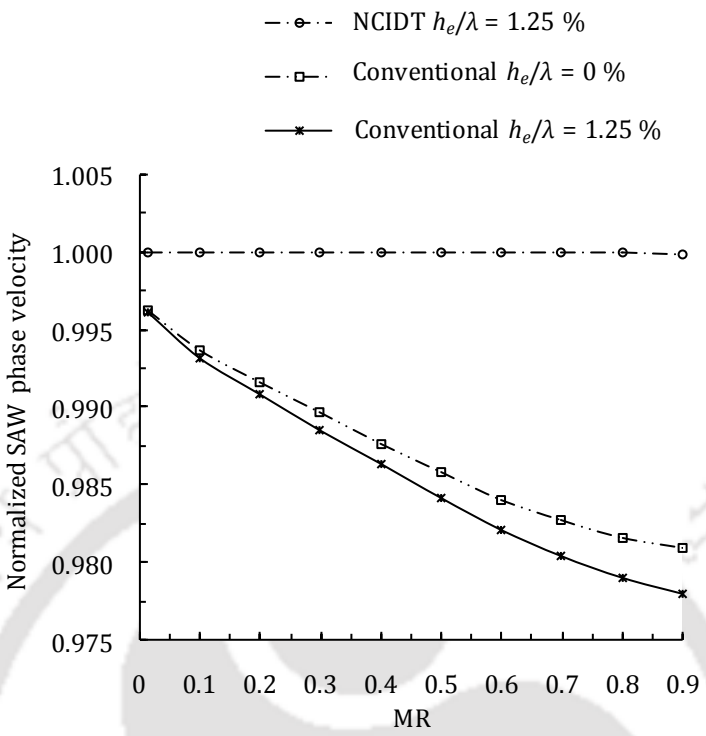

Figure 3.18 Plots of normalized SAW phase velocity versus metallization ratio (MR) in three cases: conventional one port SAW resonator having massless electrodes, conventional one port SAW resonator having 200 nm thick electrodes, and NCIDT one port SAW resonator with 200 nm thick electrodes.

Table 3.7 shows the values of SAW phase velocity in a common conventional SAW resonator with MR of 0.5 and Al electrodes of 0.2 μm thickness and in identical devices with massless electrodes and with NCIDT.

As seen from Table 3.7, with reference to the free surface SAW velocity, the SAW velocity is 55 m/s lower in conventional SAW resonator, 49 m/s lower for massless electrodes and 0.08 m/s lower for NCIDT electrodes. The SAW velocity in NCIDT is remarkably close to the free surface SAW velocity as the mass loading of electrodes in completely eliminated since the IDTs are not fabricated over the piezo-substrate and the effect of short circuit of electric field is reduced to great extent due to the air gap. More elaborate discussion about electrical loading in NCIDT SAW resonator is given in the following section.

3.6.2 Electrical loading effects of NCIDT in NCIDT SAW device

In conventional SAW device, the presence of IDT over the piezo-substrate gives mass loading as well as electrical loading as explained in section 2.12.2. The proposed NCIDT SAW device completely eliminates the effects related with the mechanical properties of the electrodes due to the separation of IDT from the substrate and greatly reduces the effects related with the electrical properties of the electrodes due to the air gap between the substrate and NCIDT. The effects of electrical loading in SAW devices with proposed configuration are demonstrated in this section. The results are compared with conventional SAW devices. One port SAW resonators with conventional and proposed configurations are simulated in COMSOL Multiphysics. The massless IDT electrodes with MR of 0.5 and λ of 16 μm are used. The other dimensions and boundary conditions in simulations are as adopted in section 2.9 and section 3.2. The eigenmode analysis is performed. The plot of the x-component of electric

TABLE 3.7

LOADING OF IDT

	SAW phase velocity (m/s)	Resonance frequency for λ = 16 μm (MHz)
Free surface piezo-substrate	3477.914173	217.369630
Conventional SAW resonator (MR = 0.5, h_e = 0.2 μm)	3422.892657	212.880126
Conventional SAW resonator (MR = 0.5, h_e = 0 μm)	3428.690075	213.362141
NCIDT SAW resonator (MR = 0.5, h_e = 0.2 μm, h_a = 4 μm)	3477.820560	217.363290

field associated with the surface wave along the surface of the piezo-substrate at resonance frequency is given in Figure 3.19. As discussed in section 2.12.2, the application of sinusoidal electric potential on IDT generates sinusoidal deformation on the substrate thus the electric field distribution to the surface of the substrate should be sinusoidal. From Figure 3.19, it is observed that the surface electric field under the IDT fingers in conventional SAW resonator is short circuited due to the metallic IDT fingers. The curves of the surface electric field for NCIDT and for free surface are almost overlapping. The *x*-component of electric field at the surface is almost unaffected in NCIDT SAW resonators due to the air gap. Consequently, the SAW velocity in the proposed device is much closer to the free surface SAW velocity which can be used to calculate the resonance frequency. The table of comparison of SAW phase velocity and resonance frequency in case of conventional and NCIDT SAW resonators for electrical loading is shown in Table 3.8.

TABLE 3.8
EFFECT OF ELECTRICAL LOADING ON SAW PHASE VELOCITY AND RESONANCE FREQUENCY

	SAW phase velocity (m/s)	Resonance frequency for λ = 16 µm (MHz)
Free surface piezo-substrate	3477.914173	217.369630
NCIDT SAW resonator	3477.814782	217.363182
Conventional SAW resonator with massless electrodes	3428.690075	213.362141

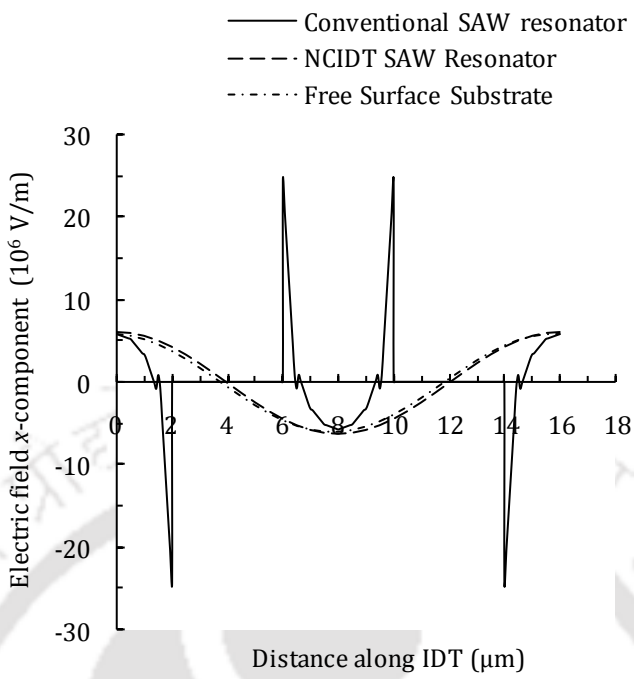

Figure 3.19 Surface electric field versus distance along propagation direction. The IDTs are placed from 2 to 6 μm and from 10 to 14 μm.

.

Resistive loss

In high frequency applications of SAW devices, the dimensions of IDT electrodes are very small and the electric resistance of IDT is considerable. It results in increase in insertion loss in SAW filters and decreases Q value of SAW resonators [21], [22]. To avoid the resistive loss, the resistance of the IDT should be sufficiently low. One way to get rid of resistive effects is to use thick IDT electrode fingers [21]. In case of conventional SAW devices, thick IDT electrodes will cause the mass loading adversely affecting the SAW device response. The effect of mass loading is demonstrated in section 2.12.1. The proposed NCIDT SAW device configuration provides the solution to reduce the effects of resistive losses. In this configuration, the IDT electrodes can be made thicker without causing mass loading effect. The simulation to demonstrate the mass loading effects in thick IDT electrodes is presented in section 3.6.1. The changes in resonance frequency and SAW phase velocity are negligible with variation in thickness of NCIDT electrodes.

3.6.3 BAW generation in NCIDT SAW devices

A brief theory related to bulk acoustic wave (BAW) is given in section 2.12.3. An NCIDT SAW delay line device with a delay line of 3λ (λ = 4 μm) is simulated in 2D structure using COMSOL Multiphysics to study BAW generation. The device used for the study of BAW generation is the same as given in section 3.4. The transit time analysis is performed for time duration of 15 ns. The total displacement of the SAW is recorded at different intervals of time during the analysis. Figure 3.20 (a) to (h) show the total displacement profile of generation and propagation of SAW over the surface of the piezo-substrate and BAW into the piezo-substrate observed at times 2.50 ns, 3.10 ns, 3.45 ns, 4.90 ns, 6.35 ns, 7.80 ns, 9.25 ns, and 10.7 ns after application of sine wave input. The total displacement profile shown in Figure 3.20 clearly shows that BAW generates at the substrate below IDT and travels inside the substrate. However the BAW attenuates as it travels along the depth of the medium. The amplitude of total displacement observed at the receiver at time 2.5 ns as extracted from Figures 3.20 (a) is 1.19 $\times 10^{-14}$ m. These displacements are purely transverse components of BAW as they are observed at time before SAW reaches at the receiver IDT. The BAW displacement in NCIDT is less than the conventional SAW device due to decrease in coupling strength.

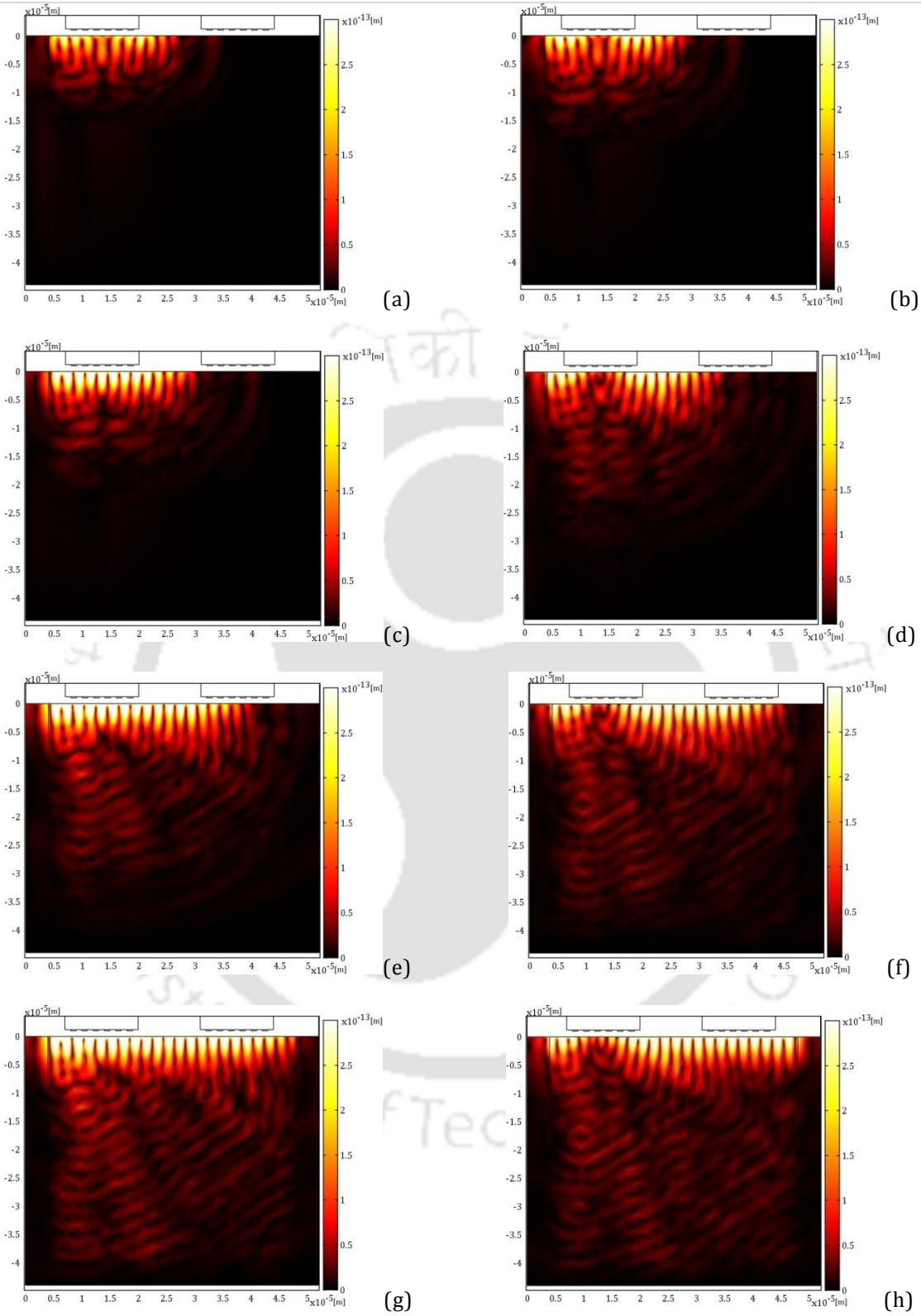

Figure 3.20 Total displacement profile in the SAW delay line device with IDT electrode thickness of 200 nm, showing propagation of SAW on the surface of the substrate and BAW into the interior of the substrate observed at times (a) 2.50 ns, (b) 3.10 ns, (c) 3.45 ns, (d) 4.90 ns, (e) 6.35 ns, (f) 7.80 ns, (g) 9.25 ns, and (h) 10.7 ns after application of sine wave input.

3.7 SAW sensors

The SAW devices basically operate in two configurations, viz. delay line configuration and resonator configuration as explained in chapter 2. The conventional SAW sensors are made by coating a sensing film over the piezo-substrate between IDTs in delay line configurations and over the IDTs and reflectors in resonator configurations. The change in the properties of sensing film due to the absorption of measurand alters the phase velocity of SAW and results in changes in the electrical parameters of the SAW sensor. Several authors have reported SAW sensors for the detection of chemicals, hazard gases, temperature, voltage, liquids, bio-molecules, and others [6]. The sensors made on SAW devices work on the principles of change in SAW propagation velocity and cause changes in the phase and resonance frequency by absorption of the measurand. The SAW sensors are mainly based on mass loading, change in conductivity, change in viscosity, change in temperature, and pressure.

In this thesis, two types of SAW sensors are simulated: 1. with direct mass load, and 2. with sensing film. In direct mass load type sensor, the measurand is added at the surface of the device and change in resonance frequency due to mass load of the measurand is measured. In the second type of sensor, a sensing film of selective material is coated on the surface of the device and exposed to the measurand. The shift in resonance frequency is measured for corresponding amount of measurand added to the sensing film.

3.7.1 SAW sensor with direct mass load

The direct mass load sensor simulated using water as the measurand. In this type of sensor the liquid is placed over the surface of the device substrate and the change in the response of the device is measured. A one port SAW resonator with NCIDT patterned on Si substrate having infinite number of IDT fingers is considered for FEM simulation. Owing to periodic nature of IDT structure, a one pair of IDT electrodes is used to model the NCIDT SAW resonator as described in Section 3.1, and periodic boundary conditions are applied. The simulation is carried out by FEM using piezo plain strain application mode provided by COMSOL Multiphysics. The 2D geometry of a periodic segment of the NCIDT SAW resonator considered for simulation is shown in Figure 3.21.

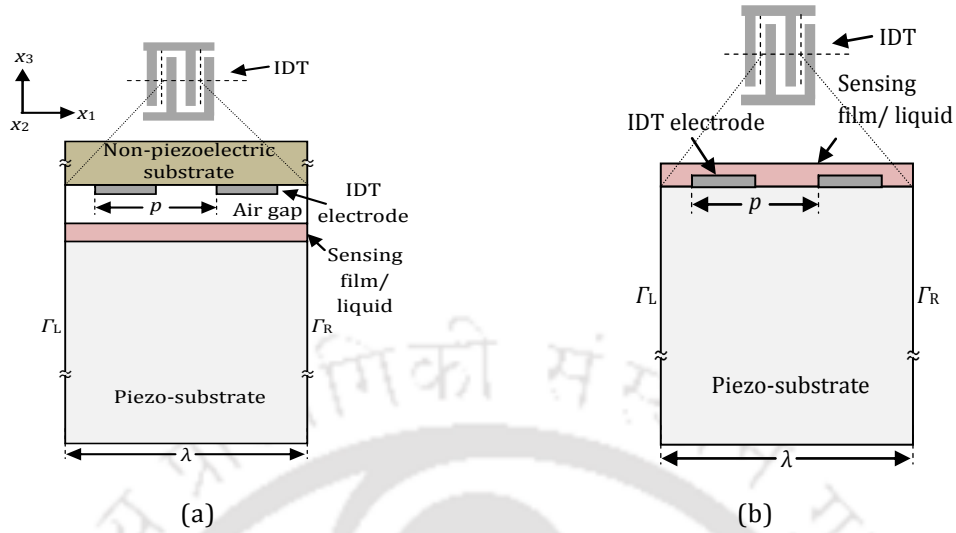

Figure 3.21 2D geometry used in the simulation of SAW resonator for sensing application, (a) using NCIDT SAW resonator, (b) using conventional SAW resonator.

The dimensions used for 2D simulation are as follows: NCIDT finger width (d) 1 μm, electrode pitch (p) 2 μm, electrode finger thickness (h_e) 0.2 μm, thickness of holding substrate of silicon (h_{Si}) truncated to 4 μm in x_3 direction, and depth of the piezo-substrate 10λ in $-x_3$ direction. The NCIDT is placed parallel over the piezo-substrate with an air gap of 2 μm. Water is placed over the surface of the piezo-substrate. The YZ $LiNbO_3$ is used as piezo-substrate. The material constants for piezo-substrate are as used in section 2.10, and are also given in Appendix C. The water properties used are from COMSOL Multiphysics materials library [15]. The bottom surface is fixed. The periodic boundary condition is applied to the left (Γ_L) and right (Γ_R) sides of device. The eigenmode analysis is performed to find the resonance frequency of resonators with and without water. The simulation is repeated for conventional SAW devices with identical dimensions.

The displacement profiles of the proposed NCIDT SAW resonator and conventional SAW resonator employed for sensing are shown in Figure 3.22. The resonance frequencies of the NCIDT resonator and conventional resonator with water and without water are given in Table 3.9. It can be seen from Table 3.9 that the sensitivity of NCIDT SAW sensor using direct mass load is about 6.6 times higher than the sensitivity of conventional SAW sensor. The significant increase in sensitivity in NCIDT SAW sensor is due to the absence of static mass of IDT on the substrate surface, facilitating detection of extremely small mass of the measurand added. In

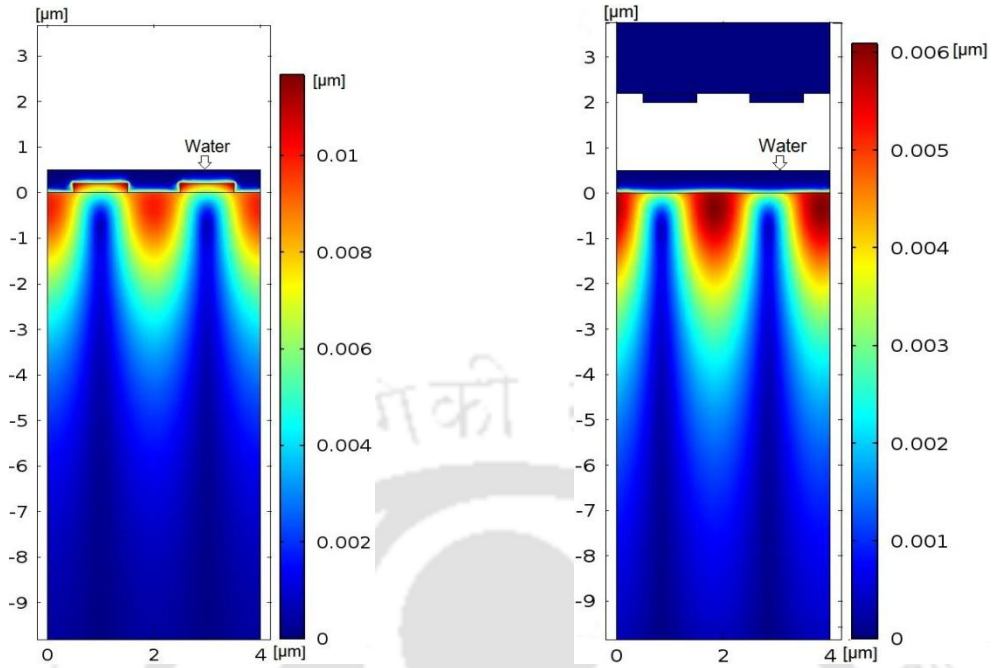

Figure 3.22 Total displacement profiles at resonance frequency for (a) conventional SAW sensor, and (b) NCIDT SAW sensor.

fact the presence of IDT over the piezo-substrate in conventional SAW sensors may swamp the mass loading effect.

3.7.2 SAW sensor with sensing film – Organic vapor sensors

SAW organic vapor sensors using proposed NCIDT configuration are simulated in COMSOL Multiphysics. The organic vapors are trichloroethylene (TCE) and cis-1,2 dichloroethene

TABLE 3.9

DIRECT MASS LOAD SAW SENSORS

Device	Resonance frequency (MHz)		Shift in resonance frequency (MHz)
	Without water	With water	
Proposed NCIDT SAW sensor	869.477482	860.991419	8.486063
Conventional SAW sensor	840.448174	839.168932	1.279251

(DCE). The polyisobutylene (PIB) film is used as the sensing medium. The device response is noted in the presence and absence of vapors. The sensitivity is obtained from the resonance frequency shift for various concentrations of the organic vapors. The organic vapor sensors are simulated in two steps. In the first step, the SAW resonator coated with PIB sensing film is simulated and the resonance frequency is noted. In the second step, the shift in resonance frequency of the SAW device after absorption of organic vapor is obtained. The sensitivities of the NCIDT SAW sensors and an identical conventional SAW sensors are compared.

(a) Structures of NCIDT SAW sensors

To simulate the organic vapor SAW sensors, one port SAW resonator with NCIDT patterned on Si wafer having infinite number of electrodes is considered. Due to the periodic nature of IDT structure, one pair of IDT fingers is used and periodic boundary conditions are applied as described in section 3.2. The simulation is carried out by FEM using piezo plane strain application mode provided by COMSOL Multiphysics [15]. The 2D geometry of one wavelength of NCIDT SAW resonator used for simulation is shown in Figure 3.21 (a). The dimensions are as follows: NCIDT electrode width (d) 1 μm, electrode pitch (p) 2 μm, electrode thickness (h_e) 0.2 μm, air gap (h_a) 2 μm, holding substrate thickness 4 μm in x_3 direction, and depth of the piezo-substrate 10λ in $-x_3$ direction. The YZ $LiNbO_3$ is used as piezo-substrate. The values of elastic constants, permittivity constants, stress constants, density are given in Appendix C. Silicon is used as the holding substrate. A PIB sensing film of 0.5 μm is coated over the piezo-substrate. The NCIDT is placed parallel over the piezo-substrate and sensing film. The separation between surface of the piezo-substrate and NCIDT electrode is taken 2 μm. The bottom boundary of the piezo-substrate is fixed and all other boundaries are traction free. The periodic boundary condition is applied to left (Γ_L) and right (Γ_R) sides of the device shown in Figure 3.21 (a). The optimized mesh density of 32 mesh elements per wavelength is employed. The eigenmode analysis provided by COMSOL Multiphysics is used to determine the resonance frequencies of the sensor.

(b) Organic vapor sensing

A PIB film is coated over the surface of the device substrate. The absorption of organic vapor increases the density and thickness of the PIB film. The change in density and thickness of the PIB film due to absorption of the organic vapor is adopted from Zhao *et al.* [72] which is based on the perturbation approach reported by Martin *et al.* [73]. The density ρ_0 and

thickness h_0 of the PIB sensing film in the presence of various concentrations c_v of organic vapor in air can be expressed as given in equation (50) and equation (51).

$$\rho(c_v) = \frac{\rho_0 + k_p c_v}{1 + k_p c_v / \rho_v} \tag{50}$$

$$h(c_v) = h_0\left(1 + \frac{k_p c_v}{\rho_v}\right) \tag{51}$$

where, k_p is the air/sensing film partition coefficient for measurand vapor, and ρ_v is the vapor density [73]. The parameters of PIB sensing film and organic vapors as TCE and DCE are given in Appendix E. The sensor is exposed to organic vapor in air at atmospheric pressure and room temperature. The vapor concentration in air is calculated as given below.

$$c_v = \frac{cP}{RT} \tag{52}$$

where, c is the vapor concentration, P is the air pressure, R is the gas constant, and T is the air temperature. The absorption of organic vapor changes the density and thickness of the PIB sensing film which perturbs the SAW velocity and results in shift in the resonance frequency of the device. The shift in the resonance frequency is obtained by subtracting the resonance frequency of the device in the presence of organic vapor from that in the absence of organic vapor.

(c) Sensor response

Two organic vapor gas sensors are simulated: (1) TCE vapor gas sensor and (2) DCE gas sensor. The SAW resonator resonance frequency is 869.48 MHz without the sensing film. After coating the PIB sensing film over the surface of the device substrate the resonance frequency is shifted to 862.07 MHz. This frequency is taken as the reference for calculating the frequency shift. The total displacement profiles in NCIDT SAW sensor at resonance is shown in Figures 3.23 (a). The depth of the substrate is shown only up to 2.5 λ for simplicity. Exposing the sensors to the organic vapor, the resonance frequency decreases mainly due to increase in the density of the PIB film. In simulation, the density and thickness of the sensing film are changed for each concentration of the vapor according to equations (50), (51), and

(52). The simulations are performed for various concentrations of the vapor and the resonance frequency is noted. Subtracting the resonance frequency calculated for various concentrations of the vapor from the reference value gives the shift in resonance frequency for the particular vapor concentration. The plot of shift in resonance frequency for various concentrations of TCE vapor and DCE vapor is shown in Figure 3.24. All the simulations are repeated for an identical conventional SAW resonator as the vapor sensor. The 2D geometry of conventional SAW resonator in sensor configuration is shown in Figure 3.21 (b). The subdomain settings and boundary settings are the same as NCIDT SAW sensors. The total displacement profiles of the conventional and proposed SAW sensors are shown in Figure 3.23 and the plot of resonance frequency shift versus concentrations of TCE vapor and DCE vapor is shown in Figure 3.24.

(d) Results and discussions

The sensitivity of proposed NCIDT SAW sensor is 378.728 Hz/ppm and 130.200 Hz/ppm for TCE vapor gas and DCE vapor gas, respectively. The sensitivity of conventional SAW sensors

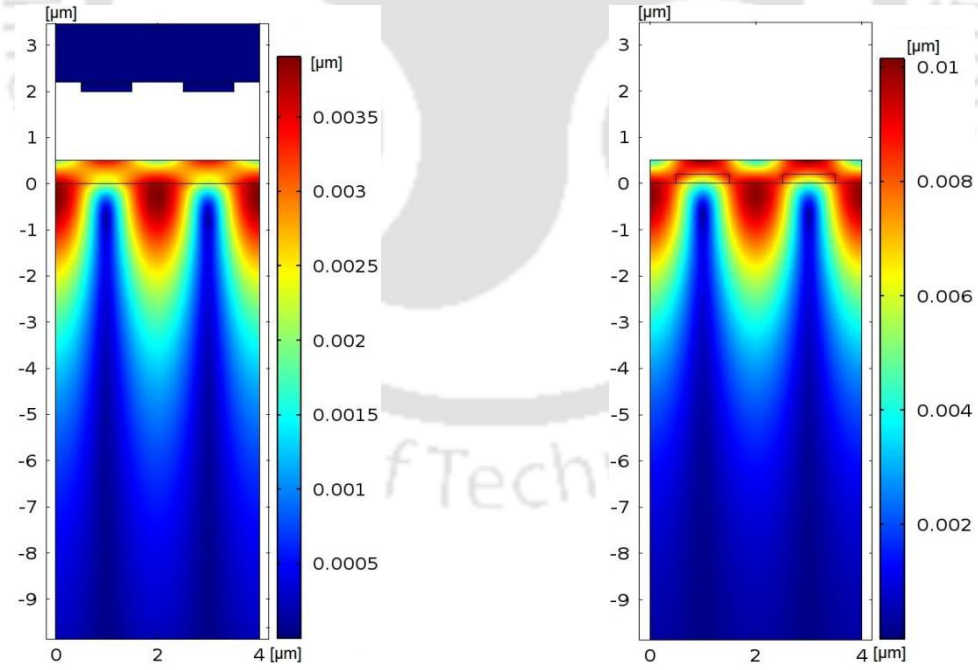

(a) (b)

Figure 3.23 (a) Total displacement profile of NCIDT SAW sensor with PIB film at the resonance frequency, (b) Total displacement profile of conventional SAW sensor with PIB film at resonance.

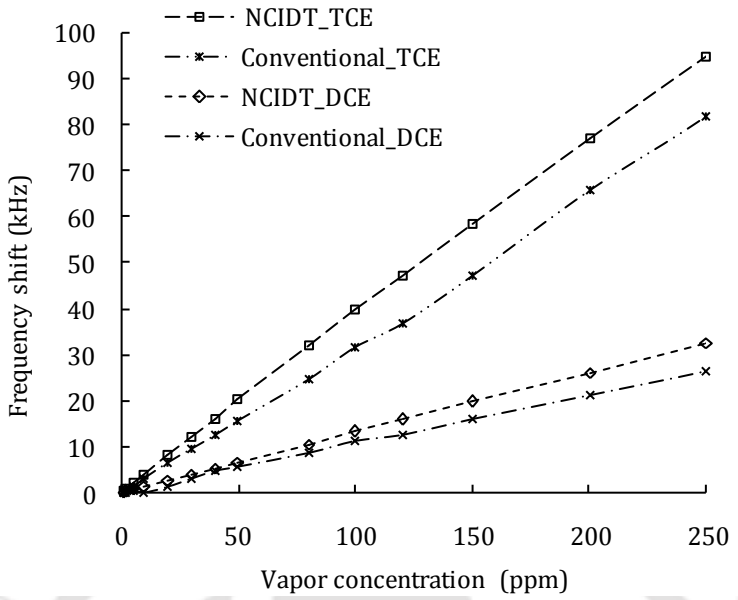

Figure 3.24 Frequency shift versus vapor concentration in ppm.

TABLE 3.10
SENSITIVITIES OF SAW SENSORS

SAW Devices	TCE vapor	DCE vapor
Proposed NCIDT SAW sensor	378.728 (Hz/ppm)	130.200 (Hz/ppm)
Conventional SAW sensor	328.036 (Hz/ppm)	114.076 (Hz/ppm)

is 328.036 Hz/ppm for TCE vapor and 114.076 Hz/ppm for DCE vapor. Table 3.10 compares the sensitivities of the proposed and conventional sensors. It is observed that the sensitivity of the NCIDT SAW sensor is about 12% greater than the conventional SAW sensor since the electric loading and mass loading imposed by IDT on SAW substrate are either completely eliminated or greatly reduced in the NCIDT SAW sensor. Hence the use the proposed NCIDT SAW sensor provides greater sensitivity than the conventional SAW sensor. In practice, NCIDT SAW sensor offers entire clean surface of piezo-substrate for sensing applications giving significant increase in sensitivity especially for the sensors based on mass load and conductivity. In addition, it will get rid of bonding wires that interfere with the coating process of sensing films.

3.8. Summary

This chapter is devoted to simulations of various types of the proposed non-contact IDT (NCIDT) SAW devices. NCIDT SAW resonators and delay line devices are mainly investigated. The first device simulated is NCIDT SAW resonator. A 2D Finite element analysis using COMSOL Multiphysics is carried out to determine device parameters such as resonance frequency, total displacement, harmonic admittance, transduction coefficient, quality factor, and capacitance ratio. These parameters are compared with the conventional SAW device parameters as given in chapter 2. It is observed that the total displacement and harmonic admittance at resonance of the NCIDT SAW resonator are about 2 orders and 4 orders lower than the conventional SAW resonator, respectively. Despite, the resonance frequency of the NCIDT SAW resonator is markedly close to the free surface resonance frequency. The excitation efficiency and quality factor are about 4 orders lower and 40 % less than conventional resonator. However, the capacitance ratio of NCIDT SAW resonator is 4000 times the conventional SAW resonator. To overcome the reduction in the excitation efficiency, the NCIDT SAW devices need to be operated with adequately high gain amplifier and often high voltage excitation. The low coupling in the NCIDT SAW device can be overcome to a large extent by using the large number of IDT finger pairs. Since the SAW velocity in NCIDT devices is close to the free surface SAW velocity, the NCIDT SAW devices have applications in the field of signal processing and communication where frequency accuracy is crucial.

A 3D finite element analysis is carried out to study the effect of aperture in the SAW devices. It is observed that the aperture has little effect on the device parameters, since Rayleigh wave has no component along the aperture, and small aperture length is sufficient to model a SAW resonator to study the resonance frequency, harmonic admittance and other parameters of the resonator.

A SAW delay line with NCIDT is simulated and the results are compared with an identical conventional SAW delay line. The *x* displacement and *y* displacement of NCIDT SAW delay line are 2 orders less than the conventional delay line device. The delay times of the conventional SAW delay line device and NCIDT SAW delay line are close to the delay time calculated from the free surface velocity.

The following aspects specific to the proposed NCIDT SAW devices are investigated in this chapter. The first parameter analyzed is effects of air gap between NCIDT and piezo-substrate on device parameters. The electric field coupling decreases exponentially with increase in the air gap, thus the gap has to be less than $\lambda/4$ for the device to be practically operational. The effects of the substrate holding NCIDT are analyzed by varying the thickness and by changing the holding substrate materials. The SAW phase velocity decreases as the thickness of holding substrate increases, however the change in velocity is negligible for the thickness of the holding substrate greater than 0.5 λ. By employing various holding substrate materials such as Si, FR4, poly Si, and SiO_2 it is found that the permittivity of the holding substrate is the only dominant property that affects the SAW phase velocity. The simulations of NCIDT SAW resonator with and without the holding substrate and the simulations with varying the metallization ratio show that the effect of short-circuiting of electric field by the metallic IDTs is significantly greater than the effect of permittivity of the holding substrate. Since the mass loading effect of the IDTs is completely eliminated in NCIDT, the NCIDT fingers can be made thicker for obtaining greater electromechanical coupling coefficient and reduced resistive losses in the IDT. The BAW displacement in NCIDT SAW devices is found to be less than the conventional SAW devices. In conclusion the following guidelines are recommended for designing a typical NCIDT SAW device. Keep the air gap less than $\lambda/4$, choose the substrate holding NCIDT of low permittivity and thickness greater than $\lambda/2$, implement the metallization ratio of 0.3 and use thick IDT fingers.

Two types of SAW sensors are simulated, direct mass load sensors and sensors with sensing film. In case of direct mass load sensor the shift in resonance frequency of NCIDT SAW sensors is found to be about 6.6 times greater than that in conventional SAW sensor. The significant increase in sensitivity in the NCIDT SAW sensor is due to the absence of static mass of IDT on the substrate surface. In the simulation of the second type of sensors, PIB sensing film is coated on the device substrate and used to sense TCE and DCE vapors. The presence of IDT over the piezo-substrate in conventional SAW sensors subdues the mass

loading effect by the sensing film. Hence the NCIDT SAW sensor provides greater shift in resonance frequency than the conventional SAW sensor.

4

SAW Devices with Electric Field Coupled Bond Pads

The previous chapter discussed about the two types of proposed SAW devices: 1. SAW devices with non-contact interdigital transducer (NCIDT) and 2. SAW devices with electric field coupled bond pads. The first type of SAW devices have been simulated in chapter 3. The results of simulation are compared with identical conventional SAW devices. Various aspects of SAW devices with NCIDT and secondary effects due to IDTs are discussed. Advantages of proposed SAW devices over conventional SAW devices are presented. NCIDT SAW sensors are simulated and their sensitivities are compared with conventional SAW devices.

This chapter deals with the study of the second type of SAW devices proposed viz., SAW devices with electric field coupled bond pads. It comprises of a piezo-substrate and IDTs fabricated on the piezo-substrate, and a pair of metal plates for external electrodes placed over the bond pads with or without an air gap. The pictorial representation of one periodic section of a conventional SAW device and the proposed SAW device with electric field coupled bond pads are shown in Figures 4.1 (a) and (b), respectively. The unique feature of the proposed device is the absence of the bonding wires. Normally, the electrical connections to the SAW device are realized through bonding wires connected to the bond pads on the SAW device. The bonding wires are fragile and offer inconvenience in some applications. In SAW

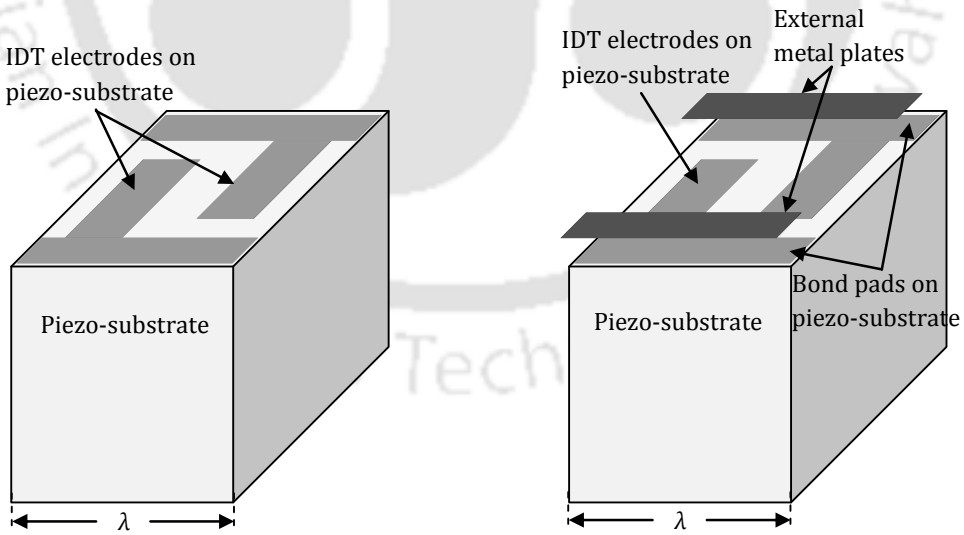

(a) (b)

Figure 4.1 Pictorial representation of one period of (a) conventional SAW device, (b) proposed SAW device with electric field coupled bond pads.

sensors the presence of bonding wires interfere with the coating procedures of the sensing films and limit the operating temperature of the device.

An attempt to get rid of bonding wires has been reported by Beck *et al.* [16] by demonstrating a SAW sensor in which the RF energy is coupled inductively. The IDTs in the device are connected to a large loop that communicates signals by transformer action.

In the proposed SAW device with electric field coupled bond pads, the IDTs are fabricated on the piezo-substrate conventionally and the signal is coupled to the IDT bond pads from the external electrodes using electric field coupling. The metal plates of the external electrodes can be fabricated on a suitable substrate like Si and FR4. The pictorial representation of proposed new SAW device with electric field coupled bond pads through external electrodes is shown in Figure 4.1. In the following section, a one port SAW resonator with bond pads using electric field coupling is simulated by FEM in COMSOL Multiphysics.

4.1 Simulation of one port SAW resonator with electric field coupled bond pads

The proposed configuration of SAW device with finite aperture is simulated in 3D. The IDTs are fabricated on the surface of the piezo-substrate. The metal plates of the external electrodes are placed above the IDT bond pads with an air gap. The simulation methodology and results are discussed below.

4.1.1 Simulation methodology

A one port SAW resonator having infinite number of IDT fingers with electric field coupled bond pads is considered for the simulation. Owing to the periodic nature of IDT, half period of IDT finger is used to model the SAW resonator. Periodic boundary condition with inverse sign is applied. The simulation is performed in 3D.

The piezo solid application mode provided by the COMSOL Multiphysics is used as described in section 2.10. In this simulation the end effects of bond pads on the harmonic admittance is neglected. The 3D geometry used for simulation is shown in Figure 4.2. The dimensions used for are as follows: IDT finger width (d) 1 μm, electrode pitch (p) 2 μm, electrode thickness (h_e) 0.2 μm, depth of the piezo-substrate 5 λ in – x_3 direction, and the aperture 1 μm to 4 μm in x_2 direction. The width of the bond pad is less than the aperture of the IDT. The metal plates of the external electrodes are placed parallel with an air gap of 1 μm above the bond pads fabricated on the piezo-substrate. The depth of the piezo-substrate is truncated to 5λ, as the SAW energy is concentrated in the substrate depth of one wavelength and it reduces the number of nodes and the cost of computation. The YZ $LiNbO_3$ piezoelectric material is used as the piezo-substrate. Al metal is used for IDT and metal plates of the external electrodes.

4.1.2 Results and discussions

The eigenmode analysis is performed in the simulation of the SAW resonator with electric field coupled bond pads. The resonance and antiresonance frequencies for various aperture widths are noted. The resonance frequency is identified from the list of eigenmode frequencies, the displacement amplitude and the mode of vibration. At resonance frequency the displacement is maximum at the middle of the space between fingers while at the

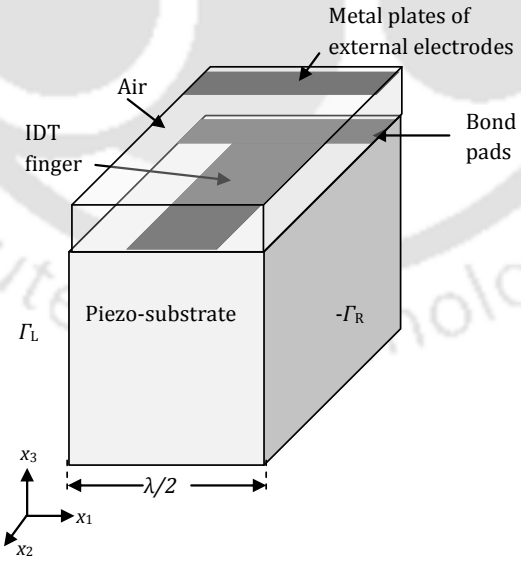

Figure 4.2 3D geometry of the one port SAW resonator with electric field coupled bond pads used in simulation.

antiresonance frequency the displacement is maximum at the middle of the fingers as given in section 2.8. The resonance frequency and antiresonance frequency of the resonator for aperture length W of 1 μm to 4 μm are recorded and tabulated in Table 4.1. An identical conventional SAW resonator is simulated. The eigenmode frequencies conventional SAW resonator are noted for aperture length W of 1 μm to 4 μm and tabulated in Table 4.2. It is observed that the resonance frequency of proposed SAW resonator is comparably more than the conventional SAW resonator.

The harmonic analysis of 3D model SAW resonator with electric field coupled bond pads and conventional SAW resonator is performed for aperture width of 1 μm for comparison. As discussed in chapter 2, the admittance value for given aperture is proportional to the aperture width. Thus a small aperture length is sufficient to model the SAW resonator with electric field coupled bond pads to study the resonance frequency, harmonic admittance and other parameters of the resonator. By this way one can minimize the computational cost as

TABLE 4.1
RESONANCE FREQUENCY VERSUS APERTURE IN SAW RESONATOR WITH ELECTRIC FIELD COUPLED BOND PADS

Aperture (μm)	Resonance frequency (MHz)	Antiresonance frequency (MHz)
1	858.167	863.843
2	856.397	863.524
3	855.583	863.254
4	855.065	862.789

TABLE 4.2
RESONANCE FREQUENCY VERSUS APERTURE IN CONVENTIONAL SAW RESONATOR

Aperture (μm)	Resonance frequency (MHz)	Antiresonance frequency (MHz)
1	839.759	846.329
2	838.730	848.212
3	838.249	848.882
4	837.897	849.060

mentioned in the section 2.7. Figure 4.3 shows the total displacement profile, *x*-displacement profile, and *y*-displacement profile at resonance frequency for SAW resonator with electric field coupled bond pads. The plot of harmonic admittance as a function of normalized frequency for aperture width of 1 μm is shown in Figure 4.4. The simulation of 3D model of SAW resonator with electric field coupled bond pads and conventional SAW resonator is performed with frequency resolution of 1 kHz which is found to be adequate.

The simulation results of SAW resonator with electric field coupled bond pads and conventional SAW resonator having aperture width *W* of 1 μm are compared in Table 4.3. The Table of comparison includes resonance frequency, total displacement and admittance. From Table 4.3 it is observed that the harmonic admittance of the SAW resonator with electric field coupled bond pads is about 2 orders lower than the conventional SAW resonator.

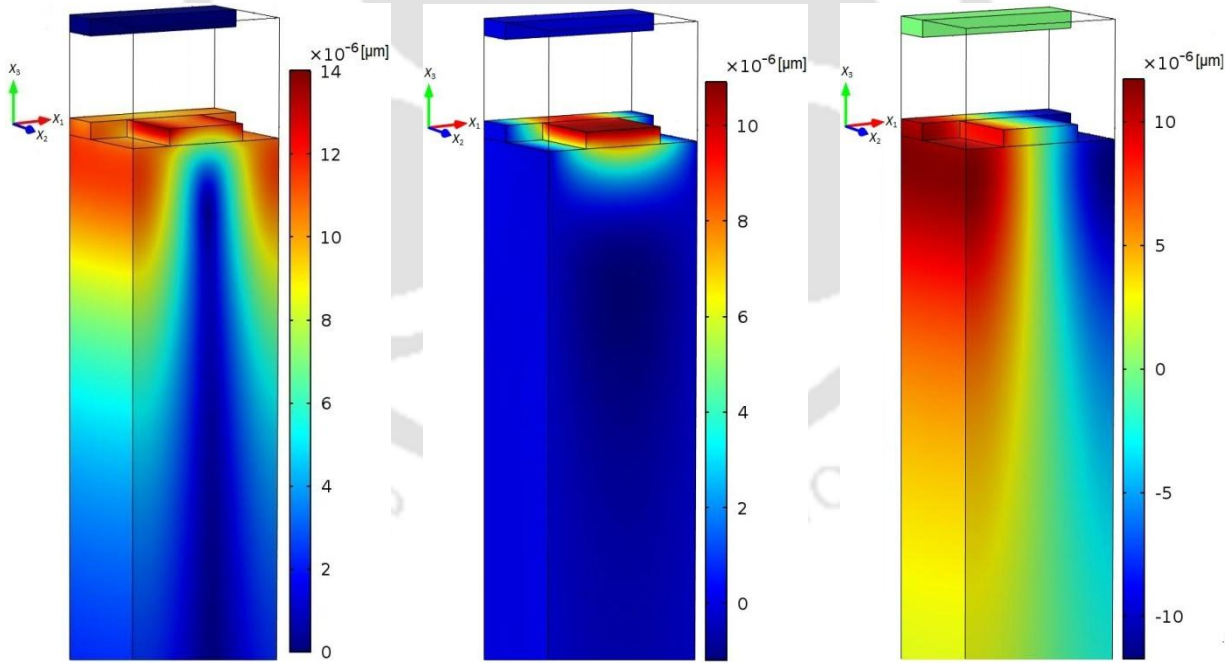

(a) (b) (c)

Figure 4.3 Displacement profiles at resonance frequency of 858.759 MHz for SAW resonator with electric field coupled bond pads, (a) Total displacement profile, (b) *x* displacement profile, (c) *y* displacement profile. Note: For simplicity the substrate depth of around 1.2 λ is shown.

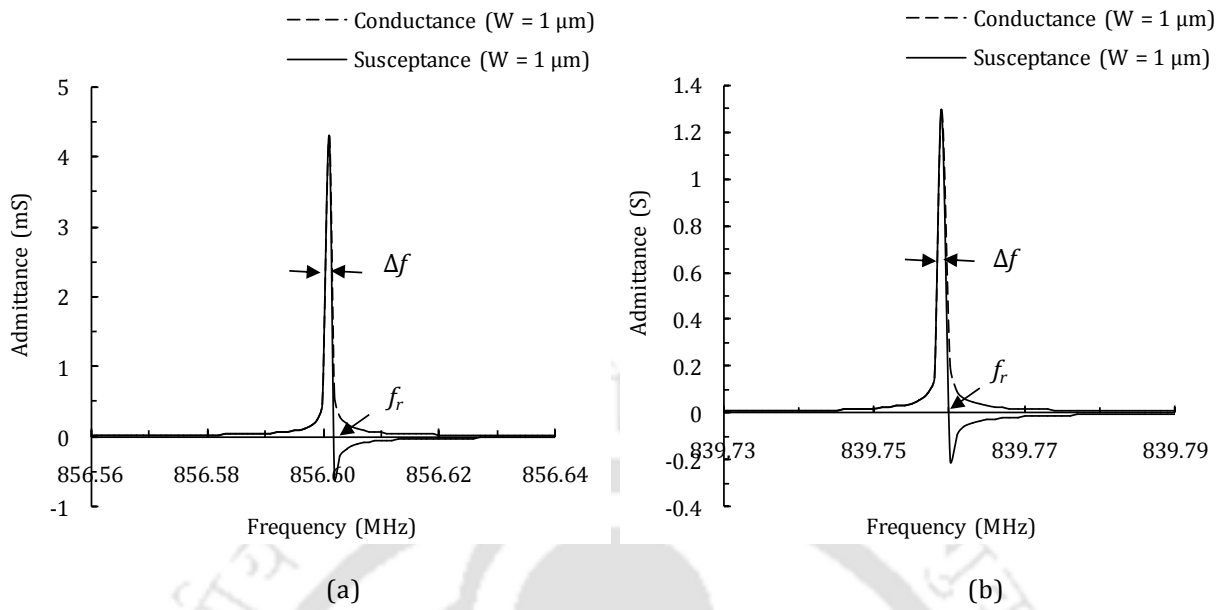

Figure 4.4 Plots of harmonic admittance as a function of frequency. (a) SAW resonator with electric field coupled bond pads. (b) Conventional SAW resonator.

The effectiveness of SAW excitation is characterized by the transaction coefficient per period. The transduction coefficient of the resonator is calculated from equation (44). To compare the two devices, the ratio of the corresponding transaction coefficients can be roughly estimated from the ratio of the corresponding conductance peaks. From Figure 4.4 (a) and (b), the ratio of the corresponding conductance peaks shows that the excitation efficiency in the SAW resonator with electric field coupled bond pads is about 2 orders lower than conventional SAW resonator. To overcome the reduction in the excitation efficiency, the

TABLE 4.3
COMPARISON OF SAW RESONATORS WITH ELECTRIC FIELD COUPLED BOND PADS AND CONVENTIONAL SAW RESONATORS (W = 1μm)

	Resonance frequency (MHz)	Harmonic admittance (mS)
SAW resonator with electric field coupled bond pads	856.601	6.075
Conventional SAW resonator	839.758	1824.757

NCIDT device needs to be operated with adequately high gain amplifier and often high voltage excitation.

The quality factors Q_r at resonance frequency f_r of the two devices are calculated from Figure 4.4 (a) and (b) using equation (34). The quality factor of the SAW resonator with electric field coupled bond pads is 744870.4 and is about 3% greater than that of the conventional SAW resonator.

The capacitance ratio which is a measure of the resonator performance is calculated from the resonance and antiresonance frequencies of the resonator. The expression for capacitance ratio is given in equation (35). The capacitance ratio for the NCIDT SAW resonator is 75.347 which is about 18% greater than the capacitance ratio of the conventional SAW resonator.

Figure 4.5 suggests a configuration of the IDT to realize a SAW device with electric field coupled bond pads. In conclusion, a conventional SAW device can be modified to have signals coupled capacitively to the bond pads using a detachable set of electrodes. The proposed device can also be used with zero air gap. The major drawback of the proposed SAW device with electric field coupled bond pads is the significant reduction in electromechanical coupling due to the air gap. The consequent reduction in signal amplitude has to be recovered by high voltage excitation and high gain amplifiers. However in the following cases the devices will have unique advantages. The proposed devices get rid of the bonding wires that cause inconvenience when conventional devices are used in applications like SAW sensors. In

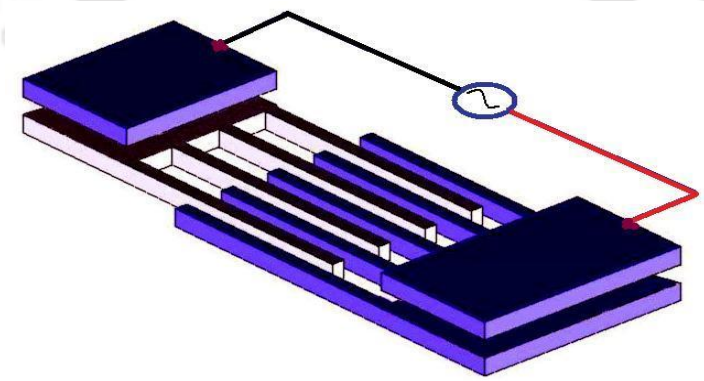

Figure 4.5 A configuration suggested for realization of the proposed SAW device with electric field coupled bond pads using external electrodes.

the absence of bonding wires the coating of the sensing films is extremely convenient. The device can be reused by removing and applying sensing films repeatedly. In addition, the configuration reduces one time-consuming step of connecting bonding wires in manufacturing process, improves mechanical robustness, and permits operating temperature above 400°C. The SAW device can be detached, isolated, and implantable. The metal plates of the external electrodes can be fabricated on a suitable substrate like Si and FR4. The device requires nearly the same chip area as in conventional SAW devices which have adequately large bond pads.

5

Micro Fabrication of SAW Devices with NCIDT

The simulation of the proposed SAW devices with non-contact IDT (NCIDT) is presented in chapter 3 and the results of simulation are compared with that of identical conventional SAW devices presented in chapter 2. The other type of the proposed SAW device with the bond pads coupled capacitively to external electrodes are presented In chapter 4. In order to validate the practicability of the proposed SAW devices, we have fabricated SAW resonators and SAW delay line devices containing NCIDT and tested their performance. This chapter deals with the design and fabrication of SAW devices with NCIDT configurations.

5.1 Fabrication of SAW devices with NCIDT

The conventional SAW devices can be predominantly fabricated using photolithographic patterning techniques used in the semiconductor industry [4]. Normally, aluminium (Al) metal is deposited on the surface of the piezo-substrate using thermal evaporation and IDTs are patterned using UV lithography followed by developing stage where the unwanted Al is removed by etching process. In the proposed configuration of SAW devices, the IDTs are fabricated on a suitable non-piezoelectric substrate and kept in close proximity with a piezo-substrate. We have fabricated the IDTs on two different substrates. For high frequency devices, the NCIDTs are fabricated on silicon (Si) substrate using conventional micro fabrication processes. For low frequency devices, it is convenient and quick to fabricate the NCIDTs over the copper clad FR4 material using a printed circuit board (PCB) prototyping machine. The fabrication of NCIDT on Si substrate is presented in the following sub-section. The fabrication of NCIDT over the copper clad FR4 sheet using a PCB prototying machine is presented in sub-section 5.1.2.

5.1.1 Fabrication of NCIDT using UV photolithography process

The basic steps involved in the fabrication of NCIDT on Si substrate using UV photolithography are as follows. Layout designs, mask generation, metal deposition over the clean wafer, UV photolithography, pattern development, etching, and wafer dicing [4].

There are two processes that are commonly used to pattern IDTs on wafers: etching and lift-off. Though both are used for fabricating SAW devices, the Lift-off is more suitable to develop IDT structure of feature size less than 5 µm. However, the etching process is simpler and easy to realize IDT patterns. In this work, etching processes is adopted and the minimum dimension of IDT pattern is about 17 µm.

(a) Design of NCIDT

In the proposed SAW devices, the NCIDTs are fabricated over the Si wafer as the holding substrate and kept facing on the $LiNbO_3$ substrate with a small air gap. This assembly forms the NCIDT SAW device. The $LiNbO_3$ piezo-substrates with one face mirror polished and the other surface lapped with #GC1000 have been procured from Roditi International, U.K.,. The dimensions of IDTs are either adopted from the published literature or are designed theoretically like the conventional SAW device [4], [6], [27], [74]. Some of the important criteria considered while designing the NCIDT for SAW devices are

i. The IDT structures are designed for admittance value of 20 mS. The parameters of the IDT are designed from the P–Matrix model described in chapter 2. Tables 5.1 and 5.2 show the designed parameters of the NCIDTs.

ii. Bond pads are designed to be compatible with a 200 µm pitch RF-probe. Bond pads are made far away from the IDT electrodes so that the $LiNbO_3$ substrate can easily be kept

TABLE 5.1
DIMENSIONS USED FOR FABRICATION OF NCIDT SAW DELAY LINE STRUCTURE

Parameters	Dimensions
Finger width	17 µm
Pitch	34 µm
Center–center separation between IDTs	7513 µm
Aperture	2000 µm
Number of IDT fingers	28

TABLE 5.2
DIMENSIONS USED FOR FABRICATION OF NCIDT SAW RESONATOR STRUCTURE

Parameters	Dimensions
Finger width	24.65 µm
Pitch	49.3 µm
Length of IDT	2021 µm
Aperture	2380 µm
Number of IDT fingers	41

above NCIDT during measurement. In some cases, large size bond pads are kept such that wires can be bonded over them using silver paste.

(b) Fabrication of NCIDT

The IDTs are fabricated on 3 inches Si wafers. The processes involved in the development of IDTs on Si wafer are as follows.

i. Layout designing

The structures to be patterned over the Si wafer are graphically designed using CleWin software. The screen shots of IDT designs for 3 inches wafer are shown in Figures 5.1 (a) and (b). Figure 5.1 (c) shows the magnified view of a pair of bond pads.

ii. Mask writing

The IDT can directly be patterned through laser writing on photoresist and Al coated Si wafer with high accuracy followed by other necessary fabrication processes. As the IDTs are to be fabricated in a whole 3 inch wafer, the direct laser writing will consume lots of time. Hence it is decided to pattern the IDT through UV lithography. The IDT layout for the mask is designed to fit maximum number IDTs in the 3 inch Si wafer.

Chrome plate masks for UV lithography are written using laser writer Microtech LW – 405. As the minimum dimensions of the pattern to be written is of 24.65 μm, lens 3 of the laser writer is employed. The laser writing process took 14 hours. The chrome plates are developed using MF 26A developer (MicroChem, USA). The exposed chromium is etched using chrome etchant solution. Chrome etchant solution contains ceric ammonium nitrate $(NH_4)_2Ce(NO_3)_6$ or sulfate $(NH_4)_4Ce(SO_4)_4.2\ H_2O$, with small amounts of HNO_3 [77]. The unwanted photo-resist is removed using acetone, followed by piranha cleaning process. An optical image of a portion of the mask given in Figure 5.2 shows that the mask has turned out properly and dimensions are as desired. The fabrication processes are summarized in Figure 5.3 (a)–(k).

iii. Cleaning of wafer

A 3 inch Si wafer is placed inside a beaker containing piranha solution (One part of H_2O_2 and 3 parts of H_2SO_4). Then wafer is placed in HF solution for few seconds. Finally, wafers are placed in de-ionized (DI) water and dried using filtered nitrogen gas.

iv. Al metal deposition

After cleaning the Si wafer, Al metal of thickness of 100 nm to 200 nm is coated over the wafer using thermal evaporator coating system. The Al pellets are cleaned using acetone and TCE. The pellets are etched with Al etchant for 5 minutes to remove the native oxides. Further, the pellets are dropped in DI water. Finally, the pellets are dried and dehydrated by heating them to a temperature of 120°C. This pellets cleaning method improves the adhesion of Al on the surface of the wafer.

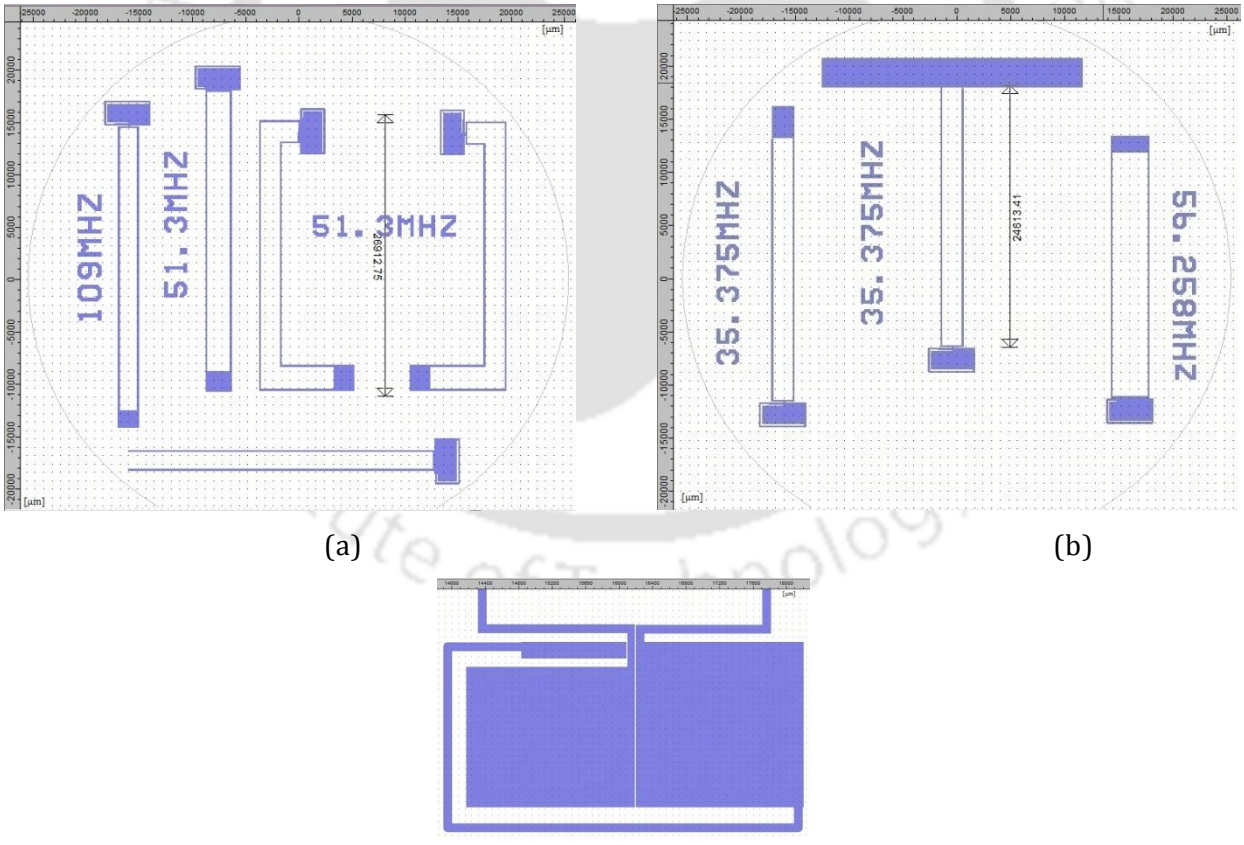

(a) (b)

(c)

Figure 5.1 (a) and (b) Layout using CleWin software for various NCIDT to be fabricated on Si wafer. (c) Magnified view of a pair of NCIDT bond pads.

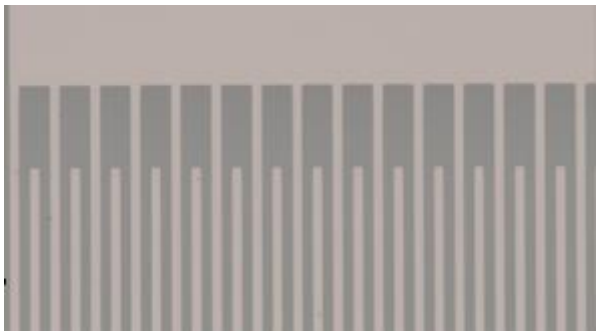

Figure 5.2 Optical microscope picture of the IDT pattern on the chrome mask plate.

After Al coating on Si wafer, the wafer is cleaned by acetone, isopropyl alcohol (IPA), and then blow dry. The clean metal coated wafer is kept on hotplate for 10 minutes at temperature 200°C and allowed wafer to cool in room temperature.

v. Photoresist coating

The wafer is then placed inside the spin coater. It is ensured that the centre of the wafer is exactly aligned with the spin coater. S1813 photoresist (Microchemicals, GmBH) is dispensed from the bottle and spread all over the wafer. The wafer is spun with a speed of 500 rpm/s for 5 s and followed by 4000 rpm/s for 40 s. Speed ramp of 500 rpm/s is maintained throughout the spinning processes. By this method, the photoresist coating thickness of about 1 µm is achieved over the wafer.

vi. Soft baking

The spun sample is soft baked by placing it in the hot plate at a temperature of 95°C for 60 s. To avoid wafer getting stuck to the hot plate surface, wipes are placed between wafer and hot plate.

vii. UV exposure

The spun sample is placed in UV mask aligner (EVG 620) substrate chuck. The exposure parameters such as wafer thickness, separation between the wafer and mask, exposure UV dosage of 75 mJ are set using the software program. The patterns in the mask are transferred to the photoresist and Al coated Si wafer by UV exposure. The UV exposed wafer with is shown in Figure 5.4.

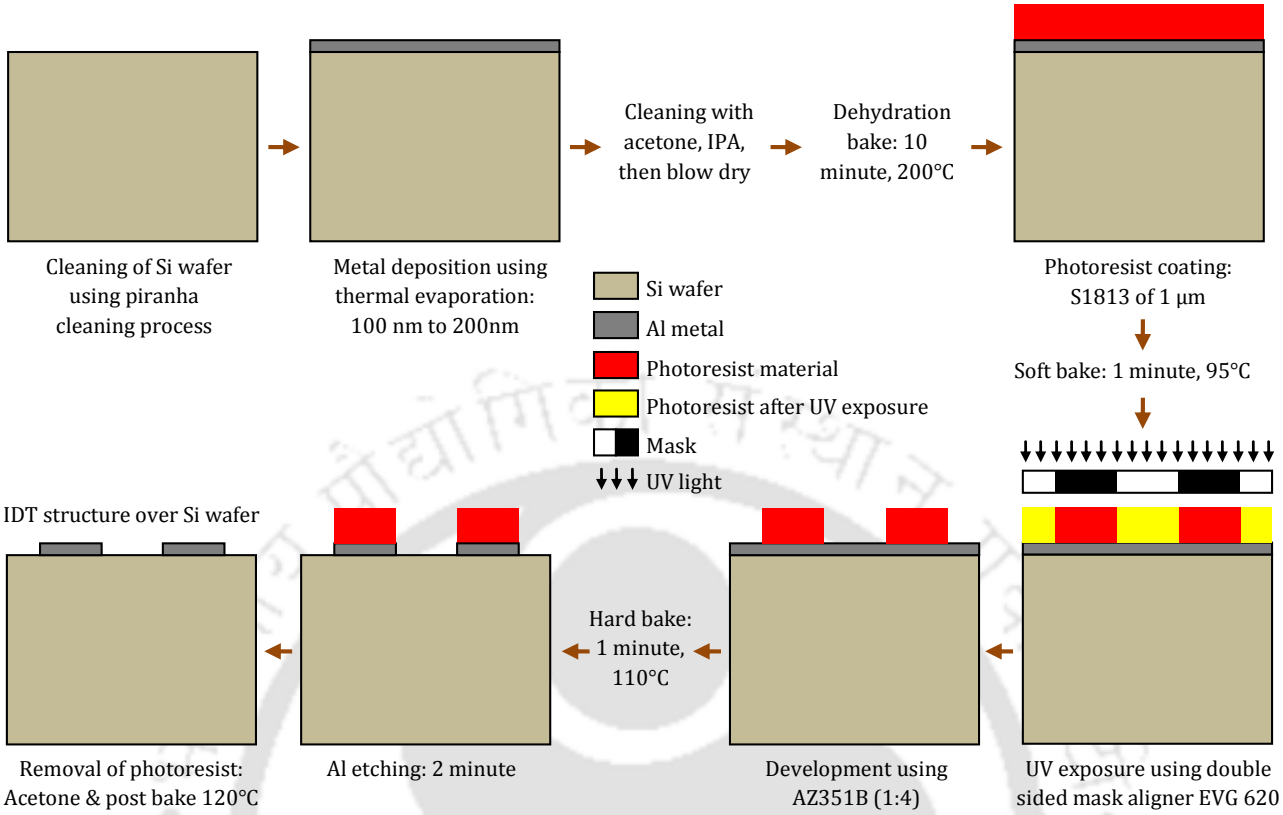

Figure 5.3 Process flow employed in the fabrication of NCIDT on Si wafer.

viii. Development of IDT structures

The UV exposed wafer is then dipped in AZ351B (1:4) solution for 30 s. The wafer is taken out from the developer solution once the patterns are identified in the wafer. If the wafer is placed for excess time it will lead to over development and finally end with poor patterns on the wafer.

ix. Post baking

The developed patterns are checked using optical microscope. The wafer is then hard baked by placing it in hot plate at a temperature of 110°C for 1 minute.

x. Aluminium etching

Aluminium etchant is prepared by mixing 19 ml of orthophosphoric acid with 1 ml of nitric acid and 4 ml of DI water. The etchant is prepared in bulk and stored in a bottle. The post baked wafer is then soaked in etchant solution for 1 minute to 2 minutes. Once the unwanted aluminium is etched out the wafer is immediately taken out from the etchant solution and

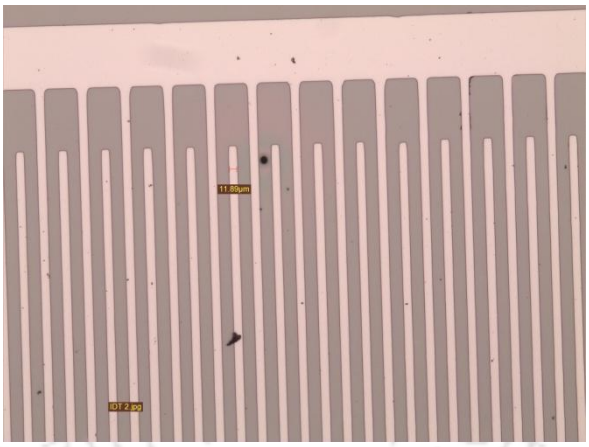

Figure 5.4 Optical microscopic image of a portion of fabricated finger patterns of an IDT.

placed in DI water. Excessive etching time will lead to undercut in the IDT. Therefore, the wafer is continuously monitored under microscope for every 30 s during the etching process. The wafers are then dried using nitrogen gas.

xi. Removal of photoresist

To remove photoresist, the wafer is placed in acetone bath for 2 minutes, followed by methanol and DI water, and subsequently dried with nitrogen gas. The fabricated IDT structure on Si wafer is shown in Figure 5.5.

The fabrication processes are optimized after many trials. The silicon wafer is chosen to facilitate monolithic electric circuits with NCIDT in future.

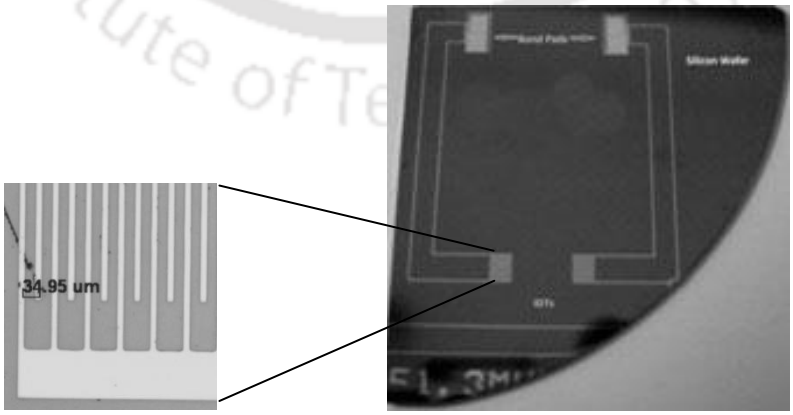

Figure 5.5 Optical image showing IDT structure with bond pads on Si wafer.

5.1.2 Fabrication of NCIDT using PCB prototyping machine

The NCIDT for low frequency SAW devices can be conveniently fabricated on a copper clad FR4 PCB using LPKF PCB prototyping machine. The picture of LPKF PCB prototyping machine is shown in Figure 5.6. The minimum dimension of IDT electrode width that can be designed using LPKF PCB prototyping machine is 0.1 mm. The NCIDT is designed using CircuitCAM 3.2 software. The designed NCIDT structures on CircuitCAM 3.2 software for delay line SAW devices are shown in Figure 5.7. The dimensions used for designing NCIDT are given in Table 5.3.

The designed IDT structures are then imported in Protel software for LPKF PCB prototyping machine. The copper clad board is secured well on the machine since a small mistake can damage the cutter. The optical images of the fabricated NCIDT structures are shown in Figure 5.8.

Figure 5.6 Picture of LPKF PCB prototyping machine.

TABLE 5.3

DIMENSIONS USED FOR DESIGNING OF NCIDT ON COPPER CLAD FR4

Parameters	Dimensions
Finger width	100 μm, 150 μm, and 200 μm
Aperture	28λ, 30λ, and 40λ
Length of delay line	3λ, 10λ, 12λ
Number of IDT fingers	50, 100, 120

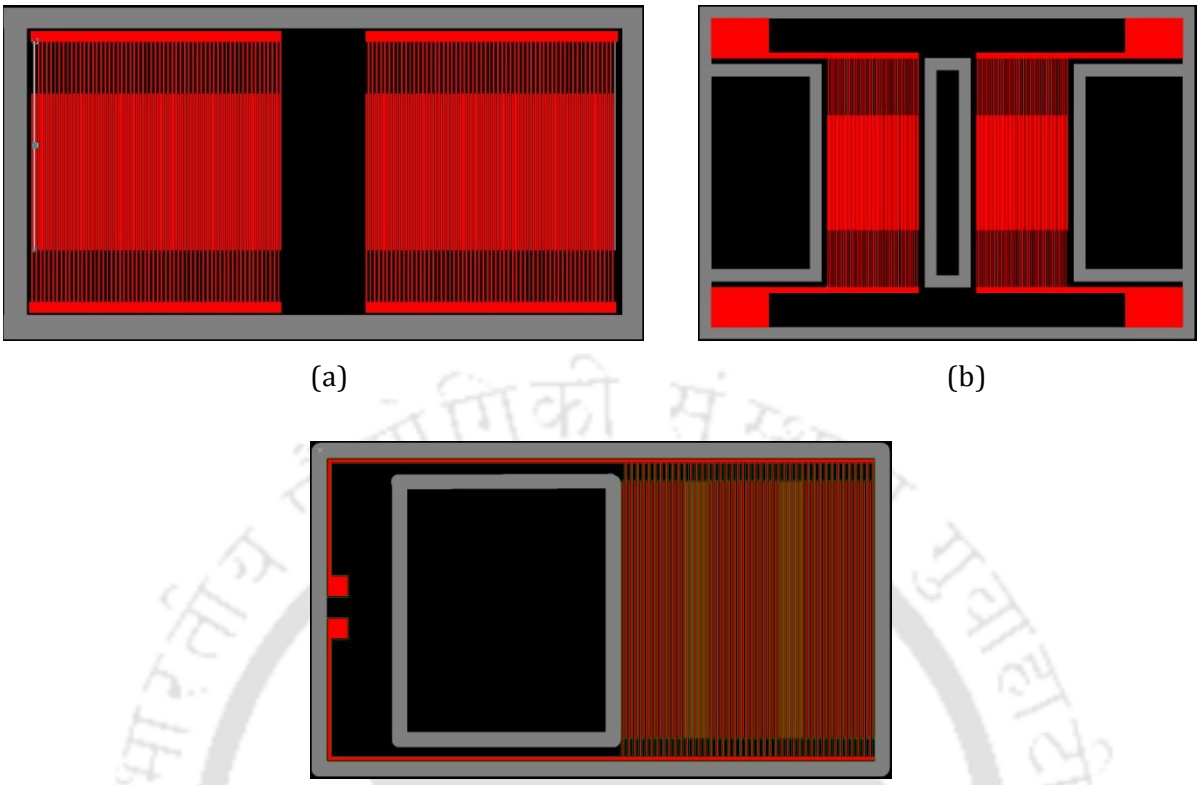

(a) (b)

(c)

Figure 5.7 (a), (b) and (c) Layout for various NCIDTs designed using CircuitCAM 3.5 software and to be fabricated on copper clad FR4 sheet using LPKF PCB prototyping machine. Note: red color shows the top layer for milling tools with micro cutter of 0.1– 0.2 mm and gray color shows the outline for cutting using contour router of 2 mm.

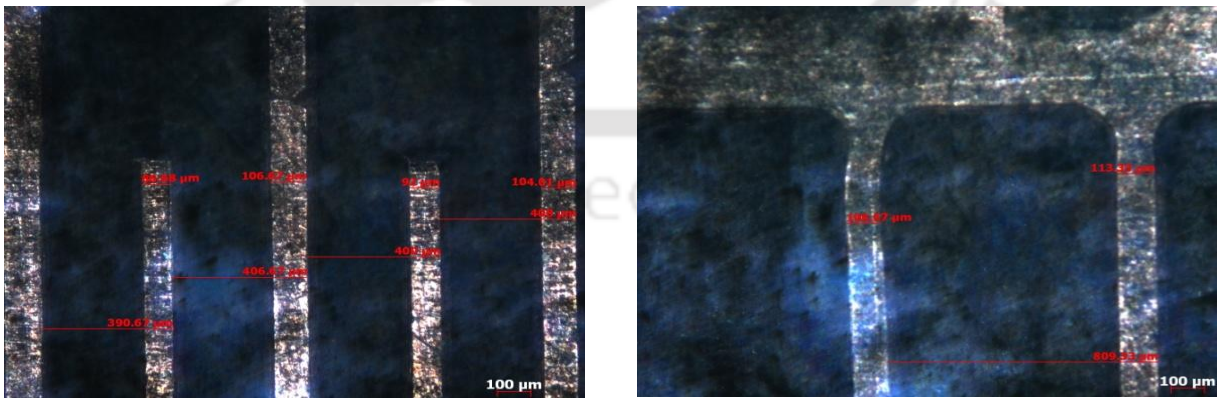

(a) (b)

Figure 5.8. Optical image showing fabricated IDT structure on copper clad FR4, (a) IDT fingers, (b) IDT fingers connected to the lateral electrode.

5.2 Summary

In order to validate the practicability of the proposed SAW devices, the NCIDT SAW devices are fabricated. The NCIDTs are fabricated using UV lithography and LPKF PCB prototyping machine. NCIDTS for high frequency SAW devices are fabricated on Si substrate using UV lithography. The fabrication processes and designs are presented. NCIDTs for low frequency SAW devices are fabricated on copper clad FR4 sheets using LPKF PCB prototyping machine. The fabrication process and designs made for LPKF PCB prototyping machine are presented. The microscopic images of fabricated devices are shown.

6

Measurements and Experiments on Fabricated NCIDT SAW Devices

This chapter of the thesis describes the experiments and measurements carried out on the fabricated SAW devices. The details about the fabrication of the devices are given in chapter 5. The measurements of resonance frequency, output electric potential, and other characteristics of the SAW devices with NCIDT are performed using RF probe station (Cascade Microtech Summit 9000) and network analyzer (Agilent E8361A & Agilent 8753ES), signal generator (Agilent 33120A) and oscilloscope (Yokogawa DL9040). The resonance frequency of the SAW devices with NCIDT fabricated on Si and FR4 is measured from the S_{11} parameter of the device. The output electric potential of a SAW delay line with NCIDT fabricated on FR4 material is measured using the oscilloscope for an input from the signal generator. An application of the proposed devices for mass load sensor is demonstrated.

6.1 S_{11} measurements of fabricated SAW resonator with NCIDT on Si substrate

The fabrication of NCIDT on Si wafer is described in section 5.1.1. The operation of a SAW resonator using the NCIDT is verified in the laboratory. The resonance frequency (f_r) of the SAW device with NCIDT is determined from the S_{11} parameter obtained using RF probe station and network analyzer. The measurement setup is shown in the picture in Figure 6.1. The RF probe station Cascade Microtech Summit 9000 is connected to the network analyzer Agilent E8361A. The RF probe of pitch length of 50 µm is used.

(a) (b)

Figure 6.1 Experimental setup used for measurement showing pictures of (a) RF probes, (b) Probe station with network analyzer.

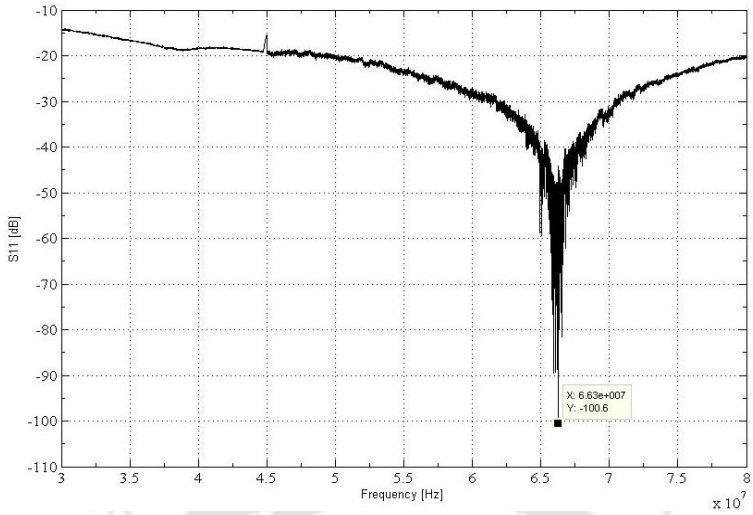

Figure 6.2 S_{11} parameter of the SAW device using NCIDT of λ = 68 µm fabricated on Si and $LiNbO_3$ substrate.

During the measurement of S_{11} parameter, the Y–Z cut $LiNbO_3$ substrate is kept over the NCIDT fabricated on Si with a small air gap. The substrate is made parallel to the surface of probe station since the Y–Z cut $LiNbO_3$ substrate is larger than the Si substrate where NCIDTs are fabricated. Care is taken to avoid fluctuations during the measurement since the NCIDT and the $LiNbO_3$ are not fixed to each others.

Initially, the response of the device without piezo-substrate is measured. The scattering parameter S_{11} is found to be a straight line at 0 dB. Subsequently, the Y–Z cut $LiNbO_3$ substrate is kept over the NCIDT and S_{11} parameter is measured. The response of the device in terms of log magnitude of S_{11} is shown in Figure 6.2. It can be seen from Figure 6.2 the measured resonance frequency of the fabricated device is around 66.3 MHz and has input return loss of -100.6 dB.

6.2 S_{11} measurement of fabricated SAW resonator with NCIDT on copper clad FR4

The S_{11} parameter of SAW device with NCIDT fabricated over the copper clad FR4 sheet using LPKF PCB designer machine is measured using network analyzer (Agilent 8753ES). Measurements of SAW device with NCIDT made on copper clad FR4 material do not required a probe station due to large dimensions of the IDT. The fabricated NCIDTs as shown in Figure

5.8 in Chapter 5 are used for the measurements. This section describes the measurement setup and characteristics of the NCIDT SAW devices where NCIDTs are fabricated on a copper clad FR4 material.

6.2.1 Measurement setup and results

The measurement setup comprises of a metal enclosure coated with Al thin foil, Bayonet Neil connector (BNC) for signal connection, copper wires connecting the NCIDT and BNC inside the enclosure as shown in Figure 6.3a. Though the NCIDT is designed for delay line SAW device, the following experiments on the measurement of S_{11} parameter use only one port of the device.

The NCIDT is kept above the Y–Z cut $LiNbO_3$ wafer aligned to the direction of the wafer cut. Figure 6.3b shows the screen shot of the scattering parameter S_{11} obtained on the network analyzer. The plot of S_{11} in Figure 6.4 shows that the resonance frequency of the device is 4.392 MHz with return loss of –11.018 dB at the resonance frequency. In the proposed SAW device configuration, the NCIDT can be detached from the surface of the piezo-substrate.

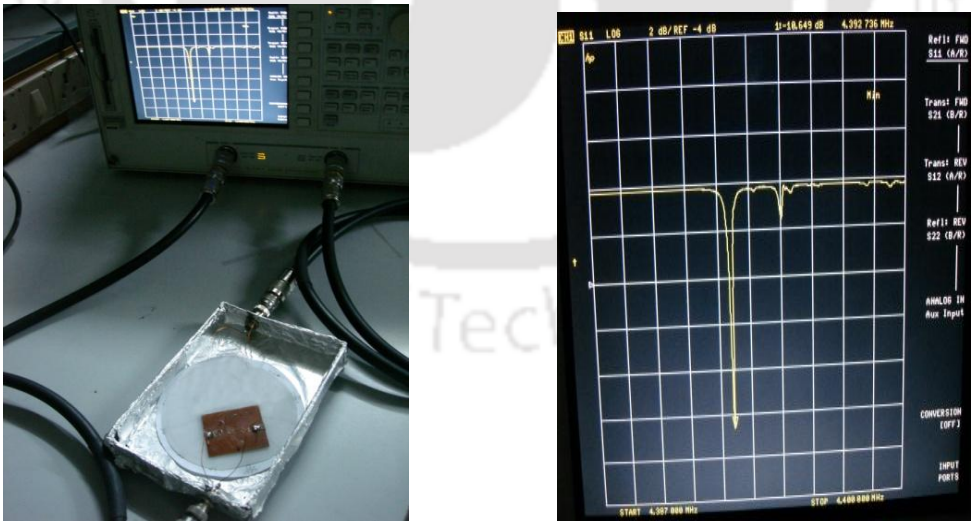

(a) (b)

Figure 6.3 (a) Measurement setup for SAW device with NCIDT fabricated on the copper clad FR4 material. (b) Screen shot of the network analyzer showing S_{11} parameter.

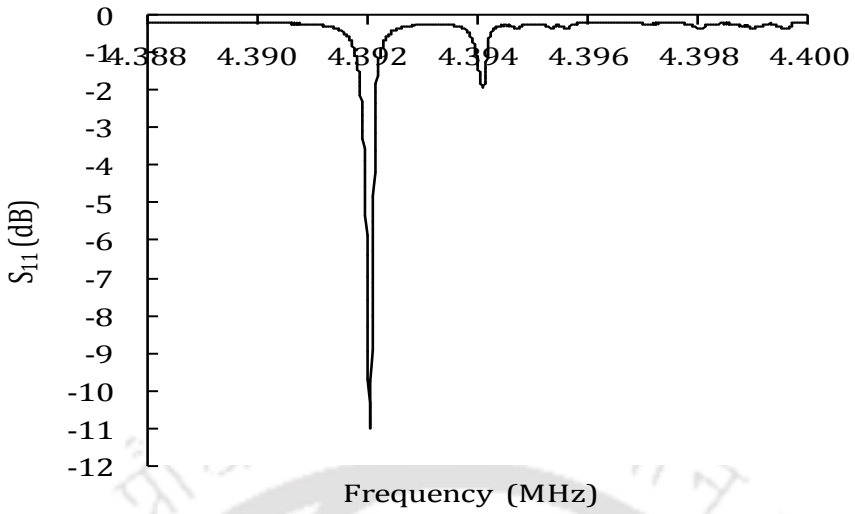

Figure 6.4 Plot of scattering parameter S_{11} for the SAW device with NCIDT fabricated on copper clad FR4 sheet.

6.3 Non-ideal situations in the proposed SAW device

The following non-ideal situations in the proposed SAW devices are studied experimentally. The effects of the change in separation between NCIDT and piezo-substrate, tilt between NCIDT and piezo-substrate, and change in orientation of NCIDT with respect to the piezo-substrate are analyzed by measuring the resonance frequency from S_{11} parameter using network analyzer. The experimental study of these effects is described below.

6.3.1 Effect of change in separation

The effect of separation between NCIDT and the piezo-substrate on the resonance frequency of a one port SAW resonator is studied experimentally by separating NCIDT from the piezo-substrate with a uniform known gap. The separation between NCIDT and the piezo-substrate is maintained by using stacks of pieces of transparency (OHP sheet) used in overhead projectors (OHP). The nominal thickness of transparency is 100 μm. The pictorial representation of the device is shown in Figure 6.5. The separation between NCIDT and the surface of the piezo-substrate is varied from 0.1 mm to 1.0 mm in steps of 0.1 mm. The measurement setup is shown in Figure 6.3a. The scattering parameter S_{11} is measured using the network analyzer. The plots of S_{11} obtained from the network analyzer are shown overlapped in Figure 6.6. The resonance frequency and the corresponding value of S_{11} are tabulated in Table 6.1.

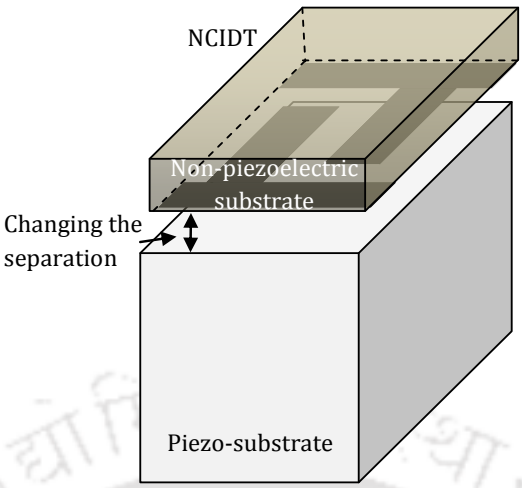

Figure 6.5 Pictorial representation showing the separation between NCIDT and the piezo-substrate.

As the separation between NCIDT and the surface of piezo-substrate increases, the coupling strength decreases [3], [67] and the reflection coefficient S_{11} changes from – 9.142 dB to – 3.167 dB for separation of 0.1 mm to 1.0 mm. The resonance frequency changes from 4.393

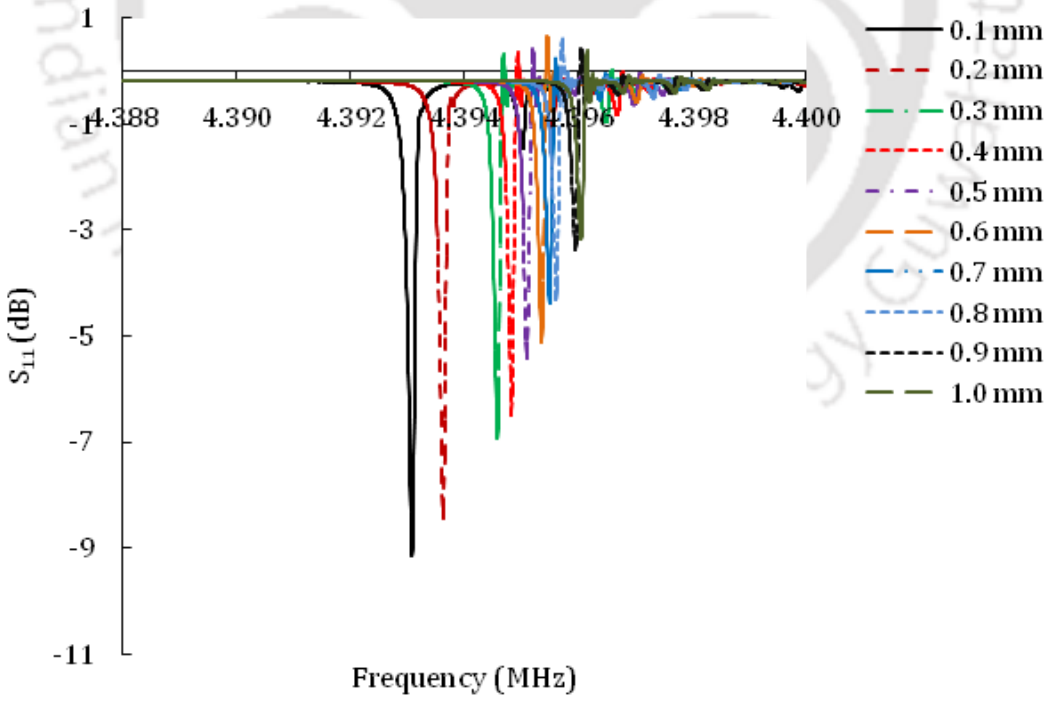

Figure 6.6 Plots of scattering parameter S_{11} for various values of separation between NCIDT and the piezo-substrate.

TABLE 6.1
RESONANCE FREQUENCY AND S_{11} AT VARIOUS VALUES OF SEPARATION BETWEEN NCIDT AND PIEZO-SUBSTRATE

Separation (mm)	Scattering parameter S_{11} (dB)	Resonance frequency (MHz)
0.1	-9.14	4.393085
0.2	-8.44	4.393633
0.3	-6.92	4.394585
0.4	-6.48	4.394833
0.5	-5.42	4.395103
0.6	-5.11	4.395358
0.7	-4.39	4.395500
0.8	-4.32	4.395620
0.9	-3.36	4.395950
1.0	-3.17	4.396055

MHz to 4.396 MHz (change of about 0.07%) for separation of 0.1 mm to 1.0 mm. The main reason for the slight increase in frequency is due to the decrease in effective permittivity as the separation increases.

More detailed analysis is carried out in simulation using FEM and the simulation results are given in section 6.5.

6.3.2 Effect of tilt between NCIDT and piezo-substrate

The effect of tilt between NCIDT and piezo-substrate is analyzed by observing the change in the resonance frequency of the proposed SAW resonator. The resonance frequency of the proposed device is measured from the scattering parameter S_{11} using the network analyzer. We have investigated the effects for tilt in two ways. In the first case, the NCIDT is tilted with the axis of rotation in the direction of wave propagation (Figure 6.7(a)). The tilt between NCIDT and piezo-substrate is made by placing stack of OFC sheets between of NCIDT and piezo-substrate on one side. The tilt angle is calculated from the stack height and the distance of the stack from the axis of rotation and taking tan-inverse of their ratio. For the stack height ranging from 0.1 mm to 1 mm, the tilt angle is found to vary from 0.145^0 to 1.447°. The table

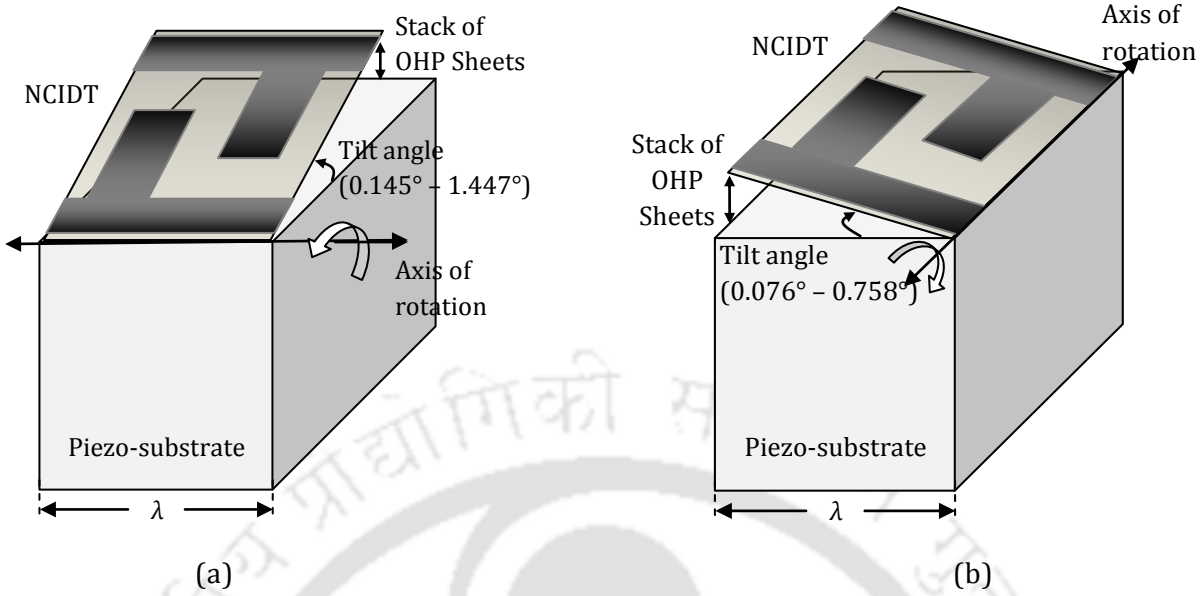

Figure 6.7 Pictorial representation showing tilting of NCIDT for axis of rotation (a) in the direction of wave propagation, (b) normal to the direction of wave propagation.

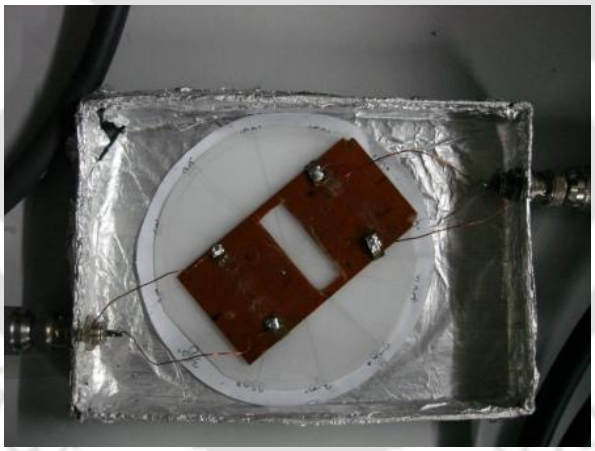

Figure 6.8 Photograph of the measurement setup used to analyze the effect of tilt on the device characteristics.

of resonance frequency and S_{11} at various tilt angles is given in Table 6.2. In the second case, the NCIDT is tilted with the axis of rotation normal to the direction of wave propagation (Figure 6.7(b)) and the tilt angle varies from 0.076° to 0.758°.

TABLE 6.2

RESONANCE FREQUENCY AND S_{11} AT VARIOUS TILT ANGLES BETWEEN NCIDT AND THE PIEZO-SUBSTRATE: THE FIRST CASE

Tilt angle (degree)	Scattering parameter S_{11} (dB)	Resonance frequency (MHz)	Deviation in resonance frequency (kHz)
0	–11.02	4.392043	0
0.145	–9.71	4.392935	0.892
0.289	–9.33	4.393445	1.402
0.434	–8.65	4.393903	1.860
0.579	–7.84	4.394188	2.145
0.723	–7.34	4.394435	2.392
0.868	–6.55	4.394705	2.662
1.013	–6.33	4.394810	2.767
1.158	–5.13	4.394975	2.932
1.302	–4.79	4.395148	3.105
1.447	–4.06	4.395215	3.172

TABLE 6.3

RESONANCE FREQUENCY AND S_{11} AT VARIOUS TILT ANGLES BETWEEN NCIDT AND PIEZO-SUBSTRATE: THE SECOND CASE

Tilt angle (degree)	Scattering parameter S_{11} (dB)	Resonance frequency (MHz)	Deviation in resonance frequency (kHz)
0	–11.02	4.392043	0
0.076	–11.78	4.392168	0.125
0.152	–11.29	4.392736	0.693
0.227	–9.76	4.393297	1.254
0.303	–8.39	4.393654	1.611
0.379	–7.44	4.394053	2.010
0.455	–6.89	4.394402	2.359
0.531	–6.22	4.394727	2.684
0.606	–5.55	4.395003	2.960
0.682	–5.04	4.395255	3.212
0.758	–4.80	4.395336	3.293

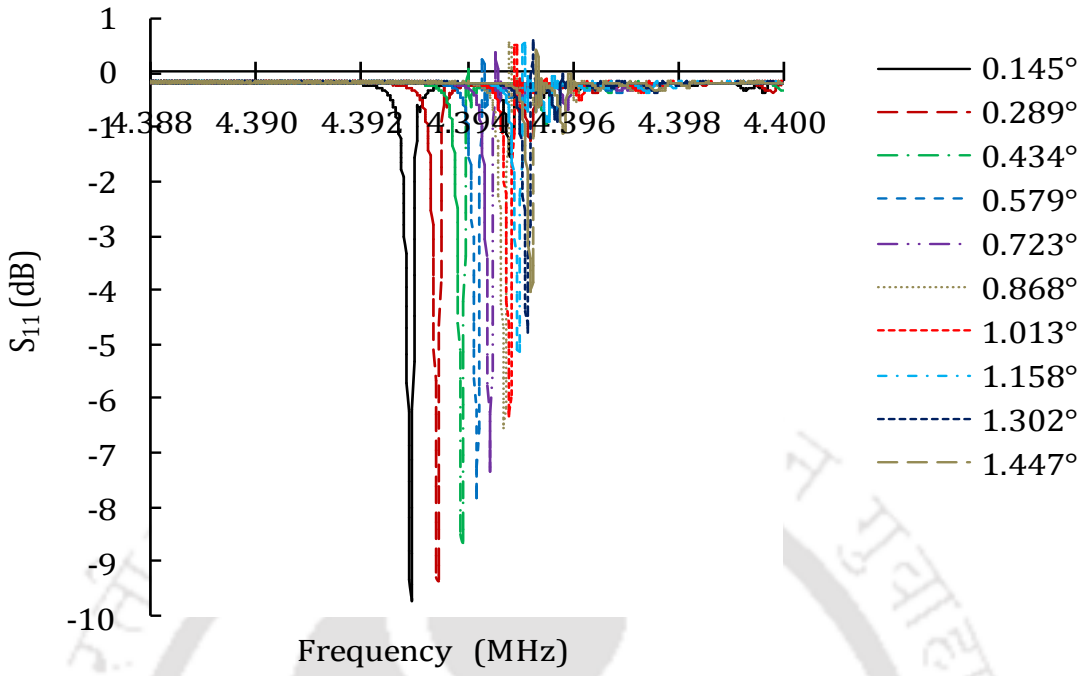

Figure 6.9 Scattering parameter S_{11} at various tilt angles between NCIDT and the piezo-substrate: The first case.

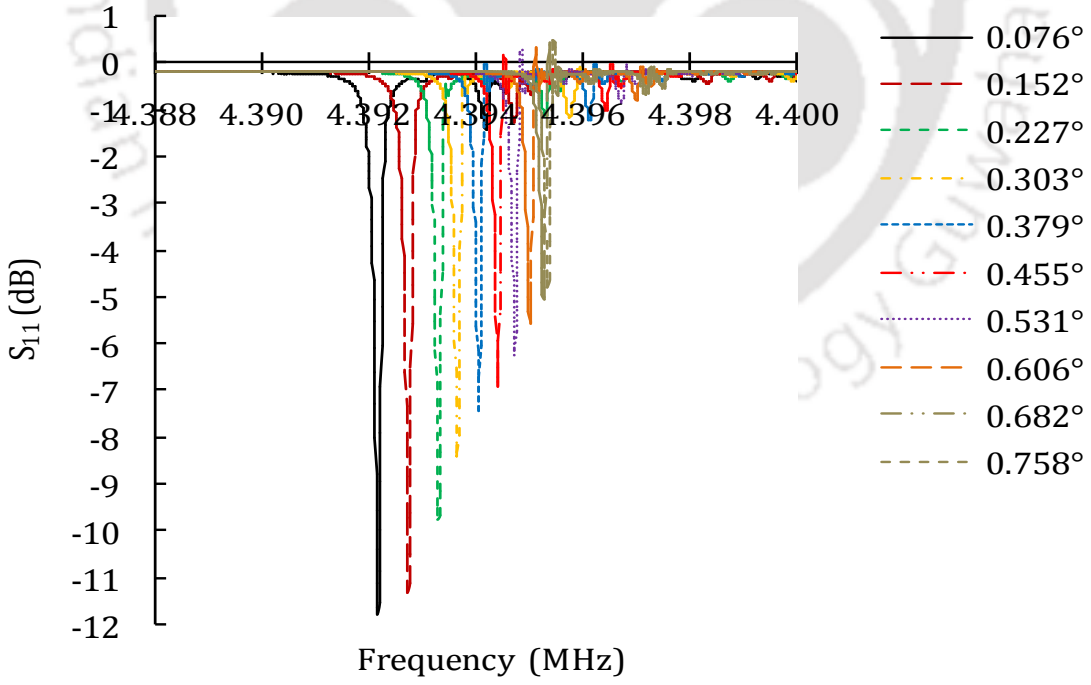

Figure 6.10 Scattering parameter S_{11} at various tilt angles between NCIDT and the piezo-substrate: The second case.

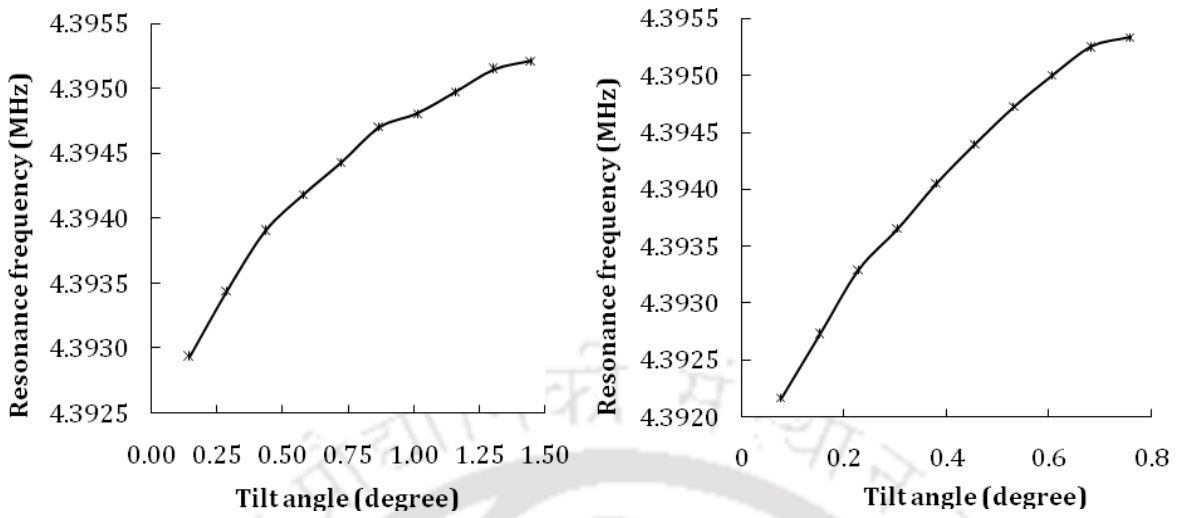

Figure 6.11 Change in resonance frequency versus various tilt angles between NCIDT and piezo-substrate for (a) the first case, and (b) the second case.

The table of resonance frequency and S_{11} at various tilt angles is given in Table 6.3. The measurement setup for studying the tilt effects on the device characteristics is shown in Figure 6.8. The plots of S_{11} parameter for various tilt angles for the two cases are given in Figures 6.9 and 6.10. From Tables 6.2 and 6.3, it is observed that the deviations in the device resonance frequency caused by tilt are small about 0.07% over the range of tilt angles under study. The main reason for the deviation in the resonance frequency is due to the change in effective permittivity with the tilt angle. The plot of resonance frequency versus tile angle for the first case is shown in Figure 6.11 (a) and for the second case is shown in Figure 6.11 (b).

6.3.3 Effect of orientation between NCIDT and piezo-substrate

The effect of relative orientation between NCIDT and piezo-substrate is analyzed by observing the change in the resonance frequency of the proposed resonator device. The resonance frequency of the proposed device is obtained from the scattering parameter S_{11} using the network analyzer. The pictorial representation of the device to study the effect of orientation is shown in Figure 6.12. The measurement setup for studying the effect of orientation of NCIDT with respect to the piezo-substrate is shown in Figure 6.8.

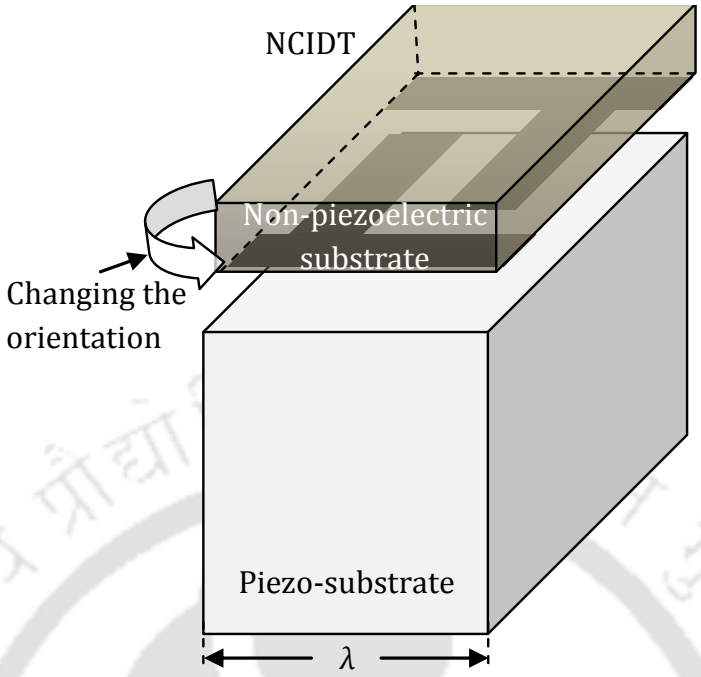

Figure 6.12 Pictorial representation showing relative orientation between NCIDT and the piezo-substrate.

TABLE 6.4

RESULTS OF EXPERIMENT ON ORIENTATION BETWEEN NCIDT AND PIEZO-SUBSTRATE

Relative Orientation (°)	Resonance frequency (MHz)	Deviation (kHz)
0	4.392043	0
1	4.392101	-0.058
2	4.391978	0.065
3	4.391895	0.148
4	4.391779	0.264
5	4.391774	0.269
10	4.391548	0.495
15	4.391348	0.695
20	4.391450	0.593
25	4.391004	1.039
30	4.391231	0.812

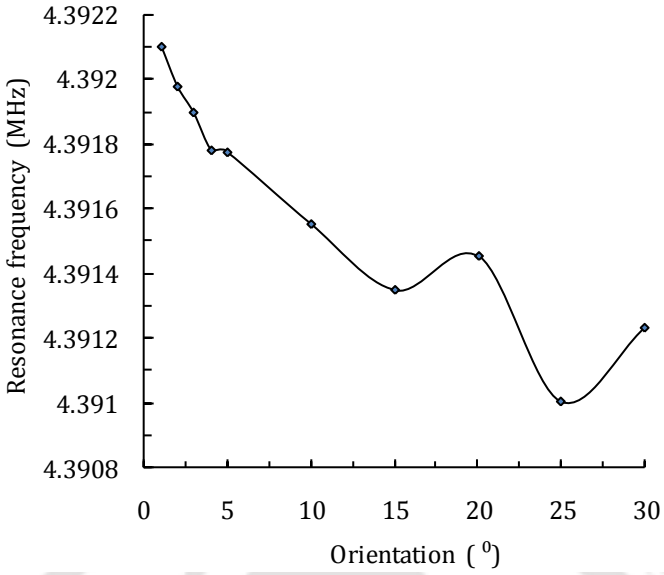

Figure 6.13 Resonance frequency versus relative orientation between NCIDT and the piezo-substrate.

To facilitate the measurement of relative orientation between NCIDT and the piezo-substrate, a plane paper with angles marked is kept under the semi-transparent piezo-substrate and the direction of wave propagation is marked on the top surface of the NCIDT as shown in Figure 6.8. The resonance frequency is measured from the S_{11} parameter at various relative orientations between NCIDT and the piezo-substrate. The values of resonance frequency and the angle of relative orientation are given in Table 6.4. It is observed that the variation in the resonance frequency is within 1 kHz (about 0.02%). The plot of resonance frequency versus relative orientation is shown in Figure 6.13. The decrease in resonance frequency is due to decrease in velocity as orientation angle increases [67].

6.4 Experiments on fabricated NCIDT SAW delay line device

This section describes the measurements carried out on the SAW delay line device using NCIDT. The measurement setup is shown in Figure 6.14. The NCIDT delay line of 22λ (17.600 mm) is used for the experiments. The NCIDT is kept above the Y–Z cut $LiNbO_3$ with a separation of 0.1 mm. The separation of 0.1 mm is achieved by placing pieces of OHP sheet between NCIDT and the piezo-substrate as described in section 6.3. A sinusoidal input of 20 V peak-to-peak amplitude is applied to the transmitting NCIDT using signal generator (Agilent 33120A) and output electric potential of the device is measured at the receiving NCIDT using digital storage oscilloscope (Yokogawa DL9040).

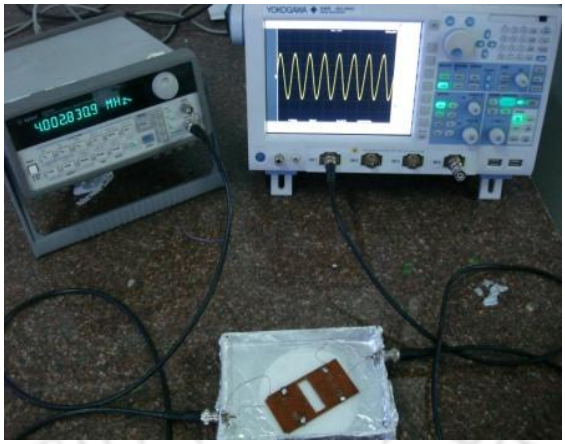

Figure 6.14 Measurement setup to test NCIDT SAW delay line device consists of signal generator, oscilloscope, and shielded enclosure with BNC for holding the device.

The frequency response of the device is plotted in Figure 6.15. The maximum sinusoidal output voltage of 2.55 V peak-to-peak is observed at 4.39188 MHz. From Figure 6.15, the maximum output potential occurs at the resonance frequency of 4.39188 MHz and the plot shows the bandwidth of about 0.3 kHz.

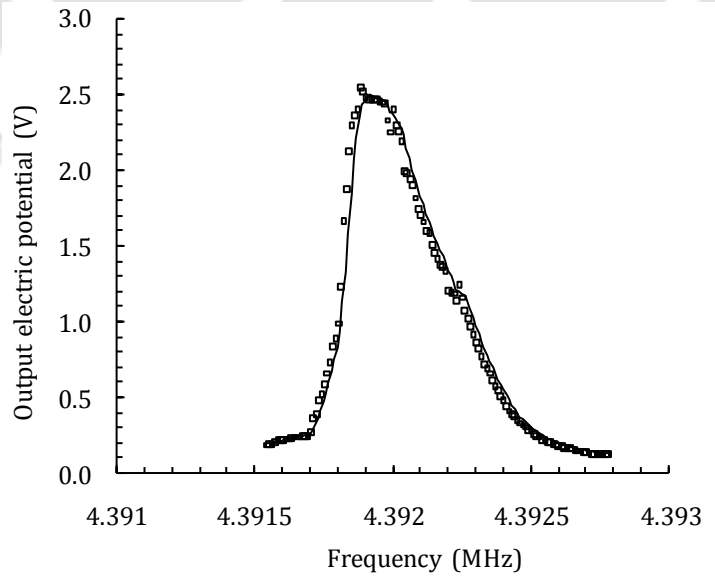

Figure 6.15 Plot of output electric potential versus frequency.

6.5 Simulation of fabricated devices

The simulations are carried out for the devices used in the experiments so that the measurement results are verified and more detailed analysis would be possible. The simulation is done mainly to study the variation in the resonance frequency as a function of separation between NCIDT and the piezo-substrate. COMSOL Multiphysics is used for the simulation.

6.5.1 Simulation methodology

The dimensions of the devices used for FEM based simulation are obtained by measuring the dimensions of the fabricated NCIDT using optical microscope. The average of 25 measurements of the fingers dimension within NCIDT is used for simulation since the finger dimensions of fabricated NCIDT are not uniform. The dimensions used for simulations are as follows: finger width (d) 108.21 µm, finger pitch (p) 401.11 µm (λ/2), finger thickness (h_e) 39 µm, thickness of the piezo-substrate 500 µm, thickness of metal plate below the piezo-substrate approximated to 500 µm, air-gap (h_a) 100 µm, and thickness of holding substrate 1000 µm. Ten pairs of NCIDT fingers are used for simulation. Y–Z cut $LiNbO_3$ piezo-substrate is used and its elastic constants, permittivity constants, stress constants are given in Appendix C. FR4 material is used as the holding substrate for NCIDT. Aluminium plate is placed at the bottom of the piezo-substrate and copper is used for NCIDT electrodes. The material properties of Y–Z cut $LiNbO_3$ are given in Appendix C. The material properties of FR4, aluminium, and copper are used from the materials library in COMSOL Multiphysics. The displacement constraints are set free except for the bottom surface of the piezo-substrate.

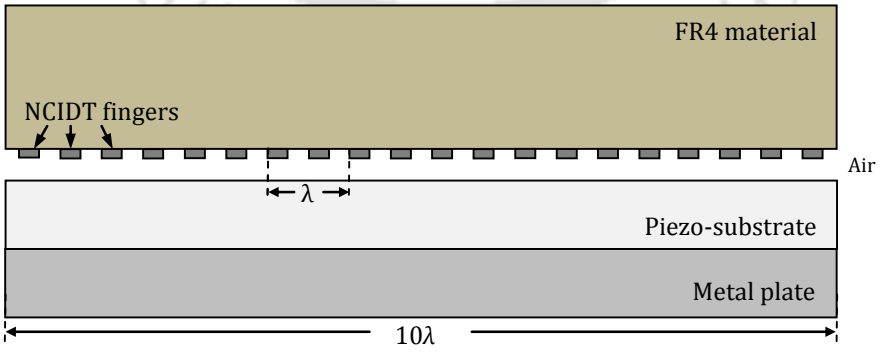

Figure 6.16 2D geometry of SAW resonator with finite number of fingers in NCIDT used for simulation.

The bottom surface is fixed. The interior boundary between piezo-substrate and bottom plate is kept at ground potential. 2D simulation is performed with piezo plane strain conditions as explained in chapter 3. The 2D geometry used for simulation is shown in Figure 6.16. The infinite number of NCIDT fingers, as discussed in chapter 3, can be modeled using periodic boundary condition at both sides of the substrate to reduce computation cost. However, to simulate the practical device, finite number of NCIDT fingers are used. As explained in chapter 3, the optimized mesh density with triangular mesh is applied to the model. Eigenmode analysis is performed to find the resonance frequency of the NCIDT SAW resonator with finite number of fingers.

6.5.2 Results and discussions

The calculation of eigenmode frequency using FEM is performed by zero driven voltage at the NCIDT electrodes. The fabricated NCIDT consists of total 50 pairs of NCIDT fingers. Due to limitation on the simulation resources, less number of fingers are used in the simulation. A study is carried out to know the effect of number of fingers on the resonance frequency. Table 6.5 lists resonance frequency against number of finger pairs. It shows that as the number of finger pairs is increased the resonance frequency will decrease and approach the experimental value of 4.393 MHz.

TABLE 6.5
NUMBER OF IDT FINGER PAIRS AND CORRESPONDING RESONANCE FREQUENCY OBTAINED BY SIMULATION

Number of finger pairs	Resonance frequency (MHz)
5	4.644861
8	4.502592
10	4.471853
12	4.465718

6.5.3 Simulation of effect of separation

The separation between the NCIDT and piezo-substrate is varied and the resonance frequency is determined using COMSOL Multiphysics. Table 6.6 shows the resonance frequency obtained in the experiments and in the simulation for values of separations between NCIDT and the piezo-substrate ranging from 0.1 mm to 2.0 mm. The experimental values are obtained for a fabricated device and the results of simulation are obtained for the actual dimensions of the fabricated device. From Table 6.6, we can see that the simulation results are close to experimental results.

TABLE 6.6
COMPARISON BETWEEN EXPERIMENTAL RESULTS AND SIMULATION RESULTS

Separation (mm)	Resonance frequency (MHz)		
	Experimental	Simulated	Deviation
0.1	4.393085	4.472097	0.079012
0.2	4.393633	4.472893	0.079260
0.3	4.394585	4.473131	0.078546
0.4	4.394833	4.473230	0.078397
0.5	4.395103	4.473280	0.078177
0.6	4.395358	4.473308	0.077950
0.7	4.395500	4.473324	0.077824
0.8	4.395620	4.473335	0.077715
0.9	4.395950	4.473341	0.077391
1	4.396055	4.473346	0.077291
1.1	4.396085	4.473349	0.077264
1.2	4.396109	4.473352	0.077243
1.3	4.396116	4.473354	0.077238
1.4	4.396123	4.473355	0.077232
1.5	4.396128	4.473357	0.077229
1.6	4.396131	4.473358	0.077227
1.7	4.396131	4.473359	0.077228
1.8	4.396132	4.473359	0.077227
1.9	4.396132	4.473360	0.077228
2.0	4.396133	4.473361	0.077228

The average frequency deviations between experimental and simulation results is 77.7 kHz, about 1.7%. The small deviation is due to the rough edges of the electrodes [10]. The edges of the electrodes of the NCIDT fabricated on the FR4 material are not perfectly smooth as seen in the optical images shown in Figure 5.8. The simulation in 2D assumes prefect edges of electrodes.

The plots of resonance frequency versus separation for experiment and simulation are shown on Figures 6.17 and 6.18, respectively. The resonance frequency of the device almost saturates after 1 mm separation and the input return loss approaches 0 dB beyond 2 mm. However the change in resonance frequency for separation from 0.1 mm to 1 mm is small, around 3 kHz (0.07 %) in experiment and 2 kHz (0.03 %) in simulation.

6.6 S_{11} measurement of SAW device with electric field coupled bond pads

This section describes operation of a SAW device, described in chapter 4, with external electrodes that couple signal to the bond pads on the SAW device capacitively. The S_{11} parameter of SAW device is measured using network analyzer. Measurements of SAW device with electric field coupled bond pads do not require a probe station due to large dimensions of the external electrodes. The measurement setup is described below.

6.6.1 Measurement setup and results

The measurement setup comprises of a metal enclosure coated with Al thin foil, Bayonet Neil connector (BNC), thin conducting wires connected to the metal plates of external electrode and BNC as shown in Figure 6.19. The device tested is a SAW IF filter at 38.9 MHz used in video applications. The metal cap of the SAW filter is opened and the bonding wires are removed. The external metal plates are made by thin copper foil fixed to a thick insulating double sided tape to avoid direct contact of hands. The metal plates of the external electrode are kept aligned to the bond pads of the IDTs. The BNCs are connected to the network analyzer ports and the scattering parameter S_{11} is measured. Agilent 8753ES network analyzer has the frequency range of 30 kHz to 6 GHz. The plot of S_{11} is shown in Figure 6.20. It can be seen from the Figure 6.20, that the center frequency of the filter is 38.9 MHz which matches with the original device, however the return loss is reduced approximately 10 times.

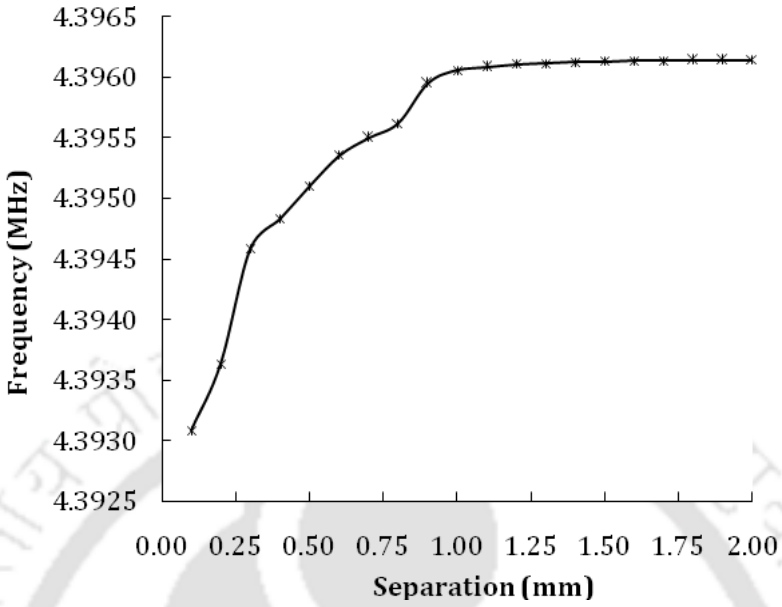

Figure 6.17 Experimental results: Resonance frequency versus separation between NCIDT and the piezo-substrate.

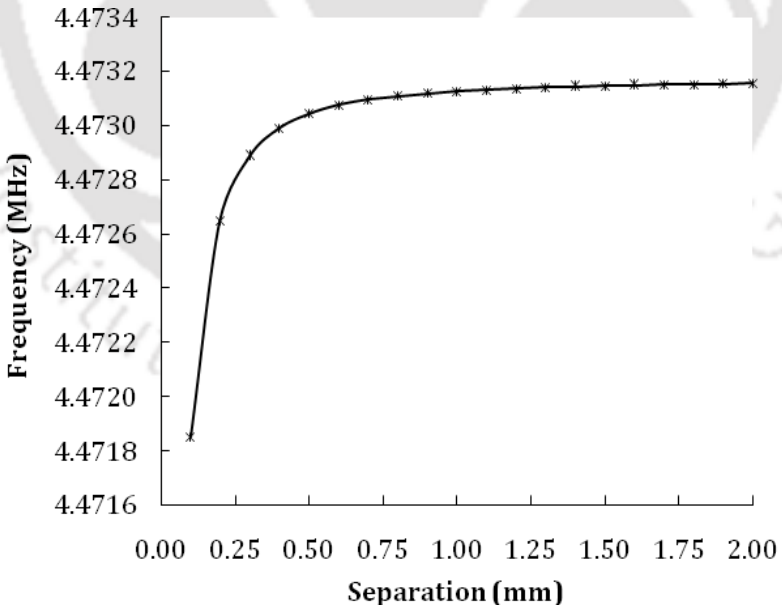

Figure 6.18 Simulation results: Resonance frequency versus separation between NCIDT and the piezo-substrate.

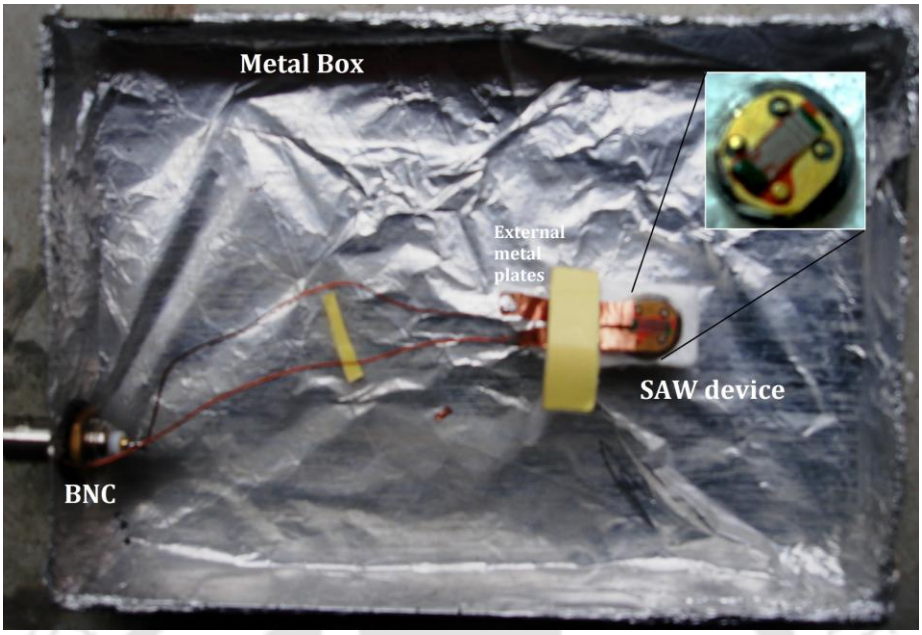

Figure 6.19 Measurement setup for demonstration of a SAW device with electric field coupled bond pads consists of metal enclosure, SAW device, external electrodes and BNC for connection.

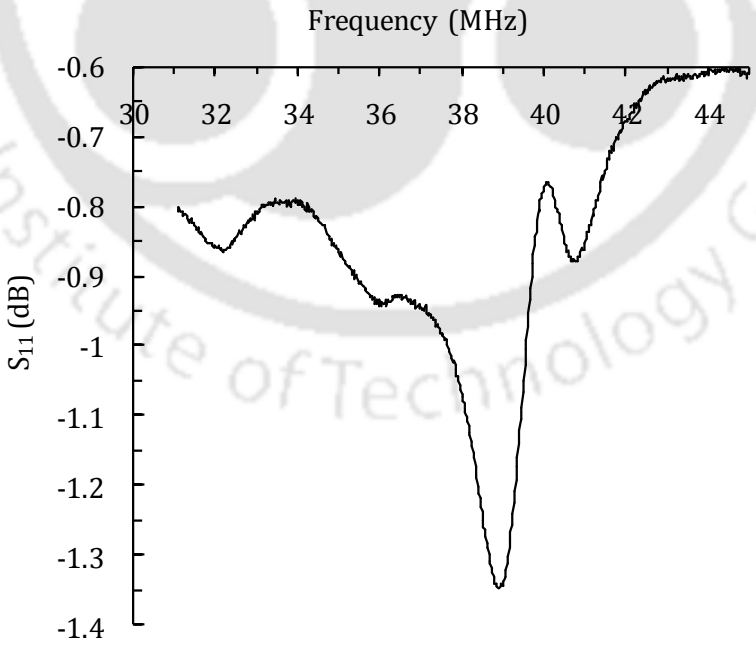

Figure 6.20 Scattering parameter S_{11} of a SAW filter with electric field coupled bond pads.

6.7 Demonstration of SAW sensor using NCIDT

This section describes the application of a SAW resonator with proposed NCIDT configuration as a sensor. A SAW sensor utilizing shear horizontal (SH) SAW for sensing liquid properties is demonstrated. The measurement setup consists of NCIDT fabricated on copper clad FR4 material, 36° rotated Y cut X propagation $LiTaO_3$ (Roditi International, U.K.), shielded metal enclosure.

The measurement setup of the SAW sensor with NCIDT is shown in Figure 6.8. 50 % glycerol solution is prepared. Before each measurement, in 50 µl pure water the glycerol solution is added in steps from 20 µl to 400 µl and the corresponding viscosity and density are calculated [75]. Initially 50 µl pure water is placed on the substrate. The resonance frequency of the SAW resonator is measured from scattering parameters by network analyzer. The addition of glycerol increases the viscosity and density of the solution. The frequency shift of the sensor is measured as the concentration of glycerol solution is increased. Table 6.7 shows the resonance frequency shift against the volume of glycerol solution added in 50 µl water. The plot of frequency shift versus viscosity is shown in Figure 6.21.

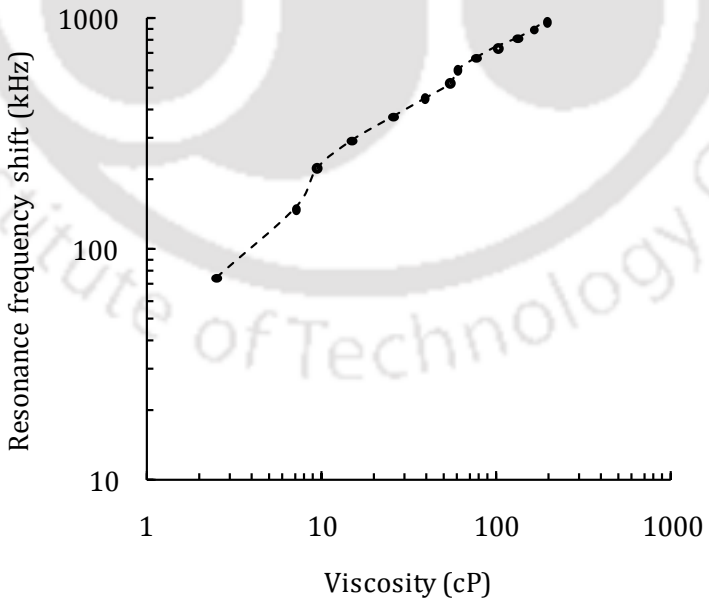

Figure 6.21 Plot of resonance frequency shift versus viscosity of water/glycerol solution.

TABLE 6.7

VOLUME OF GLYCEROL SOLUTION AND CORRESPONDING RESONANCE FREQUENCY SHIFT

Glycerol volume added per 50 µl water (µl)	Resonance frequency shift (kHz)
20	75
50	150
60	225
80	295
110	375
140	450
170	525
180	600
210	675
250	750
300	825
400	900

From Figure 6.21 it is absorbed that the sensitivity of the proposed SAW sensor with NCIDT configuration is around 4 kHz/cP. The sensitivity of the proposed SAW sensor is at least 5 times the SAW sensor reported in [75]. In a recent work [78] a SAW sensor for the detection of H_2S gas using ionic liquid as the sensing medium is reported to have 0.025% sensitivity while the proposed sensor with NCIDT provides 0.09% sensitivity. The absence of static mass load of IDTs is the main reason for the increase in sensitivity.

6.8 Summary

This chapter describes the experiments carried out on the SAW devices using the fabricated NCIDTs. The fabrication of the NCIDT is presented in chapter 5. The fabricated devices are kept over piezo-substrate with small air gap and their characteristics are determined from the S_{11} parameters using network analyzer. The NCIDTs for high frequency SAW devices is fabricated on Si using photolithography owing to small dimensions. The device has to be

connected using RF probe station and the network analyzer is employed to record S_{11} parameters. For an NCIDT of wavelength of 68 μm used with $LiNbO_3$ substrate, the resonance frequency of the fabricated device is around 66.3 MHz and has input return loss of −100.6 dB. The low frequency NCIDTs are fabricated on copper clad FR4 sheets using LPKF PCB prototyping machine. For an NCIDT of wavelength of 800 μm used with $LiNbO_3$ substrate, the resonance frequency of the SAW device is 4.392 MHz with return loss of −11.018 dB.

Since the NCIDT and piezo-substrate are separated by a small air gap, possible non-ideal situations such as change in separation, orientation and tilt between NCIDT and the piezo-substrate are experimentally studied. For a change in the separation between NCIDT and the piezo-substrate from 0.1 mm to 1.0 mm the change in resonance frequency is found to be about 0.07% which is mainly due to the change in effective permittivity. The reflection coefficient S_{11} changes from −9.1 dB to −3.2 dB as the coupling decreases due to increase in separation from 0.1 mm to 1.0 mm. The tilt between the planes of NCIDT and piezo-substrate is studied for two cases. The change in resonance frequency is within 0.07% for tilt of up to 1.5° when the axis of rotation is along the direction of SAW propagation and for tilt of up to 0.8° when the axis of rotation is perpendicular to the direction of SAW propagation. This small change in resonance frequency is mainly due to change in effective permittivity. In another experiment with changing relative orientation between NCIDT and the piezo-substrate, the variation in the resonance frequency is about 0.02%.

Another device tested experimentally is a SAW device with NCIDT delay line. A sinusoidal 20 V peak-to-peak voltage applied to the input port of NCIDT from a signal generator and the output at the other port is measured in an oscilloscope and the frequency response is plotted. The maximum amplitude of 2.55 V is observed at 4.39188 MHz and it has a bandwidth of about 0.3 kHz.

For verification and additional analysis of the fabricated devices, simulations are carried out for devices having the actual dimensions of the fabricated devices measured through an optical microscope. The fabricated NCIDT consists of total 50 pairs of NCIDT fingers. To limit the computational cost of simulation, the number of fingers is reduced to 10 pairs in the simulation. However by performing simulation for varying number of fingers, it is observed that increasing in number of NCIDT fingers would approach the resonance frequency towards the practical value. Simulation is carried out to study the effect of separation between NCIDT

and the piezo-substrate ranging from 0.1 mm to 2.0 mm and the average frequency deviation between experimental and simulation results is 77.7 kHz, about 1.7%.

The second type of proposed SAW device with electric field coupled bond pads is experimentally tested. A commercial SAW filter used as IF filter in video applications is used with external electrodes coupled capacitively to the bond pads present in the device. Though the center frequency of the device matches, the return loss is about 10 times lower.

Finally an application of the NCIDT SAW resonator as a mass load sensor is demonstrated. The glycerol/water solution of varying concentration of glycerol is added on the piezo-substrate and change in resonance frequency is noted. The sensitivity of the proposed SAW sensor with NCIDT configurations of about 4 kHz/cP is observed. The sensitivity of the proposed SAW sensor is at least 5 times a conventional SAW sensor. The absence of static mass load of IDTs is the main reason for the increase in sensitivity.

7

Conclusions and Recommendations

7.1 Conclusions

The main work investigated in the thesis is about the analysis of a non-contact arrangement of IDT (NCIDT) where IDTs are fabricated on a non-piezoelectric substrate kept above facing the piezo-substrate with a small air gap, and the electric field between NCIDT and the piezo-substrate is coupled through an air gap. As the piezo-substrate is void of IDTs, the secondary effects due to presence of metallic IDT over the piezo-substrate are either eliminated or greatly reduced. For sensor applications, the proposed configuration provides entire piezo-substrate for sensing, in addition to the convenience of easy cleaning or coating of sensing film due to the absence of bonding wires. The simulation of proposed SAW device based on FEM shows that accuracy in designed resonance frequency is high than the conventional SAW device. The sensor made with proposed SAW device provides higher sensitivity than the sensor made with conventional SAW device.

The important contributions by the thesis are as follows.

- Simulations of conventional SAW devices such as one port SAW resonators and SAW delay line device based on FEM are performed to compare the results with proposed SAW devices. In one port SAW resonator the various parameters such as admittance, resonance frequency, total displacement, quality factors, and capacitance ratio are calculated. The simulation of the conventional SAW resonator with finite width of aperture is performed and admittance value is calculated. In SAW delay line device the output potential and delay is extracted by simulation. The secondary effects such as mass loading, electrical loading, and BAW generation due to presence of metallic IDt over the surface of the piezo-substrate are demonstrated. The various parameters such as dispersion of SAW phase velocity, reflection coefficient per period of IDT fingers, and effective electromechanical coupling coefficient is calculated for various metallization ratios of the IDT electrodes. The above analysis and simulations are done to compare the outcomes with the proposed SAW device with NCIDT.

- Two SAW devices are proposed: 1. SAW devices with non-contact interdigital transducer (NCIDT) and 2. SAW devices with electric field coupled bond pads. The first proposed SAW device comprises of piezo-substrate and NCIDT patterned on non-piezoelectric substrate. The NCDIT is kept above facing to the piezo-substrate with

small air gap comparable to SAW wavelength. The second proposed SAW device comprises of piezo-substrate and IDTs fabricated on the piezo-substrate, and external metal plates placed over the bond pads with or without air gap.

- The analysis of the first proposed SAW device with NCIDT is performed by simulation based on FEM. The theory and operation of the proposed NCIDT SAW device is presented. The SAW device with NCIDT such as one port SAW resonators and SAW delay line device based on FEM are performed and results are compared with conventional SAW devices. In one port SAW resonator the various parameters such as admittance, resonance frequency, total displacement, transduction coefficient, quality factors, and capacitance ratio are calculated. With reference to free surface resonance frequency f_0, the resonance frequency of the conventional SAW resonator is 4.4895 MHz lower, whereas the resonance frequency of NCIDT SAW resonator is remarkably close, 6.34 kHz lower. The capacitance ratio for the NCIDT SAW resonator is 112390 which is about 4000 times the capacitance ratio of the conventional SAW resonator. However, the excitation efficiency and quality factor at resonance frequency in NCIDT resonator is about 4 orders lower and 40 % less than the conventional resonator. The simulation of the proposed SAW resonator with finite width of aperture is performed and admittance value is calculated. In SAW delay line device the output potential and delay is extracted by simulation. The delay time of the conventional SAW delay line device is 0.6 ns less, whereas the delay time of the proposed NCIDT SAW delay line device is equal to theoretically calculated delay time. The various aspects of the proposed NCIDT SAW device such as effects of holding substrate, different material for holding substrate, with and without holding substrate, and effects of air gap between NCIDt and piezo-substrate on SAW phase velocity are presented. The device parameters such as dispersion in SAW phase velocity, electromechanical coupling coefficient, and reflection coefficient as a function of air gap have been plotted. The secondary effects such as mass loading, electrical loading, and BAW generation due to NCIDT are demonstrated and the results are compared with the secondary effects of conventional SAW device. Two types of SAW sensors have been presented. one is direct mass load and second is sensor with sensing film. It is observed from the simulation results that the sensitivity of SAW sensors with proposed NCIDT structure is greater than the sensitivity of the conventional SAW sensors.

- The second proposed SAW device with electric field bond pads is presented by simulation based on FEM. A one port SAW resonator with proposed electric field coupled bond pads configuration is simulated. The simulation is performed with finite aperture width. The device parameters such as transduction coefficient, quality factor and capacitance ratio is calculated and these parameters are compared with identical conventional SAW resonator.

- The design and fabrication of SAW devices with NCIDT configurations is performed. The high frequency NCIDT is fabricated on Si substrate using UV photolithography and low frequency NCIDT is fabricated on copper clad FR4 material using LPKF PCB prototyping machine.

- Further, the experiments of both proposed SAW device, SAW device with NCIDT and SAW device with electric field of fabricated is performed. The S_{11} parameter of the SAW device with NCIDT fabricated on the Si substrate is measured using RF-probe station and network analyzer due to small dimension of bond pads and IDT. The S_{11} parameter of the SAW device with NCIDT fabricated on the copper clad FR4 material is measured using network analyzer without RF-probe station due to large dimensions of the IDT. Various non-ideal situations such as effects of separation between NCIDT and piezo-substrate, effects of tilt, and effects of orientations of the proposed SAW device with NCIDT fabricated on copper clad FR4 material are demonstrated. The separation is made by placing stack of OFC sheets between of NCIDT and piezo-substrate. For a stack height ranging from 0.1 mm to 1 mm, the tilt angle is found to vary from 0.145° to 1.447°. The S_{11} parameter is measured and change in resonance frequency is observed. The change in resonance frequency of 4.392 MHz device for non-ideal situations is around 4 kHz. The SAW delay line experiment with NCIDT is performed and the resonance frequency and change in output electric potential with frequency is plotted. The identical dimensions of fabricated SAW device are simulated and the results are compared. In addition the effects of separations between NCIDT and piezo-substrate on resonance frequency are demonstrated by simulation based on FEM using COMSOL Multiphysics. The maximum and minimum frequency deviations between experimental and simulation results are around 79.01 kHz and 77.22 kHz, respectively.

7.2 Recommendation for future work

The present work introduces a technique for the development of a new class of SAW device with high accuracy in designed frequency. In addition, the highly sensitive sensors can be developed.

This research work can be extended in the following directions:

- The high frequency SAW device can be developed without resistive loss unlikely in conventional SAW devices.
- The other techniques for increasing the coupling between NCIDT and piezo-substrate with non-contact configuration can be suggested.
- The proposed SAW device can be integrated with electronic circuitry, which would make the device compact.
- The planner antenna along with NCIDT to make wireless SAW devices application can be suggested.
- The device has potential application in sensing fields. Various types of gas sensor can be proposed.
- Since the IDTs are eliminated from the piezo-substrate, the proposed SAW device can be useful in making chemical sensor without insulation layer in the device substrate.
- The end effects of the IDTs and bond pads can be studied in case of NCIDT SAW device.

A. Important Substrate Materials Used in SAW Sensor Applications

Piezo-substrate materials used in SAW sensor application are shown in Table A.1 [6], [11], [76].

TABLE A.1

IMPORTANT SUBSTRATE MATERIALS USED IN SAW SENSORS

Substrate	Propagation	K^2 (%)	Acoustic velocity (m/s)
ST- quartz	X	1.89	3158
Y- quartz	X	1.1	3159
Y- $LiNbO_3$	Z	4.5	3488
Y -128° $LiNbO_3$	X	5.3	3992
77.5° Y- $LiTaO_3$	X	1.6	3379
36° Y- $LiTaO_3$	X	5	4160
Langasite	-	3.2	2742
100-011 GaAs	-	0.7	2864
Y-60° CdS	-	-	1702
ZnO	-	-	2639

B. Matrix Technique for Crystal Axes Rotation to given Euler Angles

It is important to rotate the crystal axes according to given Euler angles viz., ϕ, θ, and ψ rotated along x_1, x_2 and x_3 axis and align them with the required Cartesian co-ordinate axes. During such rotations, the stiffness matrix ($\mathbf{C}^E$), piezoelectric matrix (**e**) and dielectric matrix ($\boldsymbol{\varepsilon}$) of the material also gets transformed accordingly. A very efficient matrix technique has been developed for this purpose by W. L. Bond [10]. If the directional vector written as $\vec{r} = (x_1, x_2, x_3)$, then the directional vector written in terms of crystal axes: $\tilde{r}$ may be found using a coordinate transformation matrix **a,** and bond matrix $\mathbf{M_b}$**.** The rotated stiffness ($\tilde{\mathbf{C}}^E$), piezoelectric constant ($\tilde{\mathbf{e}}$), and permittivity matrix ($\tilde{\boldsymbol{\varepsilon}}$) can be obtained using the following equations

$$\tilde{r} = \mathbf{a}.\vec{r}$$

$$\tilde{\mathbf{C}}^{\mathbf{E}} = \mathbf{M}.\, C^E.\mathbf{M}'$$

$$\tilde{\mathbf{e}} = \mathbf{a}.\,\mathbf{e}.\,\mathbf{M}'$$

$$\tilde{\boldsymbol{\varepsilon}} = \mathbf{a}.\,\boldsymbol{\varepsilon}.\,\mathbf{a}$$

where the coordinate transform matrix **a** rotating around x_3, x_2 and x_1 (in the given order)as below

$$\mathbf{a} = \begin{pmatrix} a_{11} & a_{12} & a_{13} \\ a_{21} & a_{22} & a_{23} \\ a_{31} & a_{32} & a_{33} \end{pmatrix}$$

$$= \begin{pmatrix} \cos(\phi)\cos(\theta) & \sin(\phi)\cos(\theta) & -\sin(\theta) \\ \cos(\phi)\cos(\theta)\sin(\psi) - \sin(\phi)\cos(\psi) & \cos(\phi)\cos(\psi) + \sin(\phi)\sin(\theta)\sin(\psi) & \cos(\theta)\sin(\psi) \\ \cos(\phi)\sin(\theta)\cos(\psi) + \sin(\phi)\sin(\psi) & \sin(\phi)\sin(\theta)\cos(\psi) + \cos(\phi)\sin(\psi) & \cos(\theta)\cos(\psi) \end{pmatrix}$$

The bond matrix $\mathbf{M_b}$ is as given below

$$\mathbf{M_b} = \begin{pmatrix} a_{11}^2 & a_{12}^2 & a_{13}^2 & 2a_{12}a_{13} & 2a_{13}a_{12} & 2a_{11}a_{12} \\ a_{21}^2 & a_{22}^2 & a_{23}^2 & 2a_{22}a_{23} & 2a_{23}a_{21} & 2a_{21}a_{22} \\ a_{31}^2 & a_{32}^2 & a_{33}^2 & 2a_{32}a_{33} & 2a_{33}a_{31} & 2a_{31}a_{32} \\ a_{23}a_{31} & a_{22}a_{31} & a_{23}a_{33} & a_{22}a_{11}+a_{23}a_{32} & a_{21}a_{33}+a_{23}a_{31} & a_{22}a_{31}+a_{21}a_{32} \\ a_{23}a_{31} & a_{22}a_{12} & a_{33}a_{13} & a_{12}a_{33}+a_{13}a_{32} & a_{13}a_{31}+a_{11}a_{33} & a_{11}a_{32}+a_{12}a_{21} \\ a_{11}a_{21} & a_{12}a_{22} & a_{13}a_{23} & a_{12}a_{23}+a_{13}a_{22} & a_{13}a_{21}+a_{11}a_{23} & a_{11}a_{22}+a_{12}a_{21} \end{pmatrix}$$

C. Material Constants of Lithium Niobate

Material constants of Lithium Niobate used in the thesis are taken from [42]. The constants for X cut Y - $LiNbO_3$ and Y cut Z- $LiNbO_3$ are given in section C. 1 and C. 2, respectively.

C. 1 Material constants of X-Z cut $LiNbO_3$

Density (ρ) = 4675 kg/m^3

$$\text{Stiffness, } \mathbf{C}^E = \begin{pmatrix} 20.3 & 5.3 & 7.5 & 0.9 & 0 & 0 \\ 5.3 & 20.3 & 7.5 & -0.9 & 0 & 0 \\ 7.5 & 7.5 & 24.5 & 0 & 0 & 0 \\ 0.9 & -0.9 & 0 & 6.0 & 0 & 0 \\ 0 & 0 & 0 & 0 & 6.0 & 0.9 \\ 0 & 0 & 0 & 0 & 0.9 & 7.5 \end{pmatrix} \times 10^{10}\ \text{N/m}^2$$

$$\text{Piezoelectric constant , } \mathbf{e} = \begin{pmatrix} 0.0 & 0.0 & 0.0 & 0.0 & 3.7 & -2.5 \\ -2.5 & 2.5 & 0.0 & 3.7 & 0.0 & 0.0 \\ 0.2 & 0.2 & 1.3 & 0.0 & 0.0 & 0.0 \end{pmatrix} \text{C/m}^2$$

$$\text{Permittivity , } \boldsymbol{\varepsilon} = \begin{pmatrix} 44 & 0 & 0 \\ 0 & 44 & 0 \\ 0 & 0 & 29 \end{pmatrix}$$

C. 2 Material constants of Y-Z cut $LiNbO_3$

Density (ρ) = 4647 kg/m^3

$$\text{Stiffness, } \mathbf{C}^E = \begin{pmatrix} 24.24 & 7.52 & 7.52 & 0 & 0 & 0 \\ 7.52 & 20.3 & 5.73 & 0 & 8.5 & 0 \\ 7.52 & 5.73 & 20.3 & 0 & -8.5 & 0 \\ 0 & 0 & 0 & 7.52 & 0 & 8.5 \\ 0 & 8.5 & -8.5 & 0 & 5.95 & 0 \\ 0 & 0 & 0 & 8.5 & 0 & 5.95 \end{pmatrix} \times 10^{10}\ \text{N/m}^2$$

$$\text{Piezoelectric constant , } \mathbf{e} = \begin{pmatrix} 1.33 & 0.23 & 0.23 & 0 & 0 & 0 \\ 0 & 0 & 0.0 & -2.5 & 0 & 3.7 \\ 0 & -2.5 & 2.5 & 0 & 3.7 & 0 \end{pmatrix} \text{C/m}^2$$

$$\text{Permittivity}, \boldsymbol{\varepsilon} = \begin{pmatrix} 28.7 & 0 & 0 \\ 0 & 85.2 & 0 \\ 0 & 0 & 85.2 \end{pmatrix}$$

D. Absorbing Boundary Conditions

In order to avoid acoustic reflections from the boundaries or edges of the SAW substrate, absorbing boundary conditions are applied in the simulations. The influence of wave reflections from boundaries can be reduced by assuming critical damping along the boundaries [36]. This can be achieved by employing suitable values for Rayleigh damping coefficients in the COMSOL Multiphysics software [15]. In Rayleigh damping model, the Rayleigh damping matrix **Z** is a linear combination of mass matrix and stiffness matrix as given below

$$\xi = A_{dM} M + B_{dk} k$$

where the mass proportional damping parameter (A_{dM}) and stiffness proportional damping parameter (B_{dk}) are damping coefficients and they are related to damping ratio (ξ) as

$$\xi = \frac{A_{dM} + B_{dk}\omega^2}{2\omega}$$

Absorbing boundary can be achieved by assuming critical damping, $\xi = 1$ and $A_{dm} = 0$ then $B_{dk} = 1/\pi f$.

E. Material Properties of PIB Sensing Film and TCE and DCE Organic Vapors

TABLE E.1
PARAMETERS OF SENSING FILM AND ORGANIC VAPORS

Polymer density (ρ_0) (g/cm^3)	Organic vapor density (ρ_v) (g/dm^3)		Partition coefficient (k_p)	
PIB	TCE	DCE	PIB-TCE	PIB-DCE
0.918	5.866	4.328	$10^{2.3994}$	$10^{1.9215}$

Bibliography

[1] C. C. W. Ruppel and T. A. Fieldly, *Advances in Surface Acoustic Wave Technology, Systems and Applications (vol. I)*. Singapore: World Scientific Publishing Co. Pte. Ltd., 2000.

[2] T. Shigematsu, M. K. Kurosawa, and K. Asai, "Nanometer stepping drives of surface acoustic wave motor," *IEEE Transactions on Ultrasonics, Ferroelectronics, and Frequency Control*, vol. 50, no. 4, 2003.

[3] D. Morgan, *Surface Acoustic Wave Filters with Applications to Electronic Communications and Signal Processing*, London, U.K.: Elsevier, 2007.

[4] D. Royer and E. Dieulesaint, *Elastic Waves in Solids II*. New York: Springer–Verlag, 2000.

[5] Y. Q. Fu, X. Y. Du, J. K. Luo, A. J. Flewitt, W. I. Milne, D. S. Lee, N. M. Park, S. Maeng, S. H. Kim, Y. J. Choi, and J. Park, "SAW Streaming in ZnO Surface Acoustic Wave Micromixer and Micropump," *Sensor, 2007 IEEE*, pp. 478–483, 2007.

[6] M. Thompson, *Surface-Launched Acoustic Wave Sensors: Chemical Sensing and Thin Film Characterization*. John Wiley & Sons, 1997.

[7] K. J. Gamble and D. C. Malocha, "Simulation of short LSAW transducers including electrode mass loading and finite finger resistance," *IEEE Transactions on Ultrasonics, Ferroelectronics, and Frequency Control*, vol. 49, no. 1, pp. 47–56, 2002.

[8] M. B. Schulz and J. H. Matsinger, "Rayleigh-wave electromechanical coupling constants," *Applied Physics Letter*, vol. 20, no. 9, pp. 367–369, 1972.

[9] W. S. Jones, C. S. Hartmann, and T. D. Sturdivant, "Modified equivalent circuit model for ultrasonic surface wave interdigital transducers," in 1971 *IEEE-G-MTT Symposium Digest*, pp. 58–59.

[10] B. A. Auld, *Acoustic Fields and Waves in Solids, vol. I*., Florida: Robert E. Krieger Publishing Company, 2 edition, 1990.

[11] J. W. Gardner, V. K. Varadan, and O. O. Awadelkarim, *Microsensors MEMS and Smart Devices*. Chichester, U.K.: John Wiley & Sons, 2002.

[12] D. S. Ballantine, R. M. White, S. I. Martin, A. I. Ricco, E. T. Zellers, G. C. Frye, and H. Wohltjen, *Acoustic Waves Sensors theory, design, and physico–chemical Applications*. New York: Academic Press, 1997.

[13] K. M. Lakin, "Perturbation theory for electromagnetic coupling to elastic surface waves on piezoelectric substrates," *Journal of Applied Physics*, vol. 42, no. 3, pp. 899–906, 1971.

[14] D. Pununuri and K. M. Lakin, "Propagation of surface waves in anisotropic," in *Proceedings of IEEE Ultrasonics Symposium*, 1972, pp. 328–332.

[15] *COMSOL Multiphysics Version 3.4 Documentation*, COMSOL AB, Stockholm, Sweden, 2007.

[16] K. Beck, M. Wohlfahrt, A. Rugemer, S. Reiss, M. von Schickfus, and S. Hunklinger, "Inductively coupled surface acoustic wave device for sensor application," *IEEE Transactions on Ultrasonics, Ferroelectronics, and Frequency Control*, vol. 45, no. 5, pp. 1140–1144, 1998.

[17] G. S. Kino, "Acoustoelectric interactions in acoustic-surface-wave devices," in *Proceedings of the IEEE*, 1976, pp. 724–748.

[18] G. S. Kino, *Acoustic Waves: Devices, Imaging, and Analog Signal Processing*. New Jersey: Prentice-Hall, Inc., 1987.

[19] K. M. Lakin, "Perturbation theory for electromagnetic coupling to elastic surface waves on piezoelectric substrates," *Journal of Applied Physics*, vol. 42, no. 3, pp. 899–906, 1971.

[20] K. A. Ingebrigtsen, "Surface waves in piezoelectrics," *Journal of Applied Physics*, vol. 40, no. 7, pp. 2681–2686, 1969.

[21] K. Eda, Y. Taguchi, K. Onishi, and S. Seki, "Surface acoustic wave device with interdigital transducers formed on a holding substrate thereof and a method of producing the same," United States Patent 5 453 652, Sep. 26, 1995.

[22] K.-Y. Hashimoto, *Surface Acoustic Wave Devices in Telecommunications: Modelling and Simulation*. New York: Springer-Verlag, 2000.

[23] C. C. W. Ruppel and T. A. Fieldly, *Advances in Surface Acoustic Wave Technology, Systems and Applications (vol. II)*. Singapore: World Scientific Publishing Co. Pte. Ltd., 2001.

[24] W. R. Smith, H. M. Gerard, J. H. Collins, T. M. Reeder, and H. J. Shaw, "Analysis of interdigital surface wave transducers by use of an equivalent circuit model," *IEEE Transactions on Microwave Theory and Techniques*, vol. 17, pp. 856–864, 1969.

[25] A. B. Bhattacharyya, S. Tuli, and S. Mazumdar, "Spice simulation of surface acoustic wave interdigital transducers," *IEEE Transactions on Ultrasonics, Ferroelectrics, and Frequency Control*, vol. 42, pp. 784–786, 1995.

[26] V. Plessky and J. Koskela, "Coupling-of-modes analysis of SAW devices," *International Journal of High Speed Electronics and Systems*, vol. 10, pp. 867–947, 2000.

[27] T. T. Wu, S. M. Wang, Y. Y. Chen, T. Y. Wu, P. Z. Chang, L. S. Huang, C. L. Wang, C. W. Wu, and C. K. Lee, "Inversion determination of coupling of modes parameters of surface acoustic wave resonators," *Japanese Journal of Applied Physics*, vol. 41, pp. 6610–6615, 2002.

[28] A. Arnau (Ed.), *Piezoelectric Transducers and Applications*. New York: Springer–Verlag, 2004.

[29] D. Royer and E. Dieulesaint, *Elastic waves in solids I Free and Guided Propagation*. Berlin: Springer-Verlag, 2000.

[30] V. K. Varadan, K. J. Vinoy, and S. Gopalakrishnan, *Smart Material Systems and MEMS: Design and Development Methodologies*, England: John Wiley & Sons, 2007.

[31] T. R. Hsu, *MEMS and Microsystems: Design and Manufacture*, McGraw-Hill Science, 2001.

[32] R. Lerch, "Simulation of piezoelectric devices by two-and-three-dimensional finite elements," *IEEE Transactions on Ultrasonics, Ferroelectrics, and Frequency Control*, vol. 37, pp. 233–247, 1990.

[33] S. Rahman, M. Kataoka, C. H. W. Barnes, and H. P. Langtangen, "Numerical investigation of a piezoelectric surface acoustic wave interaction with a one-dimensional channel," *Physical Review B*, vol. 74, 035308, 2006.

[34] M. Z. Atashbar, B. J. Bazuin, M. Simpeh, and S. Krishnamurthy, "3D FE simulation of H_2 SAW gas sensor," *Sensors and Actuators B*, vol. 111, pp. 213–218, 2005.

[35] D. H. Wu and H. H. Chen, "Application of Taguchi robust design method to SAW mass sensing device," *IEEE Transactions on Ultrasonics, Ferroelectrics, and Frequency Control*, vol. 52, pp. 2403–2410, 2005.

[36] S. J. Ippolitto, K. Kalantar-Zadeh, D. A. Powell, and W. Wloderski, "A 3-dimensional finite element approach for simulating acoustic wave propagation in layered SAW devices," in *proceedings IEEE Ultrasonics Symposium*, 2003, pp. 303–306.

[37] X. Wang, and G. Xu, "Numerical study of the effects of film properties to the mass sensitivity of surface acoustic wave sensors," in *proceedings IEEE Ultrasonics Symposium*, 2005, pp. 442–448.

[38] G. Xu, "Direct finite-element analysis of the frequency response of a Y-Z lithium niobate SAW filter," *Smart Materials and Structures*, vol. 9, pp. 973–980, 2000.

[39] A. C. Tikka, S. F. Al-Sarawai, and D. Abbott, "Finite element modeling of SAW correlator," in *Proceedings of SPIE*, vol. 6799, 2007.

[40] H. Subramanian, V. K. Vardan, V. V. Vardan, and M. J. Vellekoop, "Design and fabrication of wireless remotely readable MEMS based microaccelerometers," *Smart Materials and Structures*, vol. 6, pp. 730–738, 1997.

[41] M. N. Hamidon, S. A. Mousavi, M. M. Isa, and M. A. Mahdi, "Finite element method on mass loading effect for gallium phosphate surface acoustic wave resonators," in *Proceedings of the World Congress Engineering*, vol. 1, 2009.

[42] A. W. Warner, M. Onoe, and G. A. Coquin, "Determination of elastic and piezoelectric constants for crystals in class (3M)," *The Journal of the Acoustical Society of America*, vol. 42, pp. 1223–1231, 1968.

[43] T. Kannan, "Finite element analysis of surface acoustic wave resonators," M.S. dissertation, Dept. Electrical Engineering, University of Saskatchewan, Saskatoon, Saskatchewan, 2006.

[44] N. Ramakrishnan, R. P. Palathinkal, and H. B. Nemade, "Mass loading effect of high aspect ratio structures grown over surface acoustic wave resonators," *Sensor Letters*, vol. 8, no. 2, pp. 1–5, 2010.

[45] D. M. Klymyshyn, T. Kannan, and A. Kachayev, "Finite element modeling of electrode mass loading effects in longitudinal leaky SAW resonators," *Microwave and optical technology letters*, vol. 51, no. 2, 2009.

[46] N. Ramakrishnan, H. B. Nemade, and R. P. Palathinkal "Finite element simulation of a surface acoustic wave hydrogen sensor with palladium nano-pillars as sensing medium," *Sensor Letters*, vol. 8, no. 6, pp. 824–828, 2010.

[47] Y. Kagawa and T. Yamabuchi, "Finite element simulation of a composite piezoelectric ultrasonic transducer," *IEEE Transactions on Sonics and Ultrasonics*, vol. SU-26, no. 2, pp. 81–88, 1979.

[48] J. Koskela, V. P. Plessky, and M. M. Salomaa, "SAW/LSAW COM parameter extraction from computer experiments with harmonic admittance of a periodic array of electrodes," *IEEE Transactions on Ultrasonics, Ferroelectrics, and Frequency Control*, vol. 46, no. 4, pp. 806–816, 1999.

[49] G. Zhang, "Nanostructure-enhanced surface acoustic waves biosensor and its computational modeling," *Journal of Sensors*, vol 2009, pp. 1–11, 2009.

[50] N. Ramakrishnan, A. K. Namdeo, H. B. Nemade, and R. P. Palathinkal, "Simplified model for FEM simulation of SAW delay line sensor," *Journal of Procedia Engineering*, vol. 41, pp. 1022–1027, 2012.

[51] V. Laude, A. Khelif, Th. Pastureaud, and S. Ballandras, "Generally polarized acoustic waves trapped by high aspect ratio electrode gratings at the surface of a piezoelectric material," *Journal of Applied Physics*, vol 90, 2492, pp. 2492–2497, 2001.

[52] P. Bauerschmidt, R. Lerch, J. Machui, W. Ruile, and G. Visintini, "Reflection and transmission coefficients of SAW in a periodic grating computed by finite element analysis," in *proceedings IEEE Ultrasonics Symposium*, 1990, pp. 421–423.

[53] G. F. Iriarte, F. Engelmark, I. V. Katardjiev, V. Plessky, and V. Yantchev, "SAW COM-parameter extraction in AIN/diamond Layered Structures," *IEEE Transactions on Ultrasonics, Ferroelectrics, and Frequency Control*, vol. 50, no. 11, pp. 1542–1547, 2003.

[54] M. B. Schulz and J. H. Matsinger, "Rayleigh-wave electromechanical coupling constants," *Applied Physics Letters*, vol. 20, no. 9, pp. 367–369, 1972.

[55] G. Visintini, C. C. W. Ruppel, and R. Greening, "Vistini Angular spectrum of waves analysis of SAW filters with dispersive transducers," in *proceedings IEEE Ultrasonics Symposium*, 1989, pp. 107–112.

[56] K. Bløtekjaer, K. A. Ingebrigtsen and H. Skeie, "Acoustic surface waves in piezoelectricmaterials with periodic metal strips on the surface," *IEEE Transactions on Electron Devices*, ED-20, pp. 1139–1146, 1973.

[57] K. Bløtekjaer, K. A. Ingebrigtsen and H. Skeie, "A method for analysing waves in structuresconsisting of metal strips on dispersive media," *IEEE Transactions on Electron Devices*, ED-20, pp. 1133–1138, 1973.

[58] R. F. Milsom, N. H. C. Reilly, and M. Redwood, "Analysis of generation and detection of surface and bulk acoustic waves by interdigital transducers, *IEEE Transactions on Sonics and Ultrasonics*, vol. SU-24, no. 3, pp. 147–164, 1977.

[59] K. Honkanen, J. Koskela, V. P. Plessky, and M. M. Salomaa, "Parasitic BAW excitation in LSAW transducers," in *proceedings IEEE Ultrasonics Symposium*, 1998, pp. 949–952.

[60] K. J. Gamble, and D. C. Malocha, "Bulk wave excitation from finite length SAW transducers including massloading," in *proceedings IEEE Ultrasonics Symposium*, 1999, pp. 77–81.

[61] M. Deng, "Simulation of generation of bulk acoustic waves by interdigital transducers," in *proceedings IEEE Ultrasonics Symposium*, 2001, pp. 855–858.

[62] K-Y Hashimoto, M. Yamaguchi, G. Kovacs, K. C. Wagner, W. Ruile, and R. Weigel, "Effects of the bulk wave radiation on IDT admittance on 42° YX-$LiTaO_3$, *IEEE Transactions on Ultrasonics, Ferroelectrics, and Frequency Control*, vol. 18, no. 5, pp. 1419–1425, 2001.

[63] N. H. C. Reilly, R. F, Milsom, and M. Redwood, "Generation of Rayleigh and bulk waves by interdigital transducers on Y-cut Z-propagating lithium niobate," *Electronics Letters*, vol. 9, no. 18, 1973.

[64] K. C. Wagner, and G. Visintini, "Simulation of bulk wave effects in SAW devices using Green's function and angular spectrum of waves," in *proceedings IEEE Ultrasonics Symposium*, 1989, pp. 103–106.

[65] B. A. Auld and G. S. Kino, "Normal mode theory for acoustic waves and its application to the interdigital transducer," *IEEE Transactions on Electron Devices*, ED-18, no. 10, pp. 898–908, 1971.

[66] G. S. Kino and T. M. Reeder, "A normal mode theory for the Rayleigh wave amplifier," *IEEE Transactions on Electron Devices*, ED-18, no. 10, pp. 909–920, 1971.

[67] J. J. Campbell and W. R. Jones, "A method for estimating optimal crystal cuts and propagation directions for excitation of piezoelectric surface waves," *IEEE Transactions on Sonics and Ultrasonics*, vol. SU-15, no. 4, pp. 209–217, 1968.

[68] A. Wixforth, J. Scriba, M. Wassermeier, J. P. Kotthaus, G. Weimann, and W. Schlapp, "Surface acoustic waves on GaAs/AlGaAs heterostructures, *Physical Review B,* vol. 40, pp. 7874–7887, 1989.

[69] M. Elkordy, "Study of voltage tunable SAW hybrid devices," in Proceedings 6th International SYmposium on Antennas, Propagation and EM Theory, 2003, pp. 750–753.

[70] D.-P. Chen and H. A. Haus, "Analysis of metal-strip SAW gratings and transducers," *IEEE Transactions on Sonics and Ultrasonics*, vol. SU-32, no. 3, pp. 395–408, 1985.

[71] H. Skeie, "Mechanical and electrical reflections in interdigital transducers," in *proceedings IEEE Ultrasonics Symposium*, 1972, pp. 408–412.

[72] Y.-G Zhao, M. Liu, D.-M. Li, J.-J. Li, J.-B. Niu, "FEM modeling of SAW organic vapor sensors," *Sensors and Actuators A: Physical*, vol. 154, pp. 30–34, 2009.

[73] S. J. Martin, G. C. Frye, and S. D. Senturia, "Dynamic and response of polymer-coated surface acoustic wave devices: effect of viscoelastic properties and film resonance," *Analytical Chemistry*, vol. 66, pp. 2201–2219, 1994

[74] M. Cole, G. Sehra, J. W. Gardner, and V. K. Varadan, "Development of smart tongue devices for measurement of liquid properties," *IEEE Sensor Journal*, vol. 4, no. 5, 2004.

[75] T. Nomura et al., "Measurement of acoustic properties of liquids using SH-type surface acoustic waves," in *proceedings IEEE Ultrasonics Symposium*, 1990, pp. 307–310.

[76] *Piezoelectric Materials and Devices*, Fomos-Materials co., Moscow, 2001–2014. [online]. Available: http://www.newpiezo.com/product.html

[77] P. Walker and W. H. Tarn, *CRC Handbook of Metal Etchants*. Florida: CRC Press, 1991, p. 28.

[78] Y. Murakawa et al., "Surface acoustic wave based sensors employing ionic liquid for hydrogen sulfide gas detection," *Microsystem Technologies*, vol. 19, pp. 1255–1259, 2013.

List of Publications

Journal Publications:

1. N. Ramakrishnan, Ashish Kumar Namdeo, Harshal B. Nemade, and Roy Paily Palathinkal, "Simplified model for FEM simulation of SAW delay line sensor," *Journal of Procedia Engineerin,* Elsevier, vol. 41, pp. 1022-1027, 2012.
2. Ashish Kumar Namdeo and Harshal B. Nemade, "Simulation on effects of electrical loading due to interdigital transducers in surface acoustic wave resonator," *Journal of Procedia Engineering*, Elsevier, vol. 63, pp. 322-330, 2013.
3. Ashish Kumar Namdeo and Harshal B. Nemade, "A finite element analysis of surface acoustic wave resonator with non-contact interdigital transducer," *IEEE Journal of Microelectromechanical Systems*. (Submitted)

Conference Publications:

1. Ashish Kumar Namdeo, N. Ramakrishnan, Harshal B. Nemade, and Roy Paily Palathinkal, "FEM study on contactless excitation of acoustic waves in SAW devices," *Excerpt from the Proceedings of the COMSOL Conference*, Bangalore, India, 2009.
2. Ashish Kumar Namdeo, Harshal B. Nemade, and N. Ramakrishnan, "FEM simulation of generation of bulk acoustic waves and their effects in SAW devices," *Excerpt from the Proceedings of the COMSOL Conference*, Bangalore, India, 2010.
3. Ashish Kumar Namdeo and Harshal B. Nemade, "FEM study on the effect of metallic interdigital transducers on surface acoustic wave (SAW) velocity in SAW devices," *Excerpt from the Proceedings of the COMSOL Conference*, Bangalore, India, 2011.
4. N. Ramakrishnan, Ashish Kumar Namdeo, Harshal B. Nemade, and Roy Paily Palathinkal, "A finite element method simulation of SAW delay line sensor using periodic boundary conditions," in *Proceedings International Conference on Advanced Nanomaterials and Nanotechnology*, Guwahati, India, 2011.
5. Ashish Kumar Namdeo and Harshal B. Nemade, "FEM study on short circuit of surface charges due to interdigital transducers in surface acoustic wave devices," *Excerpt from the Proceedings of the COMSOL Conference*, Bangalore, India, 2012.
6. Ashish Kumar Namdeo and Harshal B. Nemade, "Extraction of COM parameters and quality factor of one port SAW resonator using FEM based simulation," *Excerpt from the Proceedings of the COMSOL Conference*, Bangalore, India, 2014.

Patents filed:

1. Ashish Kumar Namdeo, Harshal B. Nemade, and N. Ramakrishnan, "Contactless interdigital transducer based on electrostatic principle for surface acoustic wave devices," Indian Patent application no. 591/KOL/2010, Jun. 1, 2010.
2. Ashish Kumar Namdeo and Harshal B. Nemade, "Electrostatically coupled surface acoustic wave devices with bond pads," Indian Patent application no. 1085/KOL/2011, Aug. 19, 2011.
3. Ashish Kumar Namdeo and Harshal B. Nemade, "On-board contactless interdigital transducer and planner antenna for wireless surface acoustic wave devices," Indian Patent application no. 833/KOL/2013, Jul. 12, 2013.
4. Ashish Kumar Namdeo and Harshal B. Nemade, "On-chip surface acoustic wave devices in silicon with contactless IDT," Indian Patent application no. 834/KOL/2013, Jul. 12, 2013.